ABSTRACT

Title of Dissertation: INTERFACE DESIGN FOR ALL-SOLID-STATE LITHIUM METAL BATTERIES

Xinzi He, Doctor of Philosophy, 2022

Dissertation directed by: Professor Chunsheng Wang
Department of Chemical and Biomolecular Engineering

Lithium-ion batteries (LIBs) have expanded their application from electronics to electric vehicles (EVs). To ease the safety concerns and the “range anxiety”, solid-state lithium batteries (SSLBs) become a more attractive choice. The replacement of flammable and toxic liquid electrolytes with solid-state electrolytes (SSEs) makes it a safer option. The utilization and compatibility of high specific capacity materials such as sulfur cathode and lithium-metal anode increase the cell energy density. However, SSLBs still face challenges towards practical application, which mainly from the solid-solid contact nature on the interfaces. On the anode side, lithium dendrite growth and high interface resistance both hindered the longevity of the cells. On the cathode side, low initial Coulombic efficiency (CE) and low capacity utilization of sulfur obstructed the realization of high loading cathodes.

In this dissertation, I addressed both challenges of dendrite and contact on the anode side by adding strontium into lithium anodes. Different from all previous metal/metal oxide coating on garnet or Li alloy anodes that form lithiophilic interlayer, a lithiophilic/lithiophobic bifunctional layer is formed to reduce the interfacial resistance and to suppress the growth of lithium dendrite, which is confirmed by comprehensive material characterizations, electrochemical evaluations, and simulations. The optimum Li-Sr | garnet | Li-Sr symmetric cells achieve a high critical current density (CCD) of 1.3 mA/cm^2 and can be cycled for 1,000 cycles under 0.5 mA/cm^2 at room temperature, providing a new strategy for high-performance garnet SSLB. Furthermore, I (1) verified the importance of lithiophobic on dendrite suppression by discovering and successfully constructing the highest interface energy (γ, against lithium) material ever reported among all lithium compounds that can be formed on the electrolyte | anode interface; (2) revealed the impact of anode properties on the interface by enhancing the Li self-diffusivity by a co-doping method, achieved an outperformed critical loading of 4.1 mAh/cm^2 at 1.0 mA·cm^{-2} at room temperature. On the cathode side, I tackled both low CE and low capacity utilization issues by promoting both Li$^+$ and e^- transportation across the cathode | SSE interface, resulting in high capacity utilization of 96.5% and high capacity retention of 88.8% after 145 cycles at a high loading of 4.0 mAh cm^{-2} under room temperature in Li_6PS_5Cl based SSLB.

INTERFACE DESIGN FOR ALL-SOLID-STATE LITHIUM METAL BATTERIES

by

Xinzi He

Dissertation submitted to the Faculty of the Graduate School of the
University of Maryland, College Park, in partial fulfillment
of the requirements for the degree of
Doctoral of Philosophy
2022

Advisory Committee:
Professor Chunsheng Wang, Chair
Professor Hosam Fathy
Professor Dongxia Liu
Professor Chen Zhang
Professor Paul Albertus

Dedicated to

Those who have been struggling and suffering but keep marching on with a brave heart

Acknowledgements

I would like to acknowledge the help from my advisor-Professor Chunsheng Wang, during my study and research in his group from 2017 to 2022. Prof. Wang not only taught and enlightened me as a wise and creative researcher, but also shows me the important characters of enthusiasm, diligence, and cooperation which is a gift that I could use for a lifetime. I would also like to thank my committee members: Prof. Hosam Fathy, Prof. Dongxia Liu, Prof. Chen Zhang and Prof. Paul Albertus for their attention, suggestion and encouragement.

I want to thank Prof. Xiao Ji, who acts as a teacher to me after I join Prof. Wang's group. I wish Prof. Ji to become a successful professor at Huazhong University of Science and Technology. I am also grateful to Dr. Hongli Wan, Prof. Long Chen, Dr. Tao Deng, and Dr. Singyuk Hou for their patient help and generous sharing whenever I encounter difficulties. I would also like to thank my collaborators, Zeyi Wang, Dr. Jijian Xu, Prof. Chao Luo, Bo Nan, Weiran Zhang, Dr. Panxing Bai, Dr. Sufu Liu, Dr. Yuxun Ren and Dr. Qin Li for the technical support and assistance. I would like to thank my lab mates, Dr. Ji Chen, Prof. Fudong Han, Dr. Jiale Xia, Dr. Nan Piao, Prof. Xiulin Fan, Prof. Tao Gao, Prof. Ma Lin, Prof. Chongyin Yang, Prof. Pengfei Wang, Dr. Aimin Li, Dr. Min Wu, Dr. Xiyue Zhang, Dr. Nico Eidson, Dr. Jiaxun Zhang, Prof. Xiayin Yao, Prof. Minglei Mao, Dr. Haiying Che, Dr. Chunyu Cui, An Phan, Nan Zhang, Prof. Ting Jin, Prof. Fei Wang, Dr. Yujia Liang, Boyu Wang, Tingting Qing, Dr. Jing Zheng and Dr. Jie Yue, who create a friendly and supportive environment in the lab. I would also like to thank my industrial and national lab mentors, Dr. Meng Wang, Ashwin Krishna Murali, Shubro Biswas, Dr. Jason Zhang, Dr. Xia Cao and Prof. Xiaochuan Lu for your support to help me see my research and contribution to the battery field from a more comprehensive perspective.

Finally, I want to thank University of Maryland for the perfect platform and the supporting from the Graduate School's Ann G. Wylie Dissertation Fellowship. I'd also like to send my special acknowledgement to my families, Weiqun Xin and Xiangming He for their selfless and unconditional love. I love you forever.

Table of Contents

List of Tables

List of Figures

Chapter 1 Introduction

1.1 Sustainable Energy and Energy Storage Devices

With the advent of electric vehicles and the extensive usage of various new mobile electronic devices, sustainable clean energy has become more and more important for the whole planet and future generation. Energy storage devices are the connections between clean energy sources (such as wind energy, solar energy, etc.) and people's practical daily life [1], which can gather the energy from the former sources and release it for the latter.

Energy storage technologies can be categorized into physical energy storage (such as pumped water storage, compressed air energy storage, flywheel energy storage, etc.), chemical energy storage (such as various energy storage batteries, flow batteries hydrogen fuel cells, and supercapacitors, etc.) and magnetic energy storage (such as superconducting magnetic energy storage technology, SMES) [2]. Among which, lithium-ion battery is the most successfully commercialized energy storage device.

1.2 Lithium-ion Batteries and Next Generation Batteries

Lithium-ion battery is a secondary battery in which lithium ions are intercalated and deintercalated back and forth between the positive (cathode) and negative (anode) electrodes, accompanied by redox reactions. The cathode is generally a lithiumcontaining transition metal oxide; there are many types of canoed material, and commercialized lithium-ion batteries mostly use graphite. The electrolyte is generally a lithium salt dissolved in an organic solvent. A porous polymer film is often used as a separator to separate the anode from the cathode to avoid short-circuits. **Figure 1-1** is a schematic diagram of the working principle of a lithium-ion battery. During discharge, the lithium-ion stored between the graphite layers migrates and intercalates into the cathode. And vice versa when charging.

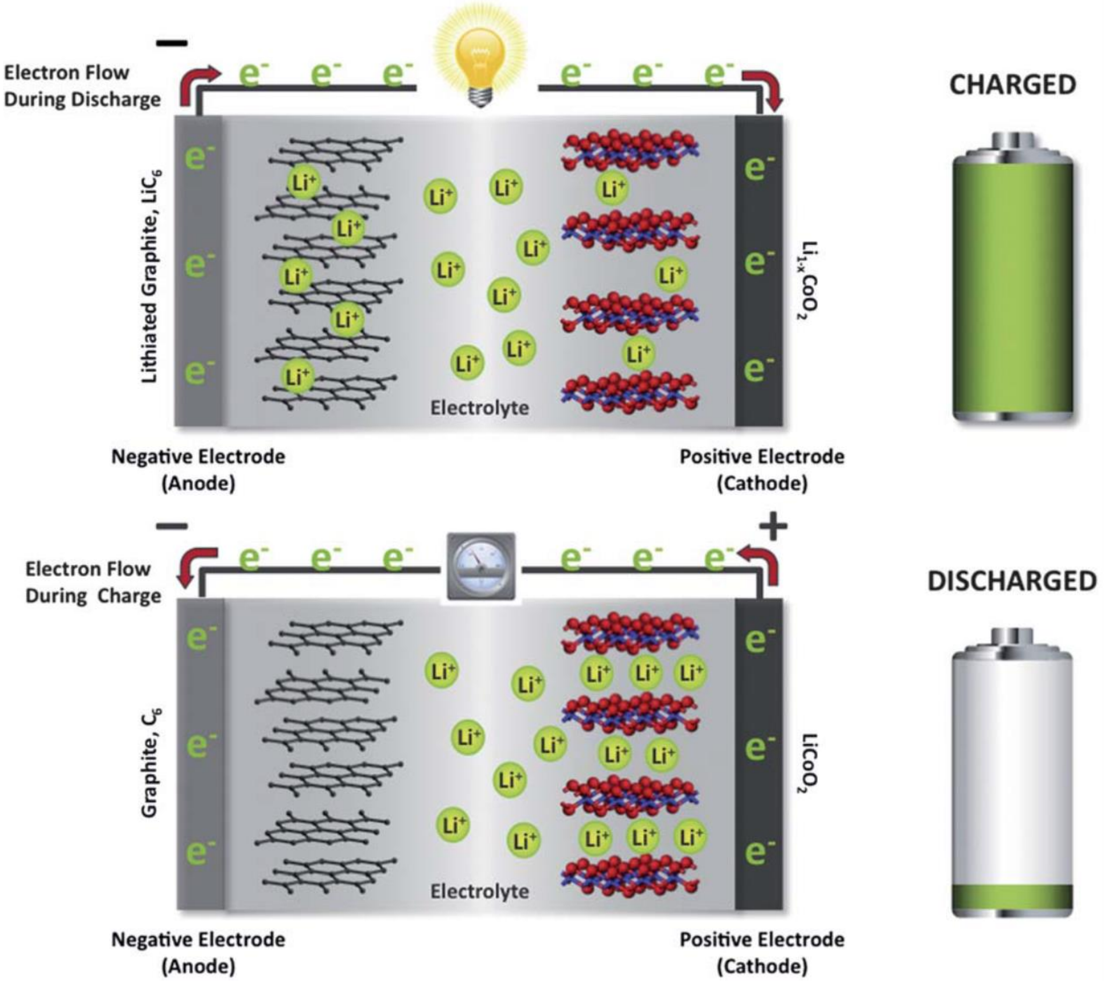

Figure 1-1 A schematic illustration of the working principles of a $Li_xC_6/Li_{1-x}CoO_2$ lithium-ion cell. During discharge, lithium ions diffuse from a lithiated graphite

(Li_xC_6) structure (the anode) into a delithiated $Li_{1-x}CoO_2$ structure (the cathode) with concomitant oxidation and reduction of the two electrodes, respectively. The reverse process occurs during charge. [3]

Lithium-ion battery was first mass-produced by Sony in Japan in the 1990s, utilizing $LiCoO_2$ as the positive electrode and graphite as negative electrode. With significant advantages such as small size, long cycle life, no memory effect, and high working voltage, lithium-ion batteries have a wide range of applications. In addition to portable electronic devices, people's pursuit of electric/hybrid vehicles and large-scale power grids in recent years has also brought lithium batteries into more exposure.

In the past two decades, lithium-ion batteries and their industries have continued to flourish. However, in recent years, the existing lithium-ion battery technology has gradually been unable to meet people's increasingly stringent requirements on batteries for mobile consumer electronic devices, electric vehicles, and large-scale energy storage system. Next generation battery technologies have gradually become a hotspot.

Although lithium-ion batteries are powering almost everything in our daily life from your cell phone, laptop to even electric vehicles, scientists are still pursuing next-generation batteries to make the electric vehicle range longer, the cell phone charge faster and the laptop battery lighter. And most importantly, making a high safety battery to protect people from any accident caused by the batteries thermal runaway.

The all-solid-state lithium metal battery is believed to be the ultimate answer, in which the substitution of flammable organic liquid electrolyte to solid state electrolyte (SSE) provides the safety while the substitution of graphite to lithium metal anode provides the high energy.

1.3 All-Solid-State Lithium Metal Batteries

The basic structure and working principle of all-solid-state lithium batteries are similar to those of traditional lithium-ion batteries. [4] As shown in **Figure 1-2**, the lithium-ion battery is composed of cathode, separator, electrolyte, anode and current collector. While the SSLB keeps the solid electrodes and replaces the separator and liquid electrolyte with a solid-state electrolyte (SSE).

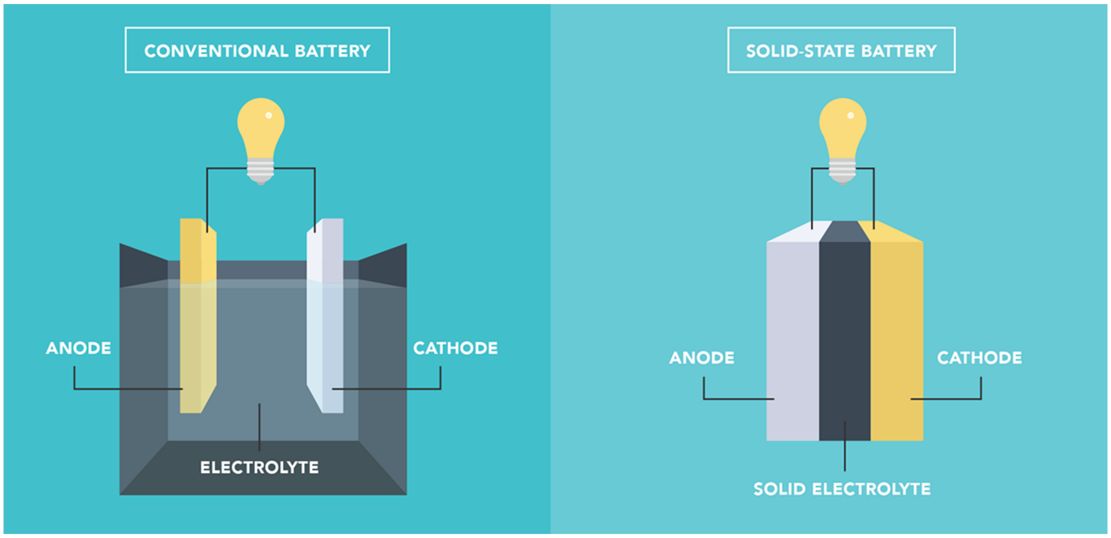

Figure 1-2 A schematic illustration of the structure of a solid-state batteries. [4]

Take $LiCoO_2$ – Graphite lithium-ion battery as an example:

Cathode: $$LiCoO_2 \leftrightarrow Li_{1-x}CoO_2 + xLi^+ + xe^-$$

Anode: $6C + xLi^{+} + xe^{-} \leftrightarrow Li_xC_6$

Overall reaction: $LiCoO_2 + 6C \leftrightarrow Li_{1-x}CoO_2 + Li_xC_6$

When the anode material is substituted to lithium metal, the cathode reaction keeps the same, while the anode an overall reaction become:

Anode: $xLi^{+} + xe^{-} \leftrightarrow xLi$

Overall reaction: $LiCoO_2 \leftrightarrow Li_{1-x}CoO_2 + xLi$

Given the fact that most of the current all-solid-state batteries use metallic lithium or lithium alloy as the anode and it is also the main subject this dissertation focuses on, this article collectively refers to such batteries as solid-state lithium metal batteries (SSLBs).

1.3.1 Advantages of Solid-State Batteries

Compared with traditional lithium-ion batteries, SSLBs have the following technical advantages:

1. High energy density. Thanks to the excellent stability and mechanical strength of the SSE, lithium metal is expected to be used in SSLB. Lithium metal is the lightest metal element in the periodical table. It has a very low reduction potential (−3.04 V vs. standard hydrogen electrode potential) and an ultrahigh theoretical specific capacity (3, 860 m Ah g^{-1}). In addition, when high-voltage positive electrodes are

used in conjunction with lithium metal, the energy density of the battery can be further improved.

2. The shape of the battery is highly expandable and has a wide range of applications. Thanks to the material diversity and good processability, SSLB can be produced in various forms, such as sputtering, pressing, casting, etc. which are applicable to a variety of occasions.

3. Higher safety. SSLB utilizes SSE instead of toxic, flammable organic electrolyte that consists of organic solvent and lithium salts. It can solve the leakage, corrosion and other issues in traditional lithium-ion battery. In addition, inorganic solid electrolytes have significantly improved heat dissipation compared with liquid electrolytes.

4. Simplified battery pack design. Single SSLB can be connected in series in order to reduce the waste of energy/volumetric density from the auxiliary materials (such as current collectors and packaging). Its excellent wide temperature work range greatly reduces the dependence on thermal management modules, which is further improving energy density on the pack level.

1.3.3 SSE and its Categories

There are many kinds of SSE with totally different characteristics. Generally, SSE can be divided into oxides, sulfides and polymers. Among them, the oxide solid electrolyte can also be subdivided into LISICON (Lithium superionic conductors) type, NASICON (Sodium superionic conductors) type, garnet type, etc. [5] Sulfides can also be divided into binary Li_2S-P_2S_5, LGPS series, lithium argyrodite Li_6PS_5X ($X = Cl$, Br, I), etc.[6] While polymer SSE can be divided into polyethylene oxide (PEO) base, polypropylene oxide (PPO) base, base, polymethyl methacrylate (PMMA) base, polyacrylonitrile (PAN) base, etc. In addition, LiPON-based thin-film solid electrolytes, hydride, nitride and halide SSE have also been developed rapidly in recent years. In view of the large number of types, the following highlights a few of the most commonly used types.

1.3.4 Garnet-type SSE

As demonstrated in **Figure 1-3,** Garnet SSE was first reported by Thangadurai in 2003.[7] Among which, garnet SSE with a nominal formula $Li_7La_3Zr_2O_{12}$ (LLZO) [8] demonstrates a high ionic conductivity (1 mS/cm for Ta-doped LLZO [9]) and wide electrochemical window [8,10]. In addition, the high mechanical properties are expected to block the lithium dendrite penetration.

In its crystal structure, Li^+ will first occupy and fill tetrahedrons and be fixed, thus contributing less to the overall conductivity. While the octahedrals are not filled, the accordingly generated vacancies will provide the main channel for Li^+ conduction. Since lithium ions need such directional diffusion to adjacent vacancies to generate ionic conduction and there is no Li^+ vacancies in the tetragonal phase. Thus, the tetragonal LLZO (t-LLZO) is thermodynamically more stable than the cubic LLZO (c-LLZO), but the ionic conductivity is orders of magnitude lower.

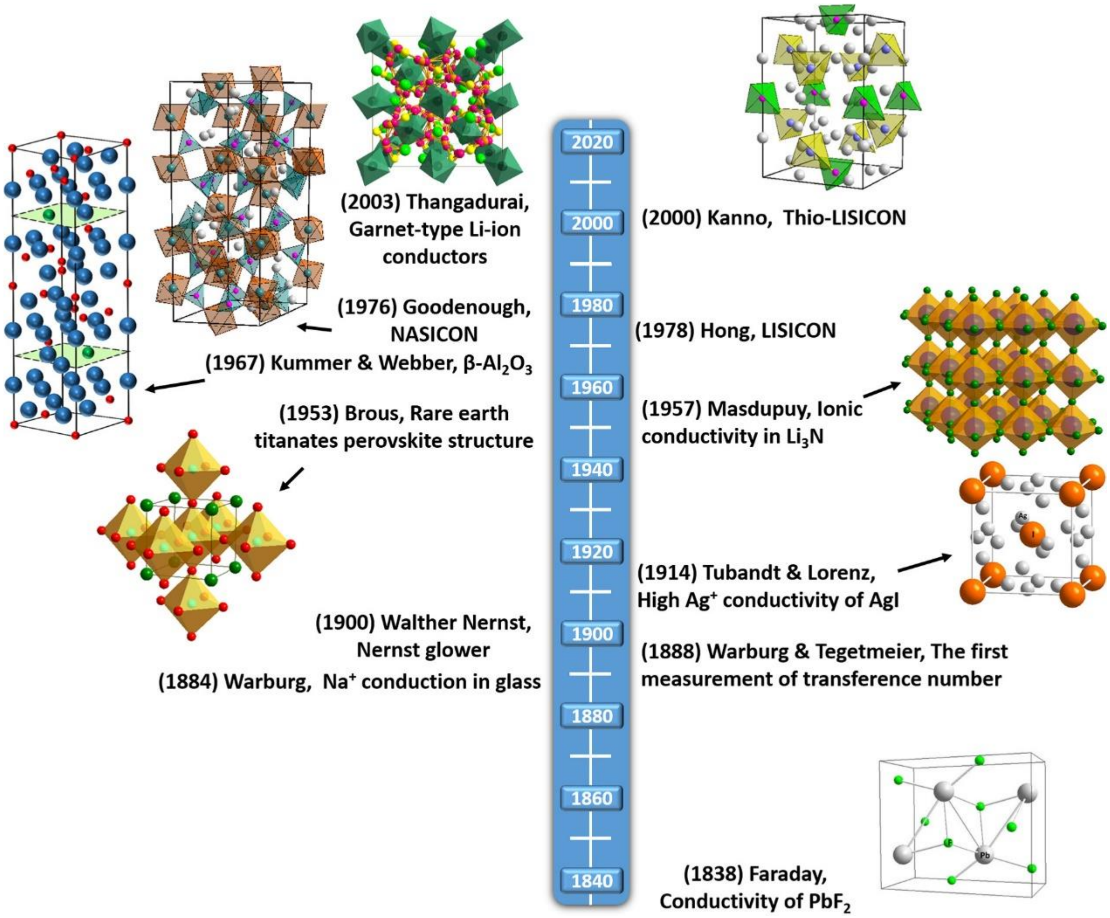

Figure 1-3 Historical development of solid electrolytes and schematic of their structures.[5]

Massive efforts had been made on how to increase lithium vacancies to obtain cubic LLZO. Major methods includes: substitution of Li+ site with high-valence cations ion Al^{3+}, Ga^{3+}; replacement of Zr^{4+} sites with Sb^{5+}, Nb^{5+}, Ta^{5+}, Te^{5+}, W^{5+}; substituting La^{3+} site with Rb^{3+} etc.[11] Among witch, ionic conductivity as high as 1.62×10^{-3} S cm^{-1} at room temperature through Ga^{5+}, Rb^+ co-doping can be achieved.[12,13]

Although garnet-type SSE have good performance, its hard and brittle characteristics also lead to poor interface contact with the electrode and thus obstacles in the processing towards practical application. [12] The Ta-doped LLZTO (Li6.5La3Zr1.5Ta0.5O12) is selected as one of the model SSE in this dissertation for its high ionic conductivity and stability against the lithium anode, and detail of the synthesis process will be elaborate in Chapter 2.1.1.

1.3.3 Argyrodite-type SSE

Argyrodite Li_6PS_5X (X=Cl, Br, I) has a parent phase of Li_7PS_6, and a cubic phase (originally an orthorhombic phase at low temperatures) can be obtained by substituting part of S to X, resulting in 10^{-3} S cm^{-1} level of Li^+ conductivity.[14] **Figure 1-4** shows the structure and the lithium-ion transportation modes of the Li_6PS_5X.

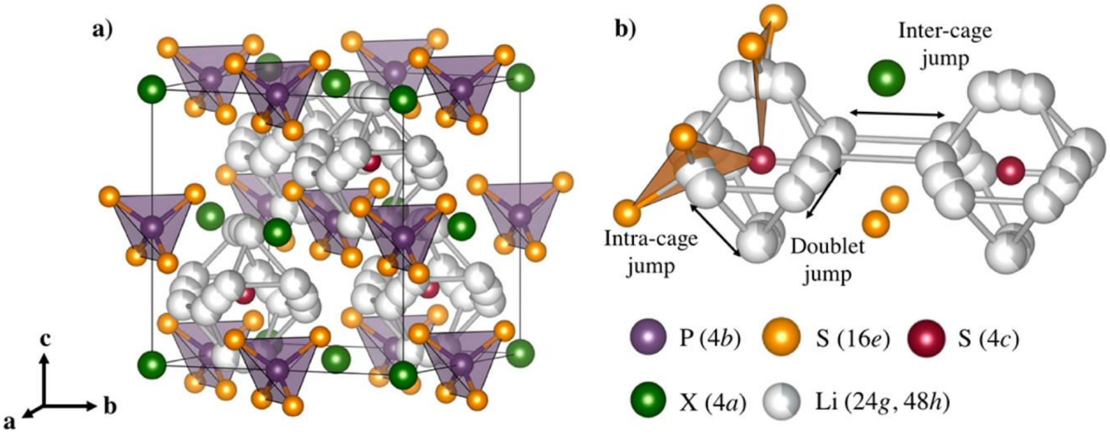

Figure 1-4 Crystal structures of Li_6PS_5X with X = Cl, Br, I. (b) Doublet jump, intra-cage jumps and inter-cage jump of Li in the Li_6PS_5X.

There are two major preparation methods for argyrodite Li_6PS_5X, liquid phase method and solid phase synthesis method. The liquid phase method is a good way to synthesize particles with controllable particle size and morphology, which makes it possible to tune the relevant properties of the SSE. In 2015, Yubuchi et al.[15] first reported the synthesis of Li_6PS_5Cl by dissolution-reprecipitation method with ethanol as the solvent. However, the ionic conductivity at room temperature of $1.4\times l0^{-5}$ S cm^{-1} is not very ideal. Afterwards, Yubuchi et al.[16] utilized tetrahydrofuran (THF) and absolute ethanol (EtOH) as dual solvents, resulting in 10^{-3} S cm^{-1} level of Li^+ conductivity. However, significantly more impurities are always found in argyrodite Li_6PS_5X made by liquid phase method, mainly due to the inevitable reactions between the P_4S_3 unit and the solvent.[17]

In the solid phase method, precursors Li_2S, P_2S_5 and LiX are annealed under protected inert atmosphere after mechanical milling. Rao et al. reported the synthesis of Li_6PS_5Cl using this solid route for the first time and got an ionic conductivity of 1.1×10^{-3} S cm^{-1} at room temperature.[18] The Li_6PS_5Cl using solid route is selected as one of the model SSE in this dissertation for its high ionic conductivity, feasibility and repeatability of synthesis, and detail of the synthesis process will be elaborate in Chapter 2.1.3.

1.4 The Challenges of All-Solid-State Lithium Metal Batteries and Progress

1.4.1 Lithium Metal Anode and its Interface with SSE

As discussed in Chapter 1.3, lithium metal is considered to be the ideal anode material for next-generation batteries for its high theoretical specific capacity. However, the interfacial contact of the inorganic solid electrolyte/metal lithium anode interface is poor and the dendrite penetration has become the biggest obstacles to the application of metal lithium anode.

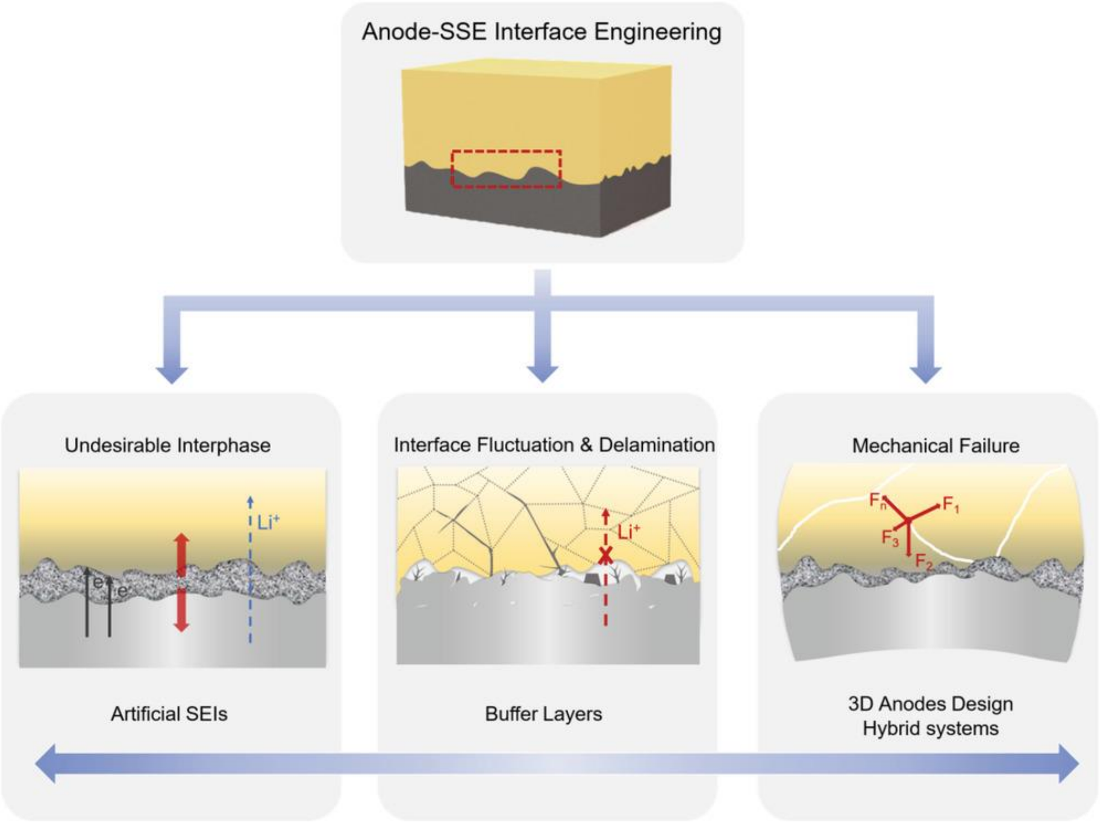

Figure 1-5 The overview of main existing problems and strategies for the anode–SSE interface.[19]

On the one hand, the poor wettability between inorganic SSE and lithium metal results in a large interfacial resistance. On the other hand, the interfacial reaction at the electrolyte/lithium metal interface leads to the formation of an interfacial layer, which may hinders the migration of Li^+ and leads to performance degrades. Most importantly, lithium dendrites form in solid-state batteries and penetrate the solid electrolyte, causing internal short-circuit, leading to serious safety hazards. Therefore, exploring the interface design of inorganic solid electrolyte/lithium metal towards 1) good contact, 2) high stability, 3) dendrite-free, become the most critical challenges.

1.4.2 Sulfur-Based Cathode and its Interfaces in Solid-State Batteries

The energy density of the current state-of-art lithium-ion/metal batteries are restricted by the traditional metal oxide cathodes (such as $LiCoO_2$, $LiFePO_4$ and $LiMnO_4$, etc.) which usually have a theoretical specific capacity of around 100-200 mAh g^{-1}. Due to the high theoretical specific capacity of sulfur element (1675 mAh g^{-1}), lithium-sulfur batteries are considered to be the best choice for next-generation high-energy-density energy storage systems.

During the conversion between S_8 and Li_2S, polysulfide would form as intermediate product. These polysulfides can dissolve in common liquid Li-S electrolytes, which will migrate from the cathode to the anode under the concentration gradient, and further being reduced by lithium metal, forming the “shuttle effect”[20], leasing to the loss of active material and efficiency.

Fortunately, replacing organic liquid electrolyte to SSE can prevent the formation of polysulfide and eliminate the polysulfide “shuttle effect”. However, there are also other problems, such as the insulating properties of S and Li_2S and the volume change between the S and Li_2S. The former will lead to poor electrochemical reaction kinetics, resulting in the low utilization rate of active materials, causing the increase of the polarization inside the battery and reduction of the energy density. The latter with a volume expansion of about 80% after lithiation[21] will cause the cathode material to pulverize and permanent loss of capacity. Both these two problems will be much tougher challenges in a solid-state battery originating from the poor solid-solid contact of the three main component inside a cathode for solid-state battery: the active material, the electronic conductor and the SSE. Therefore, the interface design of the electronic additive/SSE/sulfur triple-phase boundaries become the most critical challenge.

Improving the Li^+ transfer through coating SSE on sulfur, or enhancing the e-conduction using electronic conductive carbon as sulfur host can enhance S/Li_2S redox reaction due to the improved triple-phase contacts in these modified sulfur composite cathode. However, the preparation procedures for these modified sulfur cathodes are time-consuming. Besides, the low active sulfur content in the S@C composite will decrease the cell-level energy density because the large amount of electronic conductive carbon host cannot provide capacity to the battery. Therefore, sulfur host that can provide extra capacity was introduced into the sulfur Among these active sulfur hosts, FeS_2 with high electronic/ionic conductivity has been demonstrated to mediate the sulfur redox reaction in SSLB.[22,23] Besides, the pyrite cathode has a high-cost advantage. FeS_2 could reduce cathode material costs by 90%, from $35 per kWh to $3 per kWh. Therefore, FeS_2 will be used as the model sulfur host for this dissertation to studies the interface design of cathode-electrolyte, which will be elaborate in Chapter 6.

1.5 Motivation, Objectives and Dissertation Layout

1.5.1 Motivation and Objectives

In order to achieve the goal of high energy density and high safety next-generation SSLB battery, both deeper fundamental understanding and practical advance of the electrode-electrolyte interface design are urgently needed.

On the anode side, I choose garnet SSE as the model electrolyte for its stability against lithium, which provides a low-noise background as by-product free as possible. In this way, the interface components will be simplified, and related interface properties can be clearer. And I will focus on the interface design toward both better solid-solid contact and dendrite suppression.

On the cathode side, the establishment of garnet cathode requires a co-sintering of the cathode materials and the ceramic electrolytes, which can be time consuming for each iteration. In consideration of the efficiency and reproducibility, I choose sulfide as the model electrolyte for the cathode study.

1.5.2 Dissertation Layout

Chapter 2: Common experimental methods used in following chapters, such as the synthesis of the SSE will be summaries in here to avoid repetition.

Chapter 3: On the anode side interface, I will address both the challenges of Li dendrite and high interface resistance by doping strontium(Sr) into lithium anodes, thus form a lithiophilic/lithiophobic bifunctional layer. The interlayer reduces the interfacial resistance and also suppresses lithium dendrite. This work is published in ACS Energy Letter. (**He, X**.; Ji, X.; Zhang, B.; Rodrigo, N. D.; Hou, S.; Gaskell, K.; Deng, T.; Wan, H.; Liu, S.; Xu, J.; Nan, B.; Lucht, B. L.; Wang, C. Tuning Interface Lithiophobicity for Lithium Metal Solid-State Batteries. *ACS Energy Letter* **2021**. https://doi.org/10.1021/acsenergylett.1c02122.)

Chapter 4: In this Chapter, I screened the Gibbs energy for the reaction between Li and the metal oxides ($nLi + MO_m \leftrightarrow M + nLiO_{m/n}$) and identified the $LiYO_2$ as a highly thermodynamical stable candidate for the interface between the electrolyte and lithium. In addition, $LiYO_2$ has a record high interface energy against lithium of 81.65 meV/Å, which would provide high dynamic stability against dendrite penetration. This work is ready to submit. (**He, X**.; Ji, X.; Wang, Z.; Wan, H.; Wang, C. High Interface Energy Enabled Highly Stable Garnet-based Lithium Metal Solid-State Batteries)

Chapter 5: I will discuss my attempt to understand the void formation on the SSLB anode interface. The product of the lithium full stripping capacity and the applied current, which will be defined as the void suppression capability (VSC). The relationship between the CCD/interface-stability and VSC will be discussed. Enhancement of the VSC will be demonstrated by refining the grain using a Mg-1wt%La inoculant. This work is under review with Nature Material. (Ji, X.†; **He, X.†**; Chen, C.†; Hou, S.; Xu, J.; Zhang, B.; Ruan, Y.; Zhang, J.; Deng, T.; Chen, J.; Wang, C. Void Suppressive Lithium Anodes for All-Solid-State Batteries. (Co-First Author))

Chapter 6: On the cathode side, I will elaborate on the idea to construct a FeS_2@S@CuI composite to form a decent Li^+/e^- pass way across the cathode | Li_6PS_5Cl SSE interface upon first several cycle. The S/Li_2S redox kinetics will be enhanced for better capacity utilization at high cathode loading (4.0 mAh cm^{-2} under room temperature). This work is ready to submit. (Wan, H. †; He, X.†; Ren, Y.; Wang, C. Highly reversible sulfur cathode for all-solid-state lithium-sulfur battery (Co-First Author))

Chapter 2 Material Synthesis, Battery Fabrication and Characterization Methods

2.1 Material Synthesis Methods

2.1.1 Synthesis of the LLZTO Solid Electrolyte

The LLZTO garnet electrolyte was synthesized via a conventional solid-state reaction technique. $LiOH·H_2O$ (99.995%, Sigma-Aldrich, 10 wt.% excess to compensate for the loss of Li during high-temperature sintering), La_2O_3 (99.99%, Sigma-Aldrich, pre-heated at 900°C for 12 h to remove the water), ZrO_2 (99.5%, Alfa Aesar), and Ta_2O_5 (99.99%, Sigma-Aldrich) with stoichiometry ratio were used as precursors. The mixture was mechanical ball-milled (PM 100, Retsch) at 400 rpm for 24 h within a zirconia ceramic vial together with anhydrous 2-propanol. ZrO_2 balls with a diameter of 5 mm were used as the grinding medium. After ball-milling, the slurry was dried and calcined at 900 °C for 10 h in the Al_2O_3 crucible. After the first calcining, the powder was ball-milled again with the same parameters as above. This step is done to decrease the particle size further and increase the reactivity of the powder. Then, the obtained powder was sieved through 100 grits after drying. The obtained powder was pressed into Φ13 mm pellets, followed by isotactic pressing under 0.2 metric tons. The pellets were then sintered in air at 1150°C for 5 hours in MgO crucible covered with the same powder. The area of the obtained LLZTO pellet is around 0.75 cm^2 and the thickness is around 1 mm.

2.1.2 Assembly of the LLZTO Cells

For Li-Au | LLZTO | Li-Au symmetric cells, the gold was sputtered on the LLZTO pellets under 15 mA for 600 seconds (Cressington sputter coater 108). The residual Au on the side surfaces is polished off with sandpaper. Lithium foil was brushed to expose a fresh shining surface and punched into a round shape with a diameter of 3/8 inch. The Au sputtered LLZTO pellets were sandwiched by lithium foils followed by heat-treatment at 175°C for 12 hours to ensure the alloy reaction between Au and Li. Then, the as-prepared Li-Au | LLZTO | Li-Au symmetric cell was cooled down to room temperature for testing.

The symmetric cells were assembled in 2032-coin cells by sandwiching the spring, stainless steel (SS) disc, and the anode-attached pellet. The thickness was controlled around 100-200 μm for any Li or Li alloy anode attached to SSE.

In the "Proof of Concept" full-cells, the commercially available NMC811 cathode was provided by SAFT. The NMC811 with the loading of ~0.8 or 1.6 mAh/cm^2 was selected as the cathode for the SSLBS. The $LiFePO_4$ cathode was prepared by mixing $LiFePO_4$, conductive carbon and PVDF with a weight ratio of 80:10:10. A small amount of liquid electrolyte (10 μL) was used to wet the cathode | LLZTO interface.

2.1.3 Synthesis of the Li_6PS_5Cl Solid Electrolyte

As shown in **Figure 2-1**, Li_6PS_5Cl solid electrolyte was synthesized using high-energy mechanical milling. Li_2S (Sigma-Aldrich, 99.98%), P_2S_5 (Sigma-Aldrich, 99%) and LiCl (Sigma-Aldrich, 99%) were used as starting materials. These materials were weighed in the molar ratio of Li2S/P2S5/LiCl = 5/1/2 in an argon-filled glovebox, milled, and sintered at 550 °C for 5 hours under Ar.

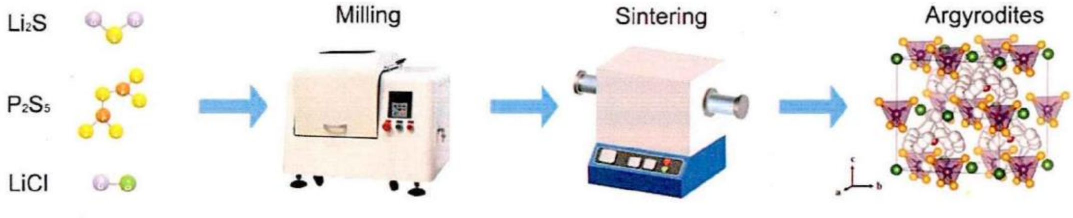

Figure 2-1 Schematic diagram of the synthesis process of Li argyrodite electrolytes in this work.[23]

2.2 Electrochemical Characterization Methods

The Li^+ ionic conductivity measurements of the electrolytes were carried out on an electrochemical station (Gamery G1000) with sputtered Au as the electrode. The measurements were performed over the frequency range from 1Hz to 1 MHz with an AC voltage amplitude of 10 mV.

2.3 Material Characterization Methods

SEM was taken at the University of Maryland using Hitachi SU-70 analytical GEG SEM (Japan) equipped with an EDS detector. The electron accelerating voltage is 200 KeV.

X-ray powder diffraction (XRD) was performed on D8 Advance with LynxEye and SolX (Bruker, USA) using Cu Kα radiation.

2.4 Density Functional Theory (DFT) Calculation

The DFT calculations[24,25] are performed by using Vienna Ab-initio Simulation Package (VASP)[26] with Projector Augmented Wave (PAW) method.[27] And the exchange-correlation energy is described by the functional of Perderw, Burke, and Ernzerhof (PBE) form[28,29] including van der Waals corrections (DFT-D3 method).[30] The kinetic energy cutoff of electron wave functions is 520 eV. The Brillouin zone is sampled by using the Monkhorst−Pack scheme.[31] The interface energy was evaluated using the same method in previous work.[32] Visualization of the atomic structures is made by using VESTA.[33]

Chapter 3 Tuning Interface Lithiophobicity for Lithium Metal Solid-State Batteries

3.1 Introduction

Lithium-ion batteries (LIBs) have expanded their application from electronics to electric vehicles (EVs).[34] To ease the safety concerns [35] and the "range anxiety", the solid-state lithium battery (SSLB) becomes a more attractive choice. The replacement of flammable and toxic liquid electrolyte [36] with solid-state electrolyte (SSE) makes it a safer option. Moreover, the wide electrochemical window of SSE enables the utilization of high-voltage cathodes and Li-metal anodes, which leads to a higher output voltage and thus a higher energy density.

Among all the inorganic SSE, garnet SSE with a nominal formula $Li_7La_3Zr_2O_{12}$ (LLZO) [8] demonstrates a high ionic conductivity (1 mS/cm for Ta-doped LLZO [9]) and wide electrochemical window [8,10]. In addition, the high mechanical properties are expected to block the lithium dendrite penetration. Unfortunately, short-circuiting is still observed even at a low current density and a low capacity. Meanwhile, solid-solid contact at Li | LLZO also induces a high interface resistance, which accelerates the reduction of the SSE and the dendrite growth. Thus, interfacial engineering that is aiming to minimize interfacial impedances is critical for SSLB. Introducing a lithiophilic interlayer to wet Li metal is proved as an effective strategy to reduce the interface resistance. Various materials such as Au [37], Mg [38,39], Ag [40], Ge [41], Al [42], Si [43], Al_2O_3 [44], and ZnO [45], have been utilized to form alloys or prelithated layers. In addition, various surface coating technologies, such as sputtering [18], vapor deposition [42], metal salt aqueous solution [46], and atomic layer deposition [47], are applied to form an interlayer between Li and garnet. Interfacial engineering has successfully reduced interfacial resistance from thousands to single-digit Ω cm^2. [44] This extremely small interfacial resistance at Li | SSE already rivals the ones in conventional LIBs employing liquid electrolytes. [48] However, these interlayers are electronic conductive, which promotes the reduction of solid-state electrolytes and Li dendrite growth. The interfacial engineering seems to be stuck in a new bottleneck since no breakthrough was obtained using new interfacial materials or coating methods. A strategy forming a stable interlayer that keeps an ionic-conducting nature and separates the lithium plating position away from the SSE is needed.

For Li anode, one significant interface resistance comes from the void formation during Li stripping at a high current and capacity due to low Li^0 diffusivity and large volume shrink. Since the voids cannot be completely healed in the following Li plating process, the void will accumulate into a large hole, increasing the interface resistance [49,50] . If pressure is applied, the plastic deformation capability of the anode also plays an essential role in void evolution. [51] The Li^0 self-diffusivity can be accelerated by the high lithiophilicity at the Li/SSE interface. [39] However, the wisdom of Li dendrite suppression in liquid electrolytes suggests that a lithiophobic SEI is needed to achieve a high critical current density, which in turn will increase the interface resistance. To simultaneously reduce the interface resistance and also suppress lithium dendrite, a bifunctional surface layer that forms lithiophilic innerface bonding to Li and lithiophobic out-layer bonding to SSE is desired. To maintain a low interface resistance during long-term lithium plating/stripping cycles, the lithiophilic/lithiophobic bifunctional layer should be stable at SSE | anode interface without diffusion into or reaction with neither Li nor SSE, and should not reduce the diffusivity of Li^0 and/or Li^+. Although the alloy interface can provide an initial good wettability, the electron-conducting nature of the alloy interfacial layer will facilitate the charge transfer reaction to take place right between the interlayer and the SSE. [52] The deposition of lithium will push the alloy layer away instead of remaining located at the SSE | anode interface [5,38,53,54] , which may not be able to keep benefit for the long-term operation condition.

The ideal bifunctional interlayer for lithium anode should (1) be stably enriched at Li | SSE interface where lithiophilic part toward to the inside Li and lithiophobic part toward to SSE; (2) not reduce the anode Li^0 diffusivity on lithiophilic side and do not reduce the SSE on lithiophobic side; (3) have a plastic deformation capability to accommodate Li volume change. However, such a Li bifunctional layer has not been explored yet.

Li_2O has a high interfacial energy γ and high Li dendrite suppression ability γE, [32] which can function as a lithiophobic interlayer to suppress the lithium dendrite growth and lithiophobicity should reflect each other from energy and macroscopic angles, respectively. [55] However, the low ionic conductivity and high interface resistance at Li | Li_2O also introduced considerable resistance [56]. In this work, we demonstrated that 1% of strontium and *in situ* formed SrO could serve as a bifunctional interlayer where SrO doped Li_2O keeps the high lithiophobic nature of the Li_2O but reduces resistance due to the formation of lithiophilic Li-Sr alloy. The unique bifunctional property of Sr-in-Li anodes can reduce the interface resistance and also suppress the Li dendrite, which is distinct from other alloy electron-conductor layers. SrO also shows a robust garnet-philic property as evidenced by the high ionic conductivity of Sr-doped garnet [57,58], and the high wetting capability of Sr-in-Li on garnet. Using Ta-doped LLZTO ($Li_{6.5}La_3Zr_{1.5}Ta_{0.5}O_{12}$) as a model solid-state electrolyte [9] , the interface resistance, critical current density (CCD) and cycle stability of LLZTO were systematically investigated using bifunctional Sr-in-Li anodes. The mechanism of bifunctional Sr-Li at Li | LLZTO was revealed using comprehensive characterization, electrochemical performance evaluation, and simulation.

3.2 Experimental

3.1.1 Synthesis of the Li-Sr Alloy and the Assembly of the Anode

The anode was prepared by a molten lithium method in a glove-box. Initially, 1%, 5%, 10%, and 20% of mole ratio Sr metal flask was added into molten lithium metal at 300℃ in a stainless-steel crucible. The crucible was kept at 300℃ in an oven for 30 minutes, followed by stirring to ensure a homogeneous reaction. The as-synthesized alloy was melted in a shallow stainless-steel crucible at 300℃ with a hot plate inside the glove-box. The as-synthesized LLZTO electrolyte pellet was cleaned by mechanical dry-polishing using 400 grit sandpaper and then polishing with 1500 grit sandpaper in an Ar-filled glove-box. The cleaned pellet was directly immersed in the shallow crucible with the molten alloy in and the anode will be attached within around 2 minutes. After cooling down to room temperature, the residual metal on the side surface will be polished off with sandpaper. For Li | LLZTO | Li symmetric cells, lithium foil was brushed to expose a fresh shining surface and punched into a round shape with a diameter of 3/8 inch. After being immersed in the molten lithium for 2 minutes, the LLZTO pellets were cooled down to room temperature and sandwiched with two fresh lithium foils. The sandwiched cells were put under 175℃ for 12 hours then cool down to room temperature for testing. The thickness was controlled around 100-200μm for any lithium or Li-Sr alloy attached to SSE.

3.1.2 Material Characterization

XPS data were collected using the K-Alpha X-ray Photoelectron Spectrometer System (Thermo Scientific™, Al Kα radiation, hν = 1486.68 eV) at the University of Rhode Island. The sample preparation is the same as the Tof-SIMS test. The sample was directly moved from Ar atmosphere to the XPS chamber with a vacuum transfer container to avoid exposure to the air. The instrument was working under ultra-high vacuum ($<1\times10^{-12}$ atm). The spot size, as well as the analysis area, was 400 μm by 400 μm. The depth profiling was conducted using an Ar^+ ion gun with an ion energy of 200 eV. The angle between the ion gun beam and the surface normal was 0°. A 2 mm ion beam spot was quickly rastered over the targeted area. The etching procedure was carried out in a cycle of an accumulated 0, 300, 900, 3000 and 7200 seconds. Spectra were recorded of the sample surface before sputtering and between sputtering cycles. All data was calibrated based on the C1*s* peak to 284.8 eV for binding energy values. Peak fitting and relative atomic percentage estimation were done using CasaXPS software (version 2.3.24), after removal of a Shirley background and accounting for the relative sensitivity factors (R.S.F) of Thermo K-Alpha.

ToF-SIMS were analyzed on Ga^+ focused ion beam (FIB)/scanning electron microscope (Tescan GAIA3) equipped with ToF-SIMS at the NanoCenter of the University of Maryland. The accelerated voltage for FIB/SEM was 20 kV. To prepare the sample, the garnet pellet with anode reattached was cleaned with a scraper for removing the anode as much as possible in the Ar-filled glove-box before characterizations. The Sr (88), Zr (90), La (139), Li (7) were tested simultaneously in the negative mode. The O (16) was tested in the positive mode. The results from negative mode and positive mode were plotted together according to the depth of the craters measured in the SEM results. The frames were conversed to depth according to the depth of the craters measured in the SEM results. The surface of the sample (anode side) is defined as the 0 depth.

3.3 Li-Sr | LLZTO Interface and the Li-Sr Anode

Li-Sr alloys with 1%, 5%, 10%, and 20% of mole ratio Sr were synthesized by melting Li and Sr at 300°C. The corresponding Li-Sr alloys were noted as Li-Sr-1%, Li-Sr-5%, Li-Sr-10%, and Li-Sr-20%, respectively. As shown in **Figure 3-1** a, when the polished LLZTO pellet was immersed into the molten Li-Sr alloy, liquid Li-Sr alloy quickly spread onto the LLZTO surface, indicating a high wettability of Li-Sr alloy with LLZTO.

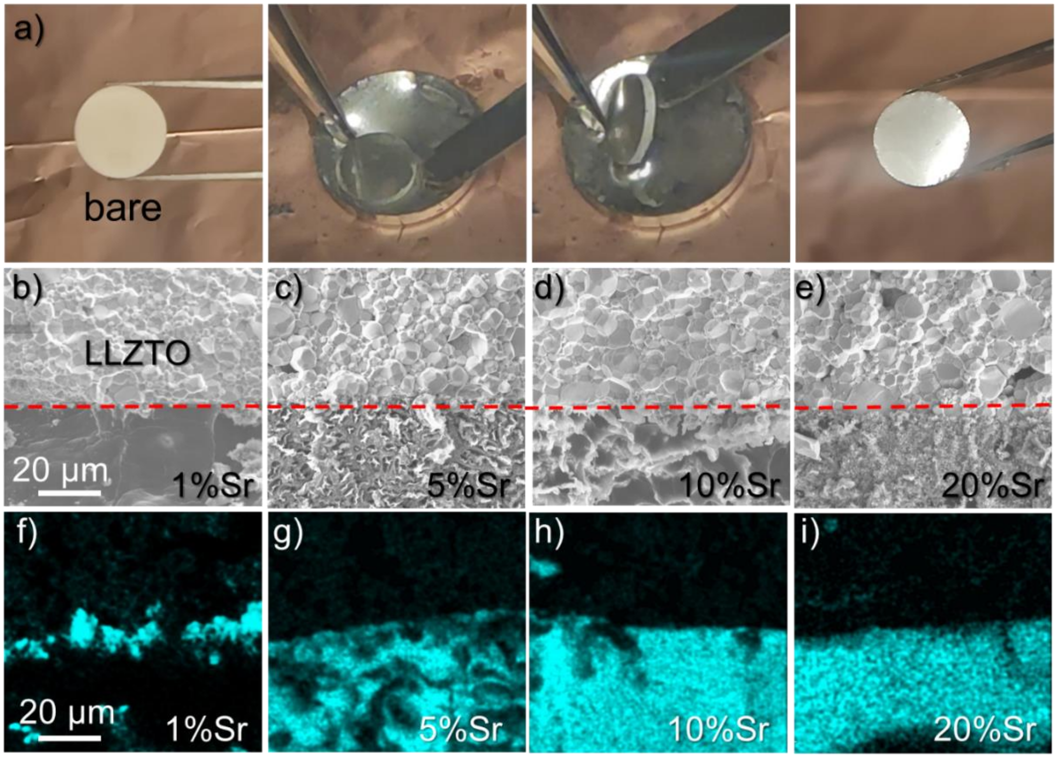

Figure 3-1 Assembling and characterization of Li-Sr | LLZTO interface. (a) Digital photographs showing the process of attaching the Li-Sr onto garnet LLZTO pellet. Cross-section morphology (b-e) and Sr elemental mapping (f-i) of the Li-Sr-1%, Li-Sr-5% Li-Sr-10% and Li-Sr-20% electrode interface with the LLZTO pellet. The red dash lines mark the interfaces.

The morphology and element distribution of the cross-section of Li-Sr | LLZTO interfaces were characterized by scanning electron microscopy (SEM). As shown in **Figure 3-1** b-i, all the Li-Sr | LLZTO interfaces, regardless of the anode composition, demonstrated seamless contact, confirming the high wettability of Li-Sr alloy against LLZTO. However, the microstructure of the Li-Sr anodes varies for different ratios Li-Sr. The Li-Sr-1% anode showed a monolith metal-like smooth surface while inhomogeneous blocks and granules were found for Li-Sr-5%, Li-Sr-10% and Li-Sr-20% anodes. The morphological variation should be attributed to the different phase-composition of Li-Sr alloy. According to the energy-dispersive X-ray spectroscopy (EDS) mapping, for the low Sr contained alloy (1%), Sr mainly segregates at the interface between LLZTO and the Li anode. The segregation of Sr at the interface is attributed to the high wettability of the Li-Sr alloy to LLZTO due to the strong interaction of Sr with O-atom at the interface. [59,60] As the Sr ratio in the Li-Sr alloy (**Figure 3-1** f-h) increases, more Sr-atoms can be found inside the bulk Li anode rather than segregating at the interface. Apparently, the higher ratio of Sr (>5% of Sr) will simultaneously affect the interface contact and the bulk Li anode.

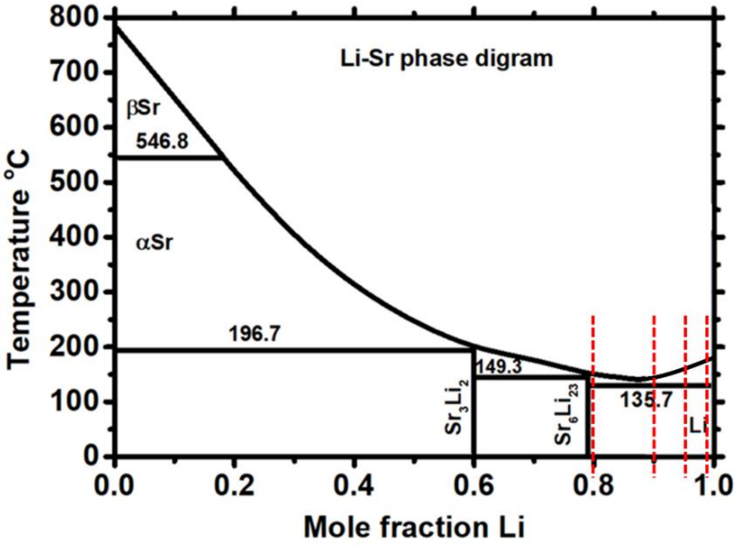

Figure 3-2 Phase Diagram of the Li-Sr system. The red dash lines mark the Li-Sr-1%, Li-Sr-5%, Li-Sr-10% and Li-Sr-10% composition from right to left.

According to the phase diagram in **Figure 3-2**, the equilibrium Li-Sr-1% alloy consists of Li metal and a small amount of $Li_{23}Sr_6$ intermetallic compound. $Li_{23}Sr_6$ can react with trace oxygen in the glove-box forming a lithiophobic Li-Sr-O layer on the Li surface and anchoring to the LLZTO (Figure 1f). With increasing of Sr, the content of Li_6Sr_{23} phase quickly increases and Li_6Sr_{23} will distribute into bulk Li, forming an inhomogeneous composite microstructure (**Figure 3-1** g-i). For Li-Sr-20% anode, the main component is $Li_{23}Sr_6$ phase (**Figure 3-2**), which has quite different physical and chemical properties compared with Li metal. The morphological and composition variation of the alloys affected the electrochemical performances when serving as anode for SSLBs.

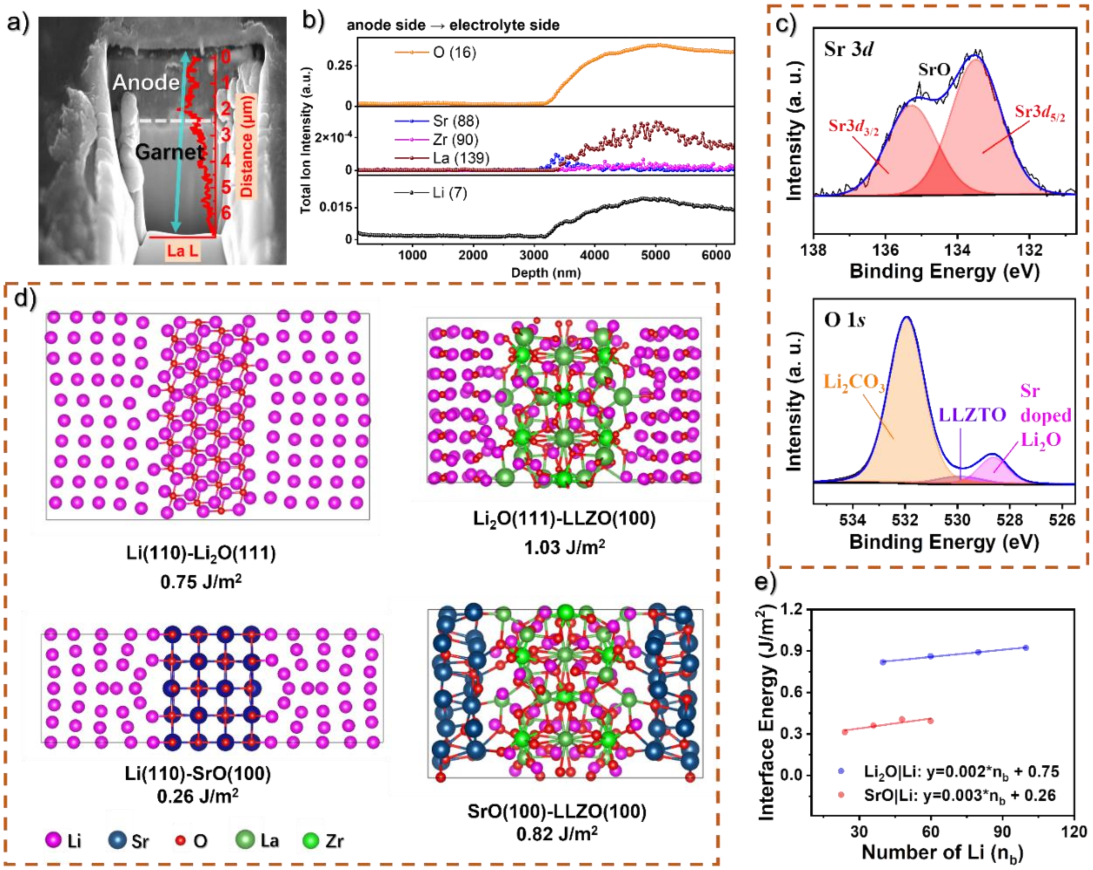

Figure 3-3 Characterization and calculation of the Li | Garnet interface. (a) The SEM image of a crater sputtered by the Ga^+ ion beam on the Li-Sr-1% | LLZTO interface showing the cross-sectional surface with an EDS elemental line scanning of the La L along scanning blue line. (b) ToF-SIMS analysis of the Li-Sr-1% | LLZTO interface. (c) The XPS spectra of the Sr 3*d* and O 1*s* on the Li-Sr-1% | LLZTO interface with 3,000 seconds of Ar^+ ion gun etching to remove the residual anode metal. The Li_2CO_3 signals are mainly from the environment. (d) The atomic structures of the Li (110)-Li_2O (111) interface, the Li_2O (111)- Garnet (100) interface, the Li (110) | SrO (100) interface and the SrO (100) | Garnet (100) interface, with the corresponding calculated interface energy γ by DFT. (e) Schematic diagram of the bifunctional lithiophilic/lithiophobic interlayer.

The Sr element segregation at Li | LLZTO interface for Li-Sr-1% anode was further characterized using depth-profiling time-of-flight secondary-ion mass spectroscopy (ToF-SIMS). As shown in **Figure 3-3** a, after removing Li-Sr-1% anode from LLZTO with a scraper, the LLZTO surface was sputtered using Ga^+ ion beam. The Li

| LLZTO interface can be clearly noticed on the SEM of the crater (marked with a white dash line), which ensures the sputtering depth was deep enough to reach the interface as well as the SSE. The EDS elemental line scanning was conducted on the line marked in blue (**Figure 3-3** a) and the distribution of the La element (red line in **Figure 3-3** a) agrees well with the SEM result. Accordingly, the ToF-SIMS analysis in **Figure 3-3** b shows a clear rise in the distribution of Zr (90), La (139), Li (7) and O (16) ions that are indicating the ion beam sputtering had reached the LLZTO solid electrolyte. Notably, the Sr (88) ion shows a peak right before the LLZTO phase, which validated the segregation of Sr element on the Li | LLZTO interface. The Sr ion enriched layer is around 250 nm thick, according to the ToF-SIMS analysis.

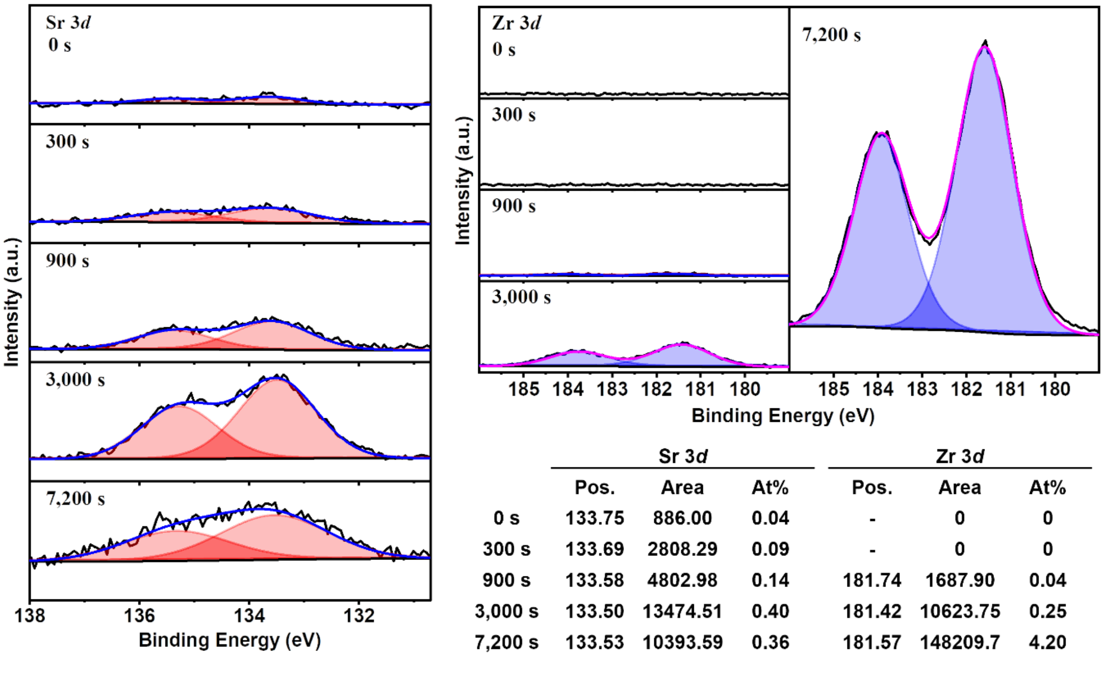

	Sr 3*d*			Zr 3*d*		
	Pos.	Area	At%	Pos.	Area	At%
0 s	133.75	886.00	0.04	-	0	0
300 s	133.69	2808.29	0.09	-	0	0
900 s	133.58	4802.98	0.14	181.74	1687.90	0.04
3,000 s	133.50	13474.51	0.40	181.42	10623.75	0.25
7,200 s	133.53	10393.59	0.36	181.57	148209.7	4.20

Figure 3-4 The XPS spectra and the quantification of the Sr 3*d* and Zr 3*d* on the Li-Sr-1% | LLZTO interface with Ar^+ ion gun etching at 0, 300, 900, 3000 and 7200 seconds. The atom percentage was calculated based on Li 1*s*, C 1*s*, O 1*s*, La 3*d*, Ta 4*f*, Sr 3*d* and Zr 3*d* in the survey from 0 to 1200 eV. The y-axis is the relative

emission intensity (a.u.) that is kept in the same proportion for all Sr 3*d* spectra and all Zr 3*d* spectra respectively.

X-ray photoelectron spectroscopy (XPS) was also conducted with Ar^+ ion gun etching to identify the valence of the Sr element in this layer. As shown in **Figure 3-4** and **Figure 3-5**, Sr 3*d* enriched at the 3,000 seconds' cycle, while after that, a more than 16 times Zr 3*d* amount and a reduced Sr 3*d* amount indicated the etching already reached the LLZTO layer. Therefore, the Li | LLZTO interface is at the 3,000 seconds' cycle, Sr 3*d* and Zr 3*d* here were analyzed in detail. From the Sr 3*d* spectra (**Figure 3-3** c), the peaks for $3d_{5/2}$ *and* $3d_{3/2}$ of SrO [61] located at 135.3 eV and 133.5 eV, respectively. The O 1*s* demonstrated that SrO doped Li_2O exists on the Li | LLZTO interface (**Figure 3-3** c). In addition to SrO, $LiCO_3$ also exists, which may come from atmospheric contamination.

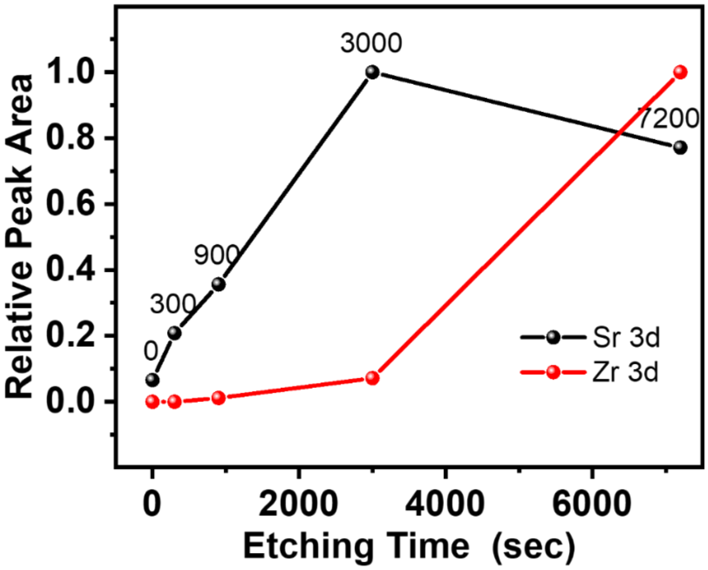

Figure 3-5 The relative peak area of Sr 3*d* and Zr 3*d* at 0, 300, 900, 3000 and 7200 seconds in the XPS. The Sr 3*d* (interface) and Zr 3*d*(SSE) are set as 1 respectively.

The quantification analysis (**Figure 3-6**) shows that Li_2O : SrO composition is roughly 9:1. Li_2O is lithiophobic with high interfacial energy of 0.75 J/m^2 and a high Li dendrite suppression ability. [32] However, the low Li-ion conductivity of Li_2O also induces a large overpotential.[56] Metal oxide doping to Li_2O cab be an effective method to reduce the resistance. SrO is one of the very few metal oxides that is relatively stable against Li with an equilibrium potential of 5.0 mV vs. Li [62] , similar to LLZO [10] .

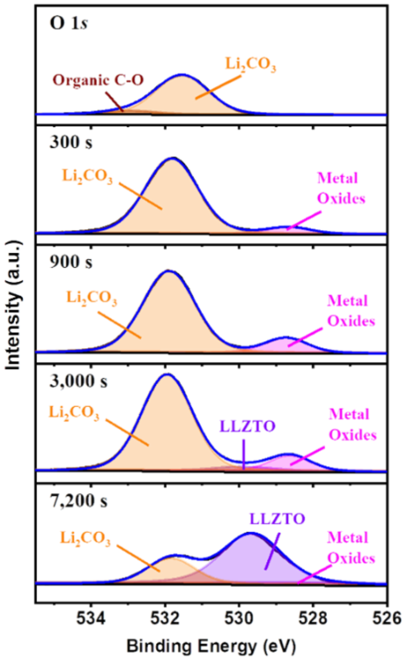

	Organic C-O			Metal Carbonates		
	Pos.	Area	At%	Pos.	Area	At%
0 s	532.68	31616	5.43	531.51	207745.17	35.68
300 s	-	-	-	531.82	421832.63	40.84
900 s	-	-	-	531.89	455482.38	34.27
3,000 s	-	-	-	531.94	520000.61	30.62
7,200 s	-	-	-	531.82	122662.56	6.60

	LLZTO			Metal Oxides		
	Pos.	Area	At%	Pos.	Area	At%
0 s	-	-	-	-	-	-
300 s	-	-	-	528.66	33908.53	3.28
900 s	-	-	-	528.73	74052.09	5.57
3,000 s	530	29386	1.73	528.61	72747.84	4.28
7,200 s	530	339915	18.29	528.66	18442.04	0.99

Figure 3-6 The XPS spectra and the quantification of the O 1*s* on the Li-Sr-1% | LLZTO interface with Ar$^+$ ion gun etching at 0, 300, 900, 3000 and 7200 seconds. The atom percentage was calculated based on Li 1*s*, C 1*s*, O 1*s*, La 3*d*, Ta 4*f*, Sr 3*d* and Zr 3*d* in the survey from 0 to 1200 eV. The y-axis is the relative emission intensity (a.u.) that is kept in the same proportion for all spectra.

In addition, the thermodynamic calculations were done using HSC-software [63] (**Table 3-1**) and the positive Gibbs energy for the reaction between Li and SrO also verify the relative stability of SrO against Li. Therefore, SrO doped Li_2O is stable with Li. In addition, SrO doped Li_2O also enhances the wettability with significantly reduced interface resistance (discussed in the following section) by reducing the interface energy between Li_2O and LLZTO, as demonstrated by the density functional theory (DFT) calculation. **Figure 3-3** d demonstrated that Li_2O is garnet-phobic due to the high interfacial energy of 1.03 J/m^2 with garnet. Since the Li_2O layer on the molten Li surface is unavoidable even in the glove-box, the molten Li with Li_2O surface cannot wet the LLZTO. Since SrO has low interface energy with garnet (0.82 J/m^2) and low interfacial energy against Li (0.26 J/m^2), SrO doped Li_2O *functions* as an anchor to bond both the Li anode and the LLZTO, which significantly reduce the interface resistance. In addition, the lithiophobic SrO doped Li_2O with low electronic conductivity can also suppress the reduction of LLZTO and Li dendrite growth (**Figure 3-3** e).

Table 3-1 The theoretical equilibrium potential and the Gibbs energy for the reaction between binary metal oxides and lithium metal. (*The Gibbs energy for the reaction between Li and the metal oxides ($nLi + MO_m \leftrightarrow M + nLiO_{m/n}$) are calculated using HSC-software[63] .)

MO_m	Theoretical equilibrium potential (mV)	$nLi + MO_m \leftrightarrow M + nLiO_{m/n}$ Gibbs energy* at 25 ℃ (kcal)
Al_2O_3	180	-24.179
ZnO	1252	-57.546
SiO_2	694	-63.540
SrO	**5**	**0.106**

3.4 Electrochemical Behavior of Li-Sr | LLZTO | Li-Sr Symmetric Cells

The Li plating/stripping behavior of the Li-Sr alloy anodes with different Li-Sr ratios was evaluated at room temperature using symmetric cells. The interfacial resistance before cycling was firstly measured using electrochemical impedance spectra (EIS). EIS plots (**Figure 3-7** a) of Li-Sr | LLZTO | Li-Sr cells demonstrated that Li-Sr-1% anode has the lowest impedance, and the total impedance of symmetric cells increase with Sr content in Li. The first semicircle (~1 kHz) of EIS plots is attributed to the total resistance of the LLZTO pellets (bulk and grain boundary), which is about 130-135 Ω cm^2 due to the difference of LLZTO pellets, which is consistent with conductivity measurement of LLZTO (**Figure 3-8**) and reported results [64]. The interfacial resistances (1kHz to 0.1Hz) increase with Sr content but they are still much smaller than that of Li | LLZTO | Li cells (**Figure 3-9**). The resistance from 1kHz to 0.01 Hz vastly increases with the increase of Sr content in the anode as 14, 40, 45, and 57 Ω cm^2 for Li-Sr-1%, Li-Sr-5%, Li-Sr-10%, and Li-Sr-20% anodes, respectively (**Figure 3-7** d), indicating that excess $Li_{23}Sr_6$ in bulk Li can reduce the Li atom diffusion.

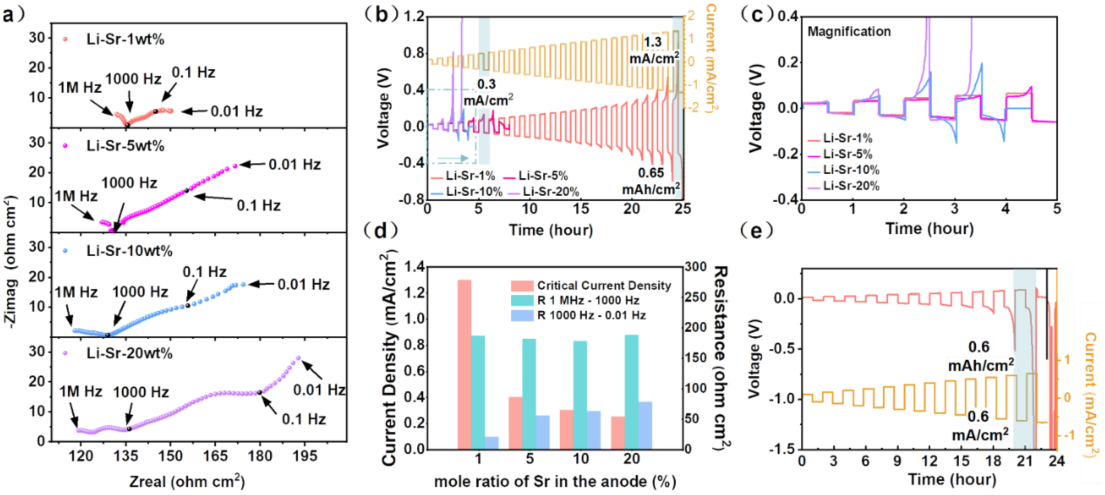

Figure 3-7 Electrochemical performance Li-Sr | LLZTO | Li-Sr symmetric cells. (a) Impedance spectra of the symmetric cells tested at room temperature from 1 MHz to 0.01 Hz. (From top panel to bottom panel are: Li-Sr-1%, Li-Sr-5%, Li-Sr-10% and Li-Sr-20%.) (b) The Li plating/stripping behavior for these cells at a step-increase current for 0.5 h, with (c) a magnified figure for the first 5 cycles. (d) The critical current densities and resistances verse the Sr mole ratio in the anode. (e) The Li plating/stripping behavior for the cell at a step-increase current for 1.0 h.

The CCD was evaluated using Li-Sr | LLZTO | Li-Sr cells by a step-increase current for a fixed 0.5 h of Li plating and 0.5 h of Li stripping. As shown in **Figure 3-7** b, the CCD for Li-Sr-1% cell is 1.3 mA/cm^2 at 0.65 mAh cm^{-2}, which is an order of magnitude higher than the CCD for Li | LLZTO|Li (**Figure 3-9**) and is highest among all reported alloy-based anode | LLZTO. [52] Therefore, SrO doped Li_2O bifunctional layer has a high Li dendrite suppression capability. Nevertheless, the CCD for the cells with Li-Sr-5%, Li-Sr-10%, and Li-Sr-20% anodes are only 0.40, 0.30 and 0.25 mA/cm^2, which are in line with resistance increase with Sr content in the EIS measurement (**Figure 3-7** d).

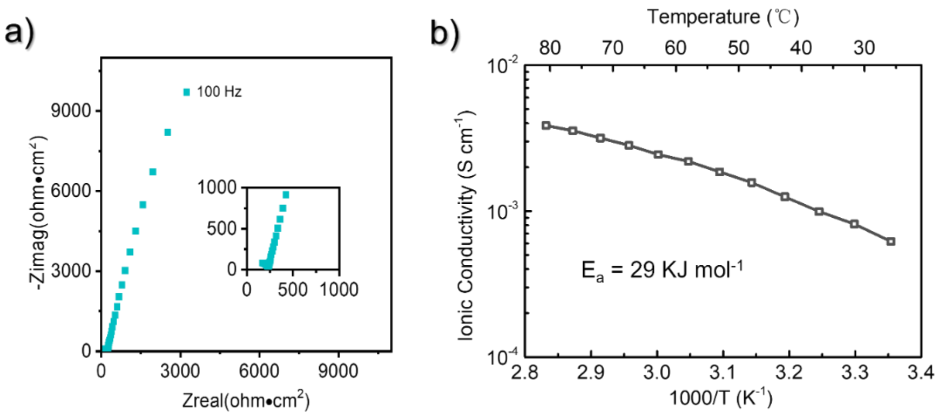

Figure 3-8 a) The EIS result of the Au | LLZTO | Au cell at 25℃. b) The Arrhenius plot for the Au | LLZTO | Au *cell* at temperatures from 25℃ to 80℃. The data points are the average of the test result of elevated temperature and decreasing temperature.

Detail analysis of Li plating/stripping curves of all Li-Sr anodes shows that a rapid increase in the slope of the voltage profiles at the latest stripping state right before the short circuit. The rapid increase of voltage can be induced by void formation. The void formation reduced the contact area at Li | LLZTO, which increases the local current density, thus reducing the CCD. For example, for Li-Sr-1% anode, the transformation from the flat voltage plateau to drastic polarization did not happen until a current density of ~1 mA/cm^2, while for the other three conditions the apparent potential boost occurred at a much lower current of 0.1 mA/cm^2 since Li$_{23}$Sr$_6$ in bulk Li may reduce the Li atom diffusion (**Figure 3-7** c). When the Li plating/stripping time was extended from 1.0 h to 2.0 h, CCD of Li-Sr | LLZTO | Li-Sr cell was decreased from 1.3 mA cm^{-2} (**Figure 3-7** b) to 0.6 mA/cm^2 **Figure 3-7** e), while the capacity at 1.0 h of plating and stripping time before short-circuit is similar to the capacity of 0.65 mAh/cm^2 measured at a short time of 0.5h (**Figure 3-7** b), indicating that the amount of the transported Li species controlled the void formation and also Li dendrite growth for the Li-Sr-1% anode.

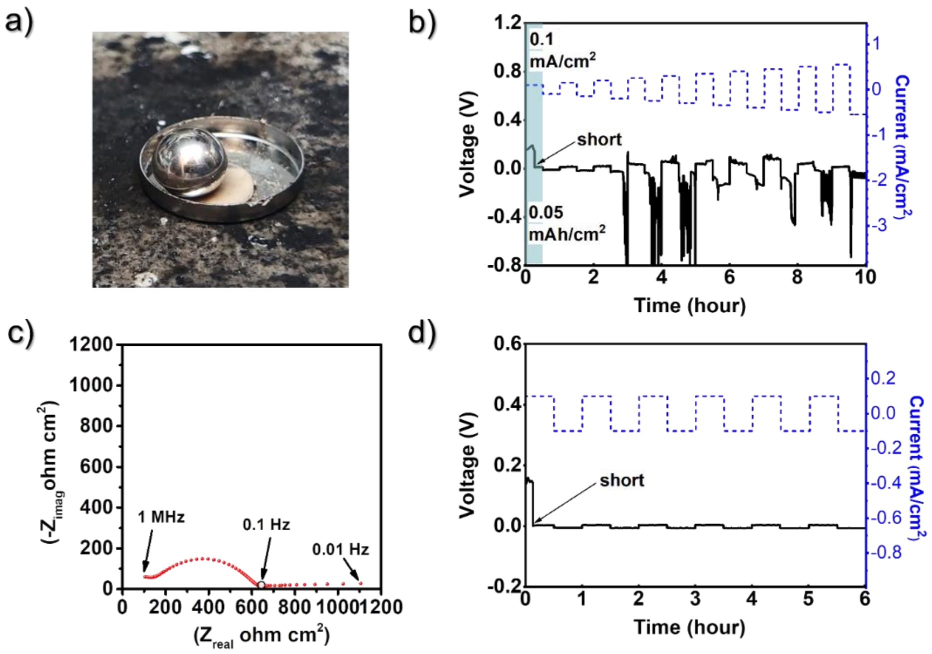

Figure 3-9 (a) Digital photographs showing attaching the Li onto garnet LLZTO pellet. (b) The Li plating/stripping behavior of the Li | LLZTO | Li symmetric cell at a step-increase current for 0.5 h each half-cycle at room temperature. (c) Impedance spectra of the Li | LLZTO | Li symmetric cell tested at room temperature from 1 MHz to 0.01 Hz. (d) Cycling performance of Li | LLZTO | Li symmetric cell at 0.1 mA/cm^2.

The cycling stability of Li-Sr | LLZTO | Li-Sr symmetric cells under a constant current of 0.2 mA/cm^2 and capacity of 0.1 mAh/cm^2 were also investigated. As exhibited in **Figure 3-10** a, the Li-Sr-1% | LLZTO | Li-Sr-1% symmetric cell demonstrated an excellent stability for 1,000 cycles with a neat and flat potential profile. In contrast, an intense polarization occurs in the Li-Sr-5% and Li-Sr-10% cells and follows with a short-circuit within the first five cycles. Even when current density increases to 0.5 mA/cm^2, the Li-Sr-1% | LLZTO | Li-Sr-1% symmetric cell still shows super cycling stability without any intense polarization for 1,000 cycles (**Figure 3-10** c), which is one of the best among reported planar garnet type solid-state electrolytes work at room temperature (**Table 3-2**).

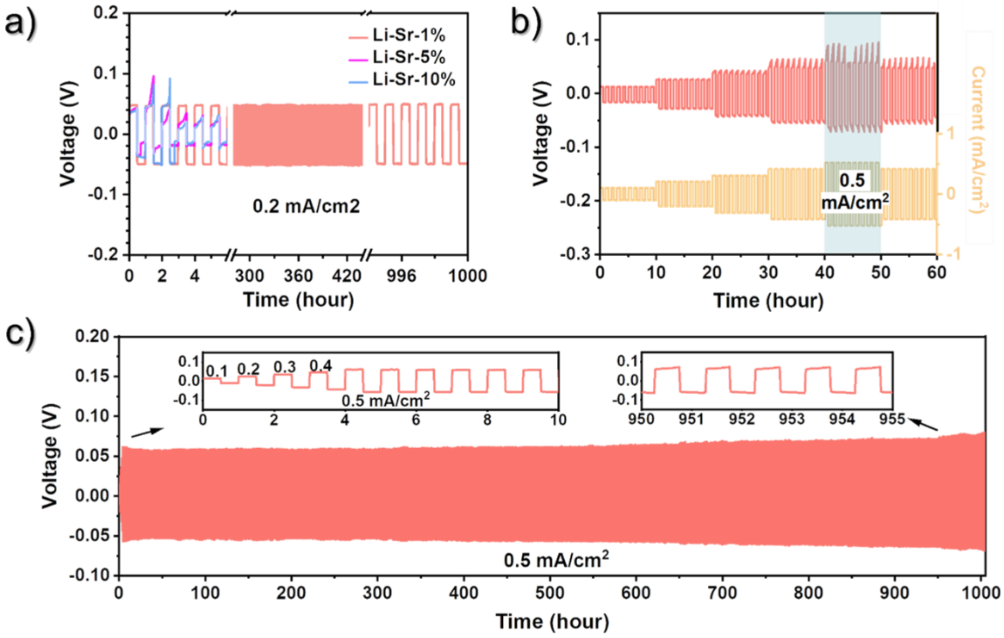

Figure 3-10 Cycling stability of Li-Sr | LLZTO | Li-Sr symmetric cells. (a) Long-term cycling performance at 0.2 mA/cm^2 with different Li-Sr anode. (b) Rate performance of Li-Sr-1% | LLZTO | Li-Sr-1% symmetric cell from 0.1 mA/cm^2 to 0.5 mA/cm^2. (c) long-term cycling performance of Li-Sr-1% | LLZTO | Li-Sr-1% symmetric cell at 0.5 mA/cm^2. Inset is the magnification of the voltage profiles of 1-10 cycles and 950-1000 cycles.

Table 3-2 Reported (2018-2021) cycling current, capacity and time for planar garnet type solid-state electrolytes at room temperature/25℃/30℃. (Ranking in descending order of cycling capacity)

Composition	**Methods**	**Cycling Current ($mA\cdot cm^2$)**	**Cycling Capacity ($mAh\cdot cm^2$)**	**Cycling Time (hour)**	**Ref.**
$Li_{6.5}La_3Zr_{1.5}Ta_{0.5}O_{12}$	Sr bifunctional layer	0.5	0.25	1,000	This work
$Li_{6.5}La_3Zr_{1.45}Ta_{0.55}O_{12}$	ultrafast sintering w/ Li_3N Filler	0.5	0.25	160	Acs Energy Lett. 6, 3753–3760 (2021).
$Li_{6.28}Al_{0.24}La_3Zr_2O_{12}$	Li–Zn alloy anode	0.35	0.175	2,200	Acs Appl Energy Mater. 3, 9010–9017 (2020).
$Li_{5.9}Al_{0.2}La_3Zr_{1.75}W_{0.25}O_{12}$	Graphite interface	0.3	0.15	1,000	Acs Energy Lett. 3, 1212–1218 (2018).
$Li_{6.5}La_3Zr_{1.5}Ta_{0.5}O_{12}$	Li-C composite	0.3	0.15	250	Advanced Materials. 31, 1807243 (2019).
$Li_{6\cdot4}La_3Zr_{1\cdot4}Ta_{0\cdot6}O_{12}$	SnO_2 coating	0.2	0.1	650	J. of Power Sources. 420, 15-21 (2019).
$Li_{6.28}La_3Zr_2Al_{0.24}O_{12}$	PVDF-PEO	0.1	0.1	600	J Mater Chem A. 9, 4018–4025 (2021).
$Li_{6.6}La_3Zr_{1.6}Ta_{0.4}O_{12}$	Acid Etching	0.2	0.1	200	ACS Appl. Energy Mater. 2, 6720–6731(2019).
$Li_{6.5}La_3Zr_{1.5}Ta_{0.5}O_{12}$	Nb coating	0.5	0.1	52	Rare Metals. 37, 473-479 (2018).
$Li_{6.5}La_{2.5}Ba_{0.5}ZrNbO_{12}$	Ionic liquid	0.2/0.3	0.05/0.075	92/30	Small. 16, 2000279 (2020).
$Li_{6.5}La_3Zr_{1.5}Ta_{0.5}O_{12}$	Cu_3N coating	0.1	0.05	1,000	Energy & Environmental Science. 13, 1, 127-134 (2020).
$Li_{6.5}La_3Zr_{1.5}Ta_{0.5}O_{12}$	Li_3N coating	0.1	0.05	210	Nano Lett. 18, 11, 7414–7418 (2018)
$Li_7La_{2.75}Ca_{0.25}Zr_{1.75}Nb_{0.25}5O_{12}$	Ag coating	0.1	0.05	100	J Power Sources. 419, 91–98 (2019).
$Li_{6.5}La_3Zr_{1.45}Ta_{0.55}O_{12}$	rapid sintering w/ Al_2O_3 coating	0.2	0.033	300	Mater Today. 42, 41–48 (2021).
$Li_{6.28}Al_{0.24}La_3Zr_2O_{12}$	Au coating w/ thermally evaporated Li	0.03	0.0125	70	J Power Sources. 396, 764–773 (2018).

The rate performance of the Li-Sr-1% | LLZTO | Li-Sr-1% symmetric cell was tested at a step-increase current of 0.1, 0.2, 0.3, 0.4, 0.5 mA/cm^2 for 10 cycles at each current density and then move back to 0.4 mA/cm^2 (**Figure 3-10** b). The Li plating/stripping curve at 0.4 mA/cm^2 before and after increasing the current is identical, demonstrating a stable Li-Sr | LLZTO interface during cycling at different currents.

3.5 The Mechanism for the Intense Polarization of Li-Sr | LLZTO | Li-Sr Cells

As shown in **Figure 3-7** c and **Figure 3-10** a, in the first few cycles, a flat and similar potential profile was found for all cells. However, the polarization quickly increases for Li-Sr anodes with Sr content ≥5%, as demonstrated by either an increase of current density or constant current cycling. The interpretation of this strong polarization (**Figure 3-11**) is crucial for the understanding of the failure mechanism. As the current density increases in a linear step in the CCD test, the ionic transportation inside SSEs should also render linear overpotential according to the Nernst-Planck equation, which is not the case for the intense polarization. The increase in Li plating/stripping overpotential at the latest Li plating/stripping stage can potentially be attributed to (1) phase transformation at Li | LLZTO interface between $Li_{23}Sr_6$ and Li_2Sr_3 with different lithiation/delithiation potential (**Figure 3-2**) because the $Li_{23}Sr_6$ phase may change to Li_2Sr_3 in Li stripping process, (2) void formation due to reduced Li atom diffusion by $Li_{23}Sr_6$ phase in bulk Li, and (3) formation of cracks in the bulk Li-Sr anodes due to the large volume changes during Li plating/stripping.

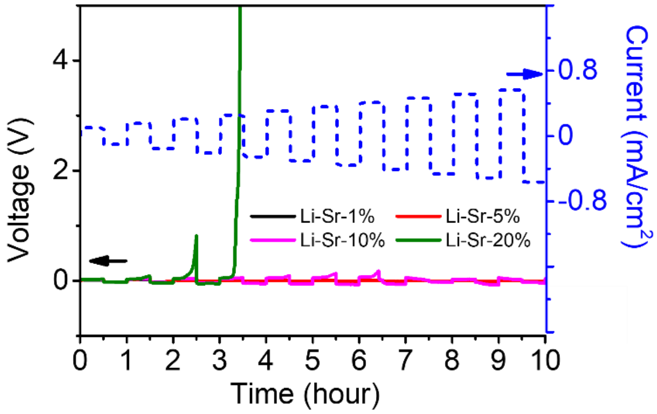

Figure 3-11 The enlarged image for **Figure 3-7** b. The Li plating/stripping behavior for these cells at a step-increase current for 0.5h.

The boosting overpotential can be a sign of overcoming a high energy barrier. We first calculated the equilibrium potentials of $Li_{23}Sr_6$ and Li_2Sr_3 using DFT since the $Li_{23}Sr_6$ phase will convert into Li_2Sr_3 during Li stripping. The equilibrium potentials of Li_2Sr_3 and $Li_{23}Sr_6$ are 27.8 mV and 25.7 mV, respectively (**Figure 3-12** a). The 2.0 mV potential difference cannot cause a significant potential increase at the latest Li stripping state right before short-circuit.

The void formation at Li | LLZTO interface may be responsible for the polarization at the latest Li stripping stage, where the Li vacancy diffusion inside the alloy electrode cannot keep the pace of the current increasing. [39,50] The void evolution is closely related to the Li atom diffusivity in the bulk Li, lithiophilic/lithiophobic property at Li-Sr | SrO doped Li_2O | LLZTO interface. A high CCD of 1.3 mA/cm^2 for Li-Sr-1%

anode at a high capacity of 0.65 mAh/cm^2 is attributed to the bifunctional SrO doped Li_2O interlayer that bonds Li to Li_2O and also reduces the interface energy at Li_2O/LLZTO, decreasing the interface resistance and also suppressing Li dendrite growth. With the increasing of Sr content in Li-Sr anodes, a large amount of $Li_{23}Sr_6$ phase is distributed inside Li, reducing the Li diffusivity, thus forming voids at the early stage of Li stripping thus a low CCD.

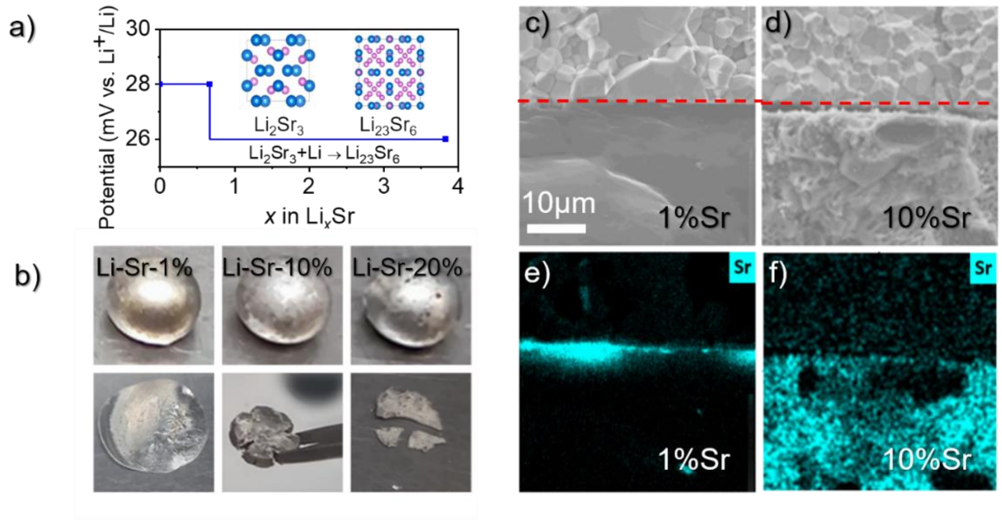

Figure 3-12 Electrochemical and mechanical stability of Li-Sr anodes and Li/LLZTO interface stability. (a) DFT calculation for the equilibrium potentials of Li-Sr alloys. (b) Digital pictures of Li-Sr alloys with significantly different ductility and malleability after press. (c-f) Morphologies and Sr elemental mapping of Li-Sr | SSE interface after 2 cycles with a current density of 0.2 mA/cm^2 and capacity of 0.1 mAh/cm^2.

The cracks formed inside the Li-Sr bulk due to the poor mechanical property of $Li_{23}Sr_6$ phase may also contribute to the low CCD. The brittle $Li_{23}Sr_6$ phase in Li-Sr anodes will crack during the significant volume change in Li plating/stripping, which also blocks the Li atom diffusion to interface and reduce the contact area [49,51] The deformation capability of Li-Sr anodes with different Sr content was evaluated using a facile pressing test. As shown in **Figure 3-12** b, the flow and elastic behavior exhibit noteworthy differences by pressing the Li metal ball, as well as the Li-Sr-alloy balls under 2 MPa. The Li-metal and the Li-Sr-1% alloy demonstrate well ductility and form thin foils with a smooth surface and metallic luster. While the Li-Sr-5%, 10% and 20% alloys render wrinkles, cracks gaps, and even fracture.

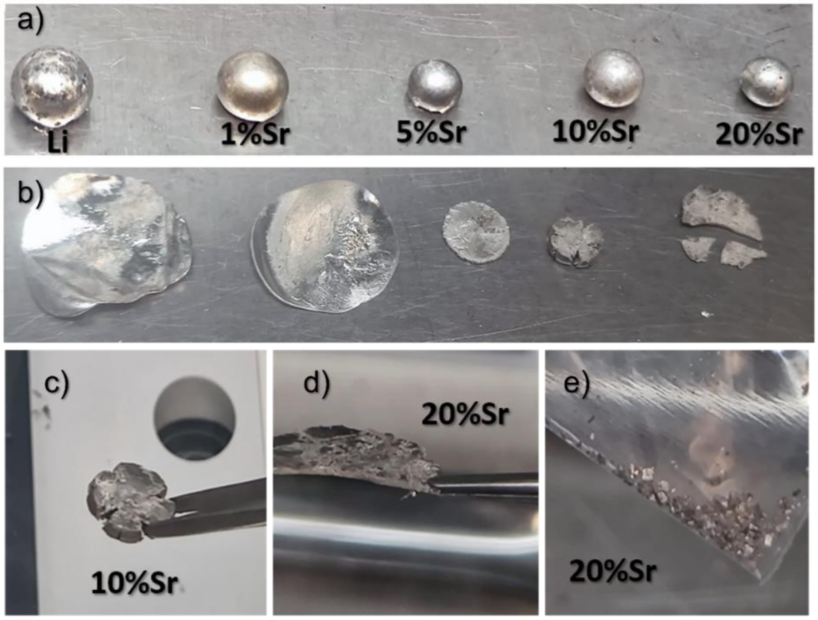

Figure 3-13 Digital pictures of Lithium anode with significantly different ductility and malleability. (a) The electrodes before pressing. (b) The electrodes after pressing. (c) The magnification of the 10% Sr in Li, (d) the fracture of 20% Sr in Li, and (e) the shattered small pieces of the 20% Sr in Li.

As shown in Error! Reference source not found., the pressed Li-Sr-20% has a sharp fracture, and part of it even shattered into small pieces. Although a precise or quantitative study on the deformation property is in absence, the contract is distinct. A significantly worse ductility and malleability can be anticipated with the increase of the Sr ratio in the Li-Sr alloy, which would introduce more detrimental cracks during cycling. The postmortem SEM was taken after the cycling test to analyze the morphology and element distribution evolution of the cross-section of Li-Sr | LLZTO interfaces. As shown in **Figure 3-12** c-f, after Li plating/stripping cycles, Sr is still enriched at Li | LLZTO interface without being pushed away due to the high stability of the SrO anchor, which is totally different from those electron-conducting alloy coating. However, gaps can be clearly seen between the LLZTO and anode for the Li-Sr 10% and 20% cells, as evidence of void formation and contact loss. Cracks and holes also appeared in the Li-Sr anode bulk with Sr >5%.

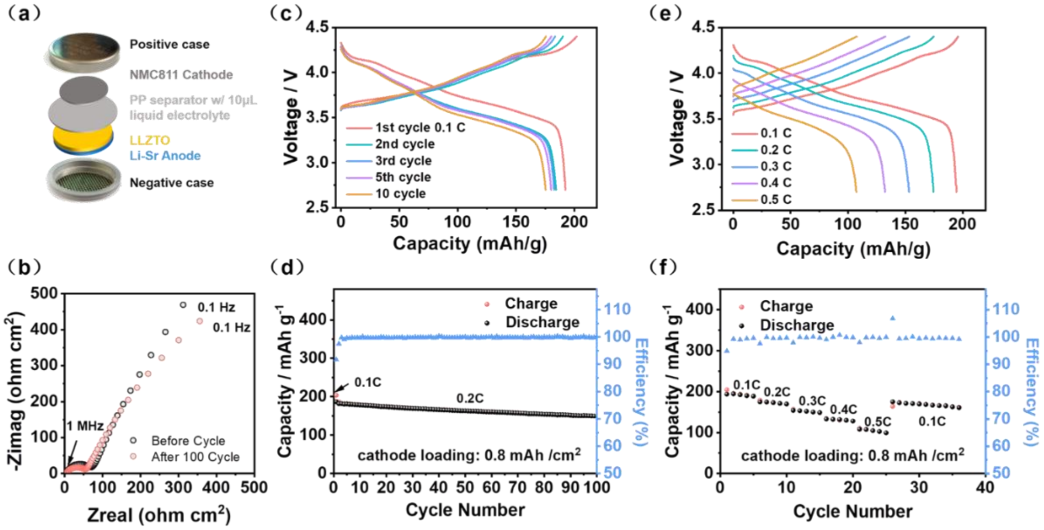

Figure 3-14 Electrochemical performance of Li-Sr-1% | LLZTO | NMC811 cells. a) Schematic diagram of a Li-Sr | LLZTO | NMC811 cells. b) Impedance spectra of the cell tested at room temperature before (black circle) and after 100 cycles (red circle). c, d) The cycle performance for the cell at 0.2 C with cathode loading of 0.8 mAh / cm^2 (0.1 C for the first cycle for activation). e, f) The rate performance for the cell at stepped C-rate.

3.6 Electrochemical Behavior of the Proof-of-Concept Li-Sr | LLZTO | $LiNi_{0.8}Mn_{0.1}Co_{0.1}O_2$ (NMC811) Cells

Since Li-Sr-1% anode shows the high CCD, high cycling stability with LLZTO electrolyte, it was selected for additional cell evaluation. Li-Sr-1% | LLZTO | $LiNi_{0.8}Mn_{0.1}Co_{0.1}O_2$ (NMC811) cells were assembled as the schematic diagram demonstrated in **Figure 3-14** a, with liquid electrolyte wetted cathode interface (**Table 3-3**) to eliminate the cathode side contact influence. The cell provides 192 mAh/g at 0.2 C from 2.7 V to 4.3 V (**Figure 3-14** c) with a capacity retention of 82% after 100 cycles (**Figure 3-14** d). The EIS plots (**Figure 3-14** b) before and after 100 cycles indicate a small resistance reduction without short-circuiting. The initial Coulombic efficiency of 91.68% at 0.1C and average Coulombic efficiency of 99.82% for the rest cycles at 0.2C were displayed. The cell delivered discharge capacities of 192.1, 174.4, 153.0, 132.2 and 107.0 mAh/g at 0.1, 0.2, 0.3, 0.4 and 0.5C (**Figure 3-14** e). The capacity quickly recovered to 175.2 mAh/g when the current was set back to 0.1C (**Figure 3-14** f).

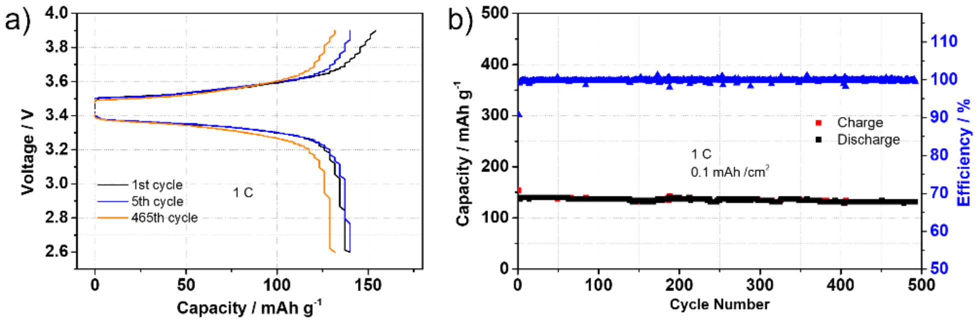

Figure 3-15 Electrochemical performance of Li-Sr-1% | LLZTO | $LiFePO_4$ cells. The loading of the cathode is 0.1 mAh cm^{-2}.

Long cycling of 500 cycles for Li-Sr | LLZTO | $LiFePO_4$ cell is also presented in **Figure 3-15**. These results indicate Li-Sr-1% as a stable anode (**Figure S10**) against LLZTO during cycling. However, further optimizations of liquid-free cathode interface engineering are still needed to realize practical applications of all-solid-state lithium metal batteries (ASSLB).

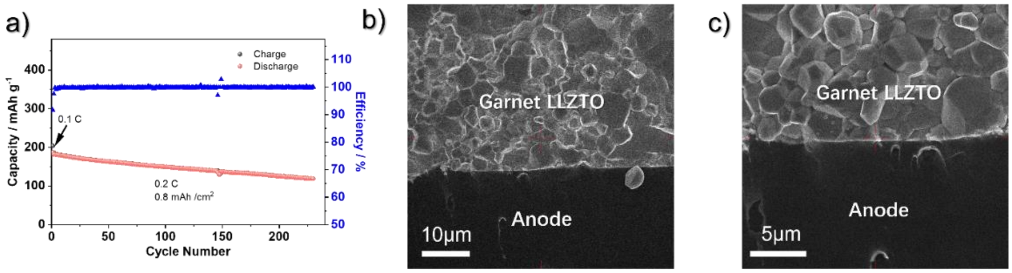

Figure 3-16 a) The cycle performance for the same cell (Li-Sr-1% | LLZTO | NMC811) in **Figure 3-14** d showing the condition before cell test termination at the 230th cycle. b, c) Morphologies of Li-Sr | SSE interface after 230 cycles.

3.7 Conclusion

Solid-state Li metal batteries face two critical challenges of Li dendrite growth and high interface resistance. To suppress Li dendrite growth, interface should be lithiophobic (dendri-phobic), while low interface resistance requires a lithiophilic (wetting) interface. The dilemma between interface wetting and dendrite-phobic was solved with a unique combination of strontium and *in situ* formed SrO, which facilitate a bifunctional lithiophilic/lithiophobic interlayer combining low interface resistance and high dendrite suppression capability.

Table 3-3 Reported cathode loading and wetting method, cycling rate and time for the prove-of-concept cells in planar garnet type solid-state electrolytes. (Operating at room temperature/25℃ without further notice)

Composition	**Anode Methods**	**Cathode and Loading (per cm^2)**	**Wetting Method**	**Cycling rate and Cycles**	**Ref.**
$Li_{6.5}La_3Zr_{1.5}Ta_{0.5}O_{12}$	Sr bifunctional layer	NMC811, 0.8 mAh	liquid electrolyte (10 µL)	0.2C, 100	This work
		LFP, 0.1 mAh		1C, 500	
$Li_{5.9}Al_{0.2}La_3Zr_{1.75}W_{0.25}O_{12}$	Graphite interface	NCM523, 0.9 mg	slurry w/ ionic liquid	0.5C, 500	Acs Energy Lett. 3, 1212–1218 (2018).
$Li_{6.5}La_3Zr_{1.5}Ta_{0.5}O_{12}$	Li-C composite	LFP, --	PVDF-HFP film w/ 10 µL liquid electrolyte	0.5C, 100	Advanced Materials. 31, 1807243 (2019).
$Li_{6.5}La_{2.5}Ba_{0.5}ZrNbO_{12}$	Ionic liquid	LFP, 2.5mg	ionic liquid (2 µL)	0.05 mA cm^{-2}, 45	Small. 16, 2000279 (2020).
$Li_{6.5}La_3Zr_{1.5}Ta_{0.5}O_{12}$	Cu_3N coating	LCO, 2mg	slurry w/ ionic liquid	0.2C, 300	Energy & Environmental Science. 13, 1, 127-134 (2020).
$Li_{6.5}La_3Zr_{1.5}Ta_{0.5}O_{12}$	Li_3N coating	LFP (40 °C), 2mg	slurry w/ PEO and acetonitrile	0.1 mA cm^{-2}, 200	Nano Lett. 18, 11, 7414–7418 (2018)
$Li_7La_{2.75}Ca_{0.25}Zr_{1.75}Nb_{0.25}5O_{12}$	Ag coating	LCO, 0.45mg	slurry w/ ionic liquid	0.2C, 100	J Power Sources. 419, 91–98 (2019).
$Li_{6.28}Al_{0.24}La_3Zr_2O_{12}$	Au coating w/ thermally evaporated Li	LCO, --	liquid electrolyte (10 µL)	0.05C, 70	J Power Sources. 396, 764–773 (2018).
$Li_7La_{2.75}Ca_{0.25}Zr_{1.75}Nb_{0.25}5O_{12}$	Al_2O_3 coating	LFMO, --	a tiny amount of liquid electrolyte	0.1 C	Nat Mater. 16, 572–579 (2016).

SrO is stable with Li and facilitates the contact between anode and LLZTO by reducing the interface energy between Li_2O and LLZTO. It serves as an anchor which let the Li to be deposited between the interfacial layer and the anode that (1) suppress the lithium nucleation and dendrite propagation on SSE; (2) keep the interfacial layer stable on the anode | SSE interface instead of being pushed away; (3) reduce the resistance of the Li_2O lithiophobic layer but kept its lithiophobic nature; (4) having high affinity to garnet. An optimized Li-1% Sr alloy anode | LLZTO can synergistically achieve a low interface resistance and high Li dendrite suppression capability, as evidenced by a high CCD of 1.3 mA/cm^2 at 0.65 mAh/cm^2 and a stable cycle of 1,000 cycles (1,000 h) under 0.5 mA/cm^2 at room temperature. This work provides a new strategy and sheds light on enhancing the performance of SSLBs.

Chapter 4 High Interface Energy Enabled Highly Stable Garnet-based Lithium Metal Solid-State Batteries

4.1 Introduction

Solid-state lithium metal battery (SSLB) is considered as one of the most promising next generation batteries to power the growing numbers of electric vehicles, owing to its high energy density and high safety origin from the lithium metal anode (LMA) and solid-state electrolyte (SSE) respectively. Among various SSEs, garnet-type Li-ion conductor $Li_7La_3Zr_2O_{12}$ (LLZO) and it variants, are been extensively developed for their high ionic conductivity (8×10^{-4} S cm^{-1} with Nb doping at room temperature), low electronic conductivity (~ 10^{-8} S cm^{-1} at room temperature), wide electrochemical window, and high shear modulus over 100 GPa that was believed able to block the dendrite growth theoretically.

The most intuitive difference between SSE and its previous generation counterpart liquid electrolyte is the lack of flowing medium that adapts the shape changes and keeps a continuous conducting channel. Thus, the priority issue to be fixed for SSLB is to facilitated the solid-solid contact between the solid-electrolyte and the electrode. What makes the matter worse for the LMA is its nature of one monolithic piece instead of particles. This means a 3D contact by mixing SSE particles with active material particles in the electrodes like most cathodes and silicon anode can do will no longer be a solution for lithium metal. Instead, the contaare between the plane SSE and plane LMA is in a 2D geometry that is more vulnerable once voids or cracks froms and lead directly to the loss of contact. Tremendous efforts had been made in the past decade to facilitate and maintain the solid-solid contact between the SSE and the LMA aiming at diminish or even eliminating the interfacial impedance. Added-on external pressure works but up to hundreds MPa pressure is not practical for the application of SSLMB in real life scenarios such as electric vehicles. Making the metal electrodes flowable such as Na-K alloy and liquid lithium solution also tackles the problem intrinsically, but the choices are extremely limited[65] for room temperature flowable electrodes. In particular, even for the garnet SSE with a nature of rigidity of ceramic and non-wettability with lithium, the interfacial impedance can be reduced from thousands to single-digit Ω cm^2 with proper interface engineering.

Recent studies have demonstrated that the interface impedance can be almost eliminated in SSLB. However, the dendrite suppression capability and cycling stability are still far from the requirement of the practical applications. This reminds us the “interface impedance” may not be the golden target and the critical properties of the interface towards dendrite suppression instead of solely low impedance demands a more clear determination. Here, we screening the interface candidates aiming at properties directly contributes to the dendrite suppression: 1) the Gibbs energy for the reaction between Li and the candidate (for metal oxides: $nLi + MO_m \leftrightarrow M + nLiO_{m/n}$) should be as positive as possible; 2) the interface energy against lithium should be as high as possible. The former guaranteed a thermodynamic stable interface that keeps the designed metal oxides interlayer instead of being reduced by lithium upon cycling. The latter established a large energy barrier for lithium dendrite to pierce through against the dynamic energy input from overpotential and volume changing during the lithium striping and plating.

In this study, we present a $LiYO_2$ as a highly thermodynamical stable candidate for the interface between SSE and LMA based on the critical properties of aforementioned Gibbs energy and interface energy. Li | $Li_{6.5}La_3Zr_{1.5}Ta_{0.5}O_{12}$ (LLZTO) interface with $LiYO_2$ as the interlayer was successfully established, which endows the symmetric cells a high critical current density of 1.15 mA cm^{-2}, a critical capacity of 4.2 mAh cm^{-2} at 0.1 mA cm^{-2} and a long cycle life of 600 cycles under 0.5 mA cm^{-2}/0.25 mAh cm^{-2}. This work represents a significant advancement in designing the interface for SSE | LMA by providing critical parameters of the interface, which would advance the design of high performance SSLBs.

4.2 Experimental

The Li-Y alloy anode was prepared by a molten lithium method in a glove-box. Initially, lithium foil (Alfa) and Y power (Sigma, 99.5%) was mixed in a shallow stainless-steel crucible under 350℃ with weight ratio of 7:1, 3:1 and 1:1. The molten alloy will be stirred for more than 10 minutes to ensure a homogeneous reaction. The as-synthesized LLZTO electrolyte pellet was cleaned by mechanical dry-polishing using 400 grits, 1500 grits and 3000 grits sandpapers consequently. The polished LLZTO pellet was directly immersed in the crucible with the molten alloy and the anode will be attached on the LLZTO pellet within around 10 seconds. After cooling down to room temperature, the residual metal attached on the side surface of LLZTO pellet will be polished off with sandpaper.

XPS was conducted on a high sensitivity Kratos Axis 165 X-ray photoelectron spectrometer with Al Kα radiation. All binding energy values were referenced to the C1s peak to 284.8 eV. The surface of the sample (anode side) after scraper-cleaning is defined as the 0 depth. The sample was directly moved from Ar atmosphere to the XPS chamber with a vacuum transfer container to avoid exposure to the air. Peak fitting and relative atomic percentage estimation were done using CasaXPS software.

4.3 Design of the Interlayer Towards Dendrite Suppression

Li-M alloy (M = metal elements) can effectively increase the wettability with the garnet SSE. However, the formed electronically conducting interface causes directly contact between the e^- and the SSE and let the lithium plating happen right on top of the SSE. This have two potential hazes: 1) the designed interface would be push away from the surface by the newly plated lithium and the interface will be invalid upon cycling; 2) the accumulated electron near the SSE can form a negative electric field and force the Li^+ expulse out of the bulk SSE to form lithium metal dendrite.[66] Thus, as mentioned earlier we aims on an interface of metal oxide (MO_m) that contract a ion or ion/electron mix interface.

To stay spatially stable against being pushed backwards is not enough for a successful IL. Thermodynamically stability of MO_m against being reduced by lithium metal to M is another key to keep the interface layer stable upon cycling. According to the theoretical equilibrium potential for the reaction between binary metal oxides and lithium metal (calculated from the Gibbs energy for the reaction between Li and the metal oxides ($nLi + MO_m \leftrightarrow M + nLiO_{m/n}$)), and Gibbs free energy for the formation ($\Delta_f \boldsymbol{G}$) of the metal oxides (**Table 4-1**), the relatively stability against Li can be preliminarily estimated. Y2O3 is one of the very few metal oxides that is stable against Li with a negative equilibrium potential, which inspires us to dope Y into the lithium metal to form a thermodynamically stable interlayer.

Table 4-1 The theoretical equilibrium potential for the reaction between binary metal oxides and lithium metal, and Gibbs free energy of formation ($\Delta_f G$).[62]

$\boldsymbol{MO_m}$	$\Delta_f \boldsymbol{G}$ (kJ/mol)	Theoretical equilibrium potential (V)	$\boldsymbol{MO_m}$	$\Delta_f \boldsymbol{G}$ (kJ/mol)	Theoretical equilibrium potential (V)
V_2O_5	-1419	1.441	SiO_2	-856	0.694
MnO_2	-465	1.708	SnO_2	-520	1.582
Fe_2O_3	-742	1.631	SrO	-561	0.005
CoO	-214	1.802	Y_2O_3	-1817	-0.226
NiO	-212	1.954	Al_2O_3	-1582	0.180
CuO	-128	2.248	ZnO	-320	1.252

4.4 Construction and Characterization of the Y doped Interlayer

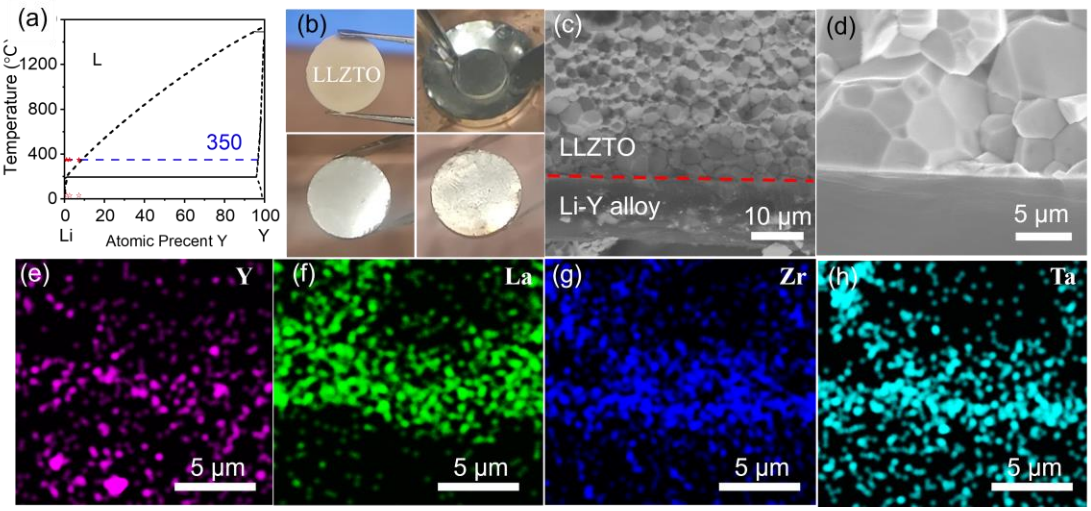

Figure 4-1 Characterization of the symmetric Li-Y|LLZTO|Li-Y cells. (a) Li-Y Phase diagram. The red stars indicate the ratio of Li-Y alloy studied (7:1, 3:1, and 1:1); (b) Digital pictures for the Li-Y|LLZTO|Li-Y symmetric cells assembling process; (c, d) cross-sectional SEM image of the Li-Y|LLZTO interface. (e-h) EDS mapping of the Li-Y|LLZTO interface.

Li-Y alloy with three different compositions (7:1, 3:1, and 1:1, marked in Figure 1a) was synthesized and attached onto garnet LLZTO pellets using a molten Li method at 350°C. As demonstrated in **Figure 4-1** b, after immersing the LLZTO pellets into the molten Li alloy anode, the anode can be attached onto the surface of the solid electrolyte easily. After cooling to room temperature, the anode delivered a flat homogenous texture with metallic luster. The wettability of Li-Y to LLZTO solid electrolyte was demonstrated through this attachment process, and further confirmed through scanning electron microscopy (SEM). As shown in **Figure 4-1** c-d, intimate contact without obvious void or gap was observed between LLZTO and Li-Y. The position of the interface was further confirmed using the energy-dispersive X-ray spectroscopy (EDS) mapping (**Figure 4-1** e-h).

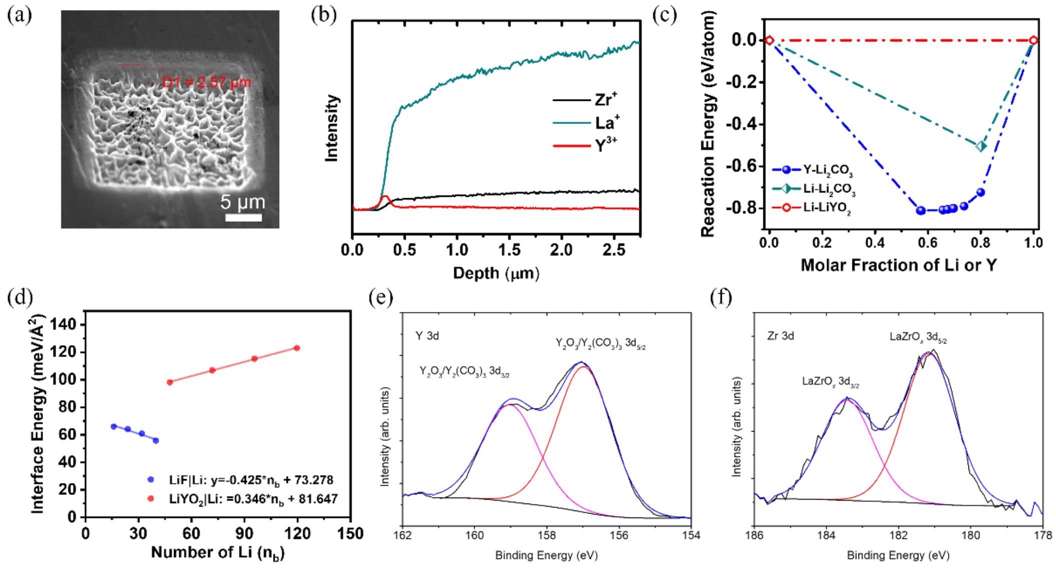

Figure 4-2 Characterization of the interface chemistry for the Li-Y | LLZTO interface (the weight ratio of Y to Li was 3:1). (a) SEM image (top view) for the Ga^+ ion beam sputtered carter of the interface. (b) Depth profiling of spatial distribution of Zr, La, and X element at the interface. (c) Thermodynamic equilibrium reaction energy for the X-Li_2CO_3, Li-Li_2CO_3, and Li-$LiXO_A$ interfaces. (d) The calculated interface energy (γ) *vs.* the number of Li-metal formula units by DFT. High-resolution XPS of (e) X 3d, and (f) Zr 3d spectra of the interface.

Further characterizations were conducted to investigate the interface chemistry and evaluate the thermodynamic stability against dendrite penetration. The depth profiles of Zr^+, $Y3^+$ and La^+ were acquired by *ex situ* time-of-flight secondary ion mass spectrometry (ToF-SIMS). A 20 μm × 20 μm area (**Figure 4-2** a) was sputtered with Ga+ ion focused ion beam (FIB) on top of the SSE, in which Y^{3+} show peak at a depth around 0.3 μm with the followed by a rise of La^{+}, indicating the aggregation of Y^{3+} at the Li-Y | LLZTO interface (**Figure 4-2** b). X-ray photoelectron spectroscopy (XPS) was performed with Ar^{+} ion gun etching to identify the component at Li-Y | LLZTO interface. The etching depth of the interface was confirmed with the Zr *3d* spectra (**Figure 4-2** f) to make sure the interface has been reached. From the Y *3d* spectra (**Figure 4-2** e), the peaks for $3d_{5/2}$ and $3d_{3/2}$ of the oxide or carbonate of Y were located at 159.03 eV and 157.04 eV, respectively. As a cross-validation and further identification between the oxide and carbonate, calculation based on density functional theory (DFT) was conducted to find the potentially thermodynamically stable compound on the interface. The result was plotted in the "convex-hull" plot in **Figure 4-2** c, in which a stable compound should have a lower formation energy than the linear combination of any other phases in the system, i.e., being on a convex hull. As shown by the blue and green curves, there are more stable compounds in both Y-Li_2CO_3 and Li-Li_2CO_3 systems. On the contrary, Li-$LiYO_2$ demonstrates a straight line in red without any more stable compound. These confirmed the most stable form of Y should be its oxide form: $LiYO_2$, and $LiYO_2$ should be the main functioning species on Li-Y | LLZTO interface.

To further evaluate the dendrite suppression capability of $LiYO_2$, the interface energy (γ) of the $LiYO_2$ against Li was analyzed based on DFT simulation. On an energy perspective, interfaces with high γ will require high energy penalty for lithium to penetrate in a dendritic form, and thus promoting lateral lithium motion along the interface.[67] In previous reports, LiF has been recognized as having the highest γ among all lithium compounds that can be formed in the electrolyte | anode interface.[32] LiF-rich interfaces have been used in multiple systems and demonstrated exceptional performance of dendrite suppression. [68–70]

As shown in **Figure 4-2** d, the interface energy obtained from the intercept of the fitted line was 81.65 meV/Å for $LiYO_2$, which is even higher than that of LiF. The $LiYO_2$ with extremely high interface energy against lithium can effectively suppress Li dendrite growth.

Here, the high interface energy of $LiYO_2$ against lithium guaranteed a dynamic stable interlayer that suppressed the dendrite penetration. While the negative theoretical equilibrium potential of oxide form of Y against lithium affirmed a thermodynamic stable interlayer that would not be reduced back to an electron-conducting Y metal layer by lithium. With these two unique properties, the Y formed a solid "Great Wall" to protect the SSE from decomposition and Li dendrite penetration.

4.5 Lithium Dendrite Suppression Capability of $LiYO_2$ Interphase

Electrochemical characterizations of the Li-Y|LLZTO|Li-Y cells were conducted to confirm the lithium dendrite suppression capability of the designed interlayer with high thermodynamic stability. In order to select the Li-Y alloy with optimized composition, electrochemical impedance spectra (EIS) were conducted to measure the interfacial resistance before cycling, and critical current density (CCD) tests was conducted to evaluate the lithium dendrite suppression capability.

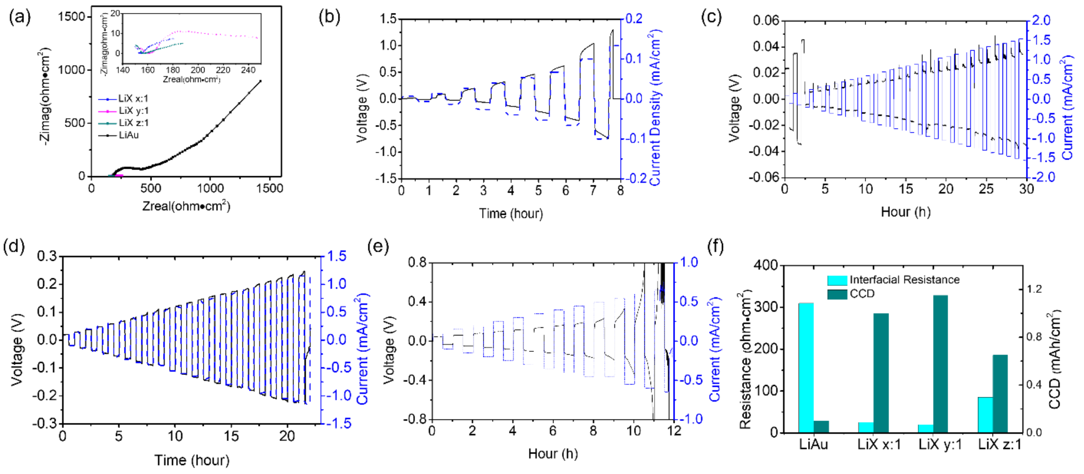

Figure 4-3 Electrochemical characterizations of the symmetric Li-X|LLZTO|Li-X cells at room temperature without extra pressure. (a) EIS plot of Li-X|LLZTO|Li-X and Li-Au|LLZTO|Li-Au symmetric cells; The detailed EIS for different ratio of X were shown in the inset figure. CCD measurement for the (b) Li-Au|LLZTO|Li-Au cell, and (c-e) Li-X|LLZTO|Li-X (the weight ratio of X to Li was (c) x:1, (d) y:1 and (e) z:1, respectively) at step-increased current densities with a fix charging/discharging time of 0.5 h. (f) The summary of interfacial resistance and measured CCD for the symmetric cells with Li-Au and Li-X anodes.

As shown in **Figure 4-3** a and f, the resistance of the electrolyte pellets, including both bulk and grain boundary, are represented as the first semicircles, which are around 150~165 Ω cm^2 regardless the interface treatment. The interface resistances of Li-Y|LLZTO|Li-Y cells are around 20 - 85 Ω cm^2, which are significantly smaller compared to the Au sputtered one (314 Ω cm^2). The CCD measurement shows that the Li-Y |LLZTO| Li-Y (the weight ratio of Y to Li was 3:1) can reach a high CCD of 1.15 mA cm^{-2} (**Figure 4-3** d), which is 10 times higher than that of Li-Au |LLZTO| Li-Au (0.1 mA cm^{-2}, **Figure 4-3** b). The comparison of the Li-Au anode and Li-Y anode with different Li/Y weight ratios is shown in **Figure 4-3** f, among which the Li-Y |LLZTO|Li-X (the weight ratio of Y to Li was 3:1) shows the smallest interface resistance and highest CCD (**Figure 4-3** c-e).

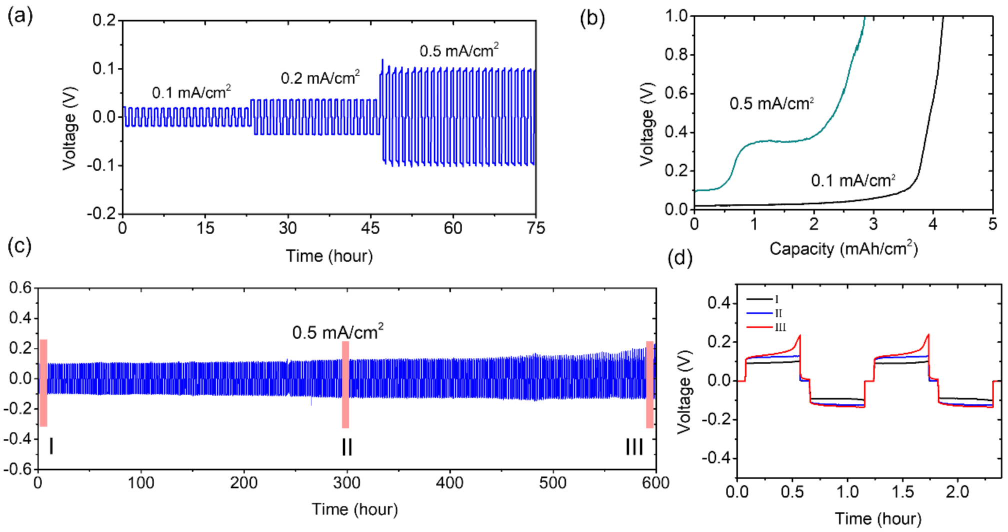

Figure 4-4 Electrochemical characterizations of the composition optimized Li-Y anode. (a) The voltage profile of Li-Y |LLZTO| Li-Y (the weight ratio of Yto Li was y:1) cell at step-increased current densities. (b) Voltage profile for Li-Y |LLZTO| Li-Y (the weight ratio of Y to Li was 3:1) cells when Li was stripped at a constant current density of 0.1 and 0.5 mA cm^{-2} with a cut-off voltage of 1.0 V. (c) Galvanostatic cyclic performance of the symmetric Li-Y |LLZTO| Li-Y (the weight ratio of Y to Li was 3:1) cells at 0.5 mA cm^{-2} and the corresponding details for the regions I, II, and III were shown in (d).

To further study the Li plating/stripping behavior of Li-Y anode (the weight ratio of X to Li was 3:1), the critical capacity of cell was tested. When Li-Y |LLZTO| Li-Y was stripped at constant current densities of 0.1 and 0.5 mA cm^{-2} with a cut-off voltage of 1.0 V, the critical capacities of 4.2 and 2.8 mAh cm^{-2} were achieved (**Figure 4-4** b), which can fully meet the capacity requirement for practical application of Li-metal anode in all-solid-state battery. The optimized Li-Y |LLZTO|

Li-Y (the weight ratio of Y to Li was 3:1) shows stable cyclic performance at different current densities of 0.1, 0.2 and 0.5 mA cm^{-2} without any abrupt overpotential increase (**Figure 4-4** a). Besides, a long cycle life of 600 hours under 0.5 mA cm^{-2}/0.25 mAh cm^{-2} can also be achieved (**Figure 4-4** c-d). The superior electrochemical performances of Li-Y |LLZTO| Li-Y cell demonstrate the effectiveness of our design principle for a thermodynamically stable interlayer.

4.6 Electrochemical Performance of Full Cells

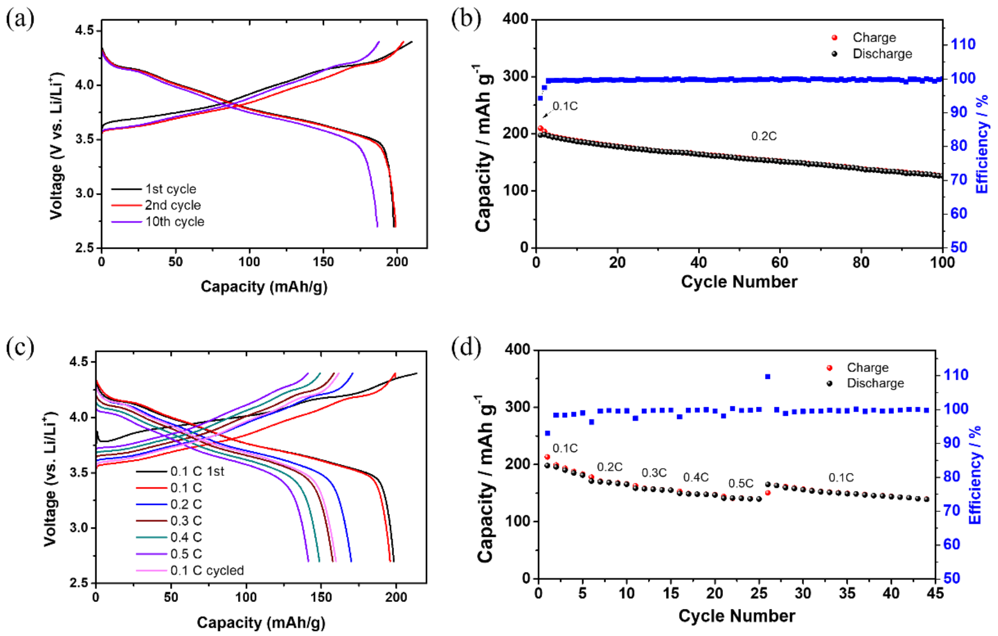

Figure 4-5 Electrochemical performance of proof-of-concept Li-Y | LLZTO | NMC811 cells. (a, b) The cycle performance for the cell at 0.2 C with cathode loading of 0.8 mAh cm^{-2} (0.1 C for the first cycle for activation). (c, d) The rate performance for the cell at step-increased C-rate.

Since Li-Y anode shows high CCD and high cycling stability with LLZTO electrolyte, it was selected for additional full cell performance evaluation. Li-Y | LLZTO | $LiNi_{0.8}Mn_{0.1}Co_{0.1}O_2$ (NMC811) cells were assembled with liquid electrolyte wetted cathode interface to eliminate the contact effect on cathode side. The cell was activated at 0.1C in the first cycle and then cycled at 0.2C in the following cycles. Li-X | LLZTO | NMC811 cell provides reversible capacity of 186.4 mAh g^{-1} at the 10th cycle of 0.2 C under cut-off voltage of 2.7~4.3 V (**Figure 4-5** a) with a capacity retention of 80% after 100 cycles with average Coulombic efficiency of 99.77% (**Figure 4-5** b). Li-Y | LLZTO | NMC811 cells also shows excellent rate capability. As shown in **Figure 4-5** c-d, The Li-X | LLZTO | NMC811 cells display capacity of 198.2 mAh g^{-1} at 0.1 C, 170.0 mAh g^{-1} at 0.2 C, 157.6 mAh g^{-1} at 0.3 C, 148.7 mAh g^{-1} at 0.4 C and 141.0 mAh g^{-1} at 0.5 C. When the current recovered back to 0.1 C, reversible capacity of 159.7 mAh g^{-1} can also be remained. The superior cyclic performance and rate capability of Li-Y | LLZTO | NMC811 cells can fully demonstrate the superior stability of Li-Y alloy anode to LLZTO electrolyte. However, further optimizations of liquid-free cathode interface engineering are still needed to realize practical applications of all-solid-state lithium metal batteries.

4.7 Conclusion

Overall, a high stable $LiYO_2$ interface was established and studied in this chapter to validate our design principle of high interface energy for SSE | Li interface. A high critical current density of 1.15 mA cm^{-2}, a critical capacity of 4.2 mAh cm^{-2} at 0.1

mA cm-2 and a long cycle life of 600 cycles under 0.5 mA cm^{-2}/0.25 mAh cm^{-2} was achieved in the lithium symmetric battery tests to demonstrate the dendrite suppression capability of the interface. This work sheds new insight on the rational design of the interface for SSLBs with high performance.

Chapter 5 Void Suppressive Lithium Anodes for All-Solid-State Batteries

5.1 Introduction

All-solid-state lithium metal batteries have garnered great attention due to their high energy density and safety.[71–73] However, SSLBs suffer from high interface resistance and severe lithium dendrite growth, impeding their applications.[74–78] The initial interfacial resistance and overpotential can be reduced by enhancing the wettability between lithium and solid-state electrolyte (SSE) through removing the surface contaminants[79] and coating lithophilic layer[80,81], enabling stable lithium cycling at a low rate and capacity. However, the interfacial overpotential dynamically increases due to the void evolution at the Li|SSE interface during cycling.[50,82,83] When the interfacial overpotential exceeds the critical overpotential (COP) of SSE[65,84,85], chemomechanical degradation[86] will occur, accelerating lithium dendrite propagation inside SSE.

Lacking an understanding of the origin of void evolution, the reported preengineered methods cannot effectively eliminate dynamic void formation and dendrite propagation. The dynamic strategies of suppressing void evolution are mainly limited to applying stacking pressure[87–89] and raising the operating temperature[39], which are unfavorable for battery integration due to the introduced weight and cost to the battery stacks. To develop an SSLB that can cycle at a high rate and a high capacity under low pressure and room temperature, a fundamental mechanism of the void evolution[90,91] should be revealed, and corresponding effective strategies are urgently needed.

In this study, we systematically investigated the lithium dendrite formation mechanism and correlated it with the interfacial overpotential induced by void formation. To enhance the void suppression capability (VSC) of the lithium anode, lithium diffusion was accelerated over 10 times by refining the grain through solidification of molten Li with a Mg-La inoculant (LiMgLa) additive, simultaneously enhancing the wettability. The refined LiMgLa anode demonstrated a high VSC of 4.1 $mA^2 \cdot h \cdot cm^{-4}$, which is over 10 times higher than that of the LiMg alloy (0.4 $mA^2 \cdot h \cdot cm^{-4}$). The LiMgLa anodes enable a high critical current density (CCD) of 2.2 $mA \cdot cm^{-2}$ at a high capacity of 1.1 $mAh \cdot cm^{-2}$ with the $Li_{6.5}La_3Zr_{1.5}Ta_{0.5}O_{12}$ (LLZTO) electrolyte, improving the rate and capacity simultaneously. The LiMgLa|LLZTO interface evolution during lithium stripping is simulated using a phase-field model, providing dynamic insight into the void formation process at the dependency of current density and diffusivity.

5.2 Experimental

5.2.1 Synthesis of the Alloys as Anodes

The anodes were prepared by a molten lithium method in a glovebox with an argon-filled atmosphere with moisture and oxygen concentrations <0.1 ppm. The lithium foil was placed in a stainless-steel container and heated at 350 °C on a hot plate. The native surface film was carefully removed to present a shiny liquid lithium. To prepare the Li-Mg alloy, Mg powder was added slowly to the molten lithium according to the molar ratio and vigorously stirred for approximately 10 minutes. Then, the Li-Mg alloy was cooled to room temperature by moving from the hot plate. For the Li-Mg-La alloy, the La powder was added to the molten Li-Mg alloy at 350 °C by the weight ratio of Mg and La. The following procedures for the Li-Mg-La alloy are similar to those for Li-Mg.

5.2.2 Electrochemical Characterizations

The critical current density (CCD) measurements were conducted with stepwise increased current densities (0.1, 0.2, 0.5, 0.7, 1.0, 1.2, 1.5, 1.7, 2.0, 2.2 $mA \cdot cm^{-2}$), and each step was fixed as 30 minutes of charging/discharging. The profiles for anodic dissolution were tested with a voltage cutoff of 5.0 V at various current densities.

A commercially available NMC811 cathode with a loading of 1.6 $mAh \cdot cm^{2}$ was provided by SAFT as the cathode for the SSLBS. 1 C was defined as 200 $mA \cdot g^{-1}$.

5.2.3 Molecular Dynamics Simulations

All the classic molecular dynamics (MD) simulations conducted in this work were performed using the Large-scale Atomic/Molecular Massively Parallel Simulator (LAMMPS, http://lammps.sandia.gov) software.[92] The modified embedded atom method (MEAM) potentials were used for Li and LiMg. A lithium vacancy concentration of 2% is introduced to the Li and LiMg bulk and slabs. The MD simulations were performed in the NPT ensemble at p = 1 atm and T = 298 K with a Nose–Hoover barostat and thermostat for 5 ns with a time step of 1.0 fs to integrate the equations of motion. Periodic boundary conditions were used, and electrostatic interactions were considered using the particle–particle particle–mesh scheme in k-space. Subsequently, 10 ns equilibration MD runs were performed in the NVT ensemble, followed by 10 ns NVT production runs that were used to extract structural properties. The diffusion coefficients (D) were defined as the mean squared displacement (MSD) over time as

$$\mathrm{D} = \lim_{t\to\infty} \frac{\langle [r(t)]^2 \rangle}{6t} \tag{1.}$$

The average MSD, $\langle [r(t)]^2 \rangle$, was calculated by equation (3):

$$\langle [r(t)]^2 \rangle = \frac{1}{N} \sum_i \langle [r_i(t+t_0)]^2 - [r_i(t_0)]^2 \rangle \tag{2.}$$

where $r_i(t)$ is the displacement of the i-th Li-ion at time t and N is the total number of ions in the system. The coefficients are finally attained from the slope of the average MSD vs. time plot for each temperature.

5.2.3 Phase-Field Model and Parameters

The phase-field method has been widely applied to dendrite growth in liquid and solid-state electrolytes, showing great capability in revealing the underlying mechanism for energy storage devices. However, the evolution of the anode during anodic dissolution has not been investigated. To probe the morphological evolution of the LiMg and LiMgLa anodes during the stripping process, the phase-field model[93,94] is simulated using a finite element method on the COMSOL Multiphysics 5.6 platform under an adaptive grid.

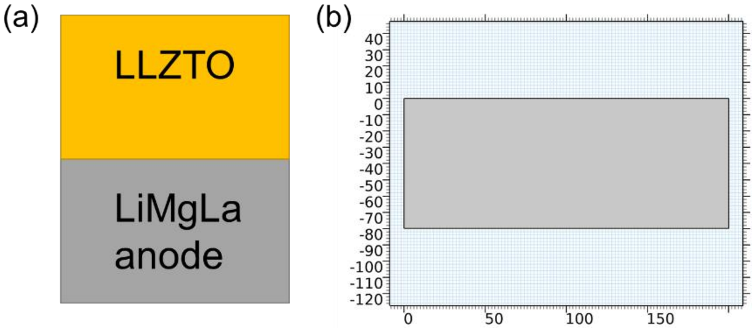

Figure 5-1 (a) Scheme of the modeled LiMgLa and LLZTO interface and (b) the geometry of the anode in COMSOL Multiphysics. The physics in the LLZTO pellet has not been solved

The size of the lithium anode (**Figure 5-1**) is set to 200 × 80 μm, and the mesh size is set as 50 × 20 with a minimum grid spacing of d_{min} = 4 μm. Since the amount of doped Mg and La is quite small, the Li bulk concentration is employed as $c_0 = 7.64 \times 10^4$ mol·m^{-3}. All the parameters are normalized to a characteristic energy density $E_0 = c_0RT = 1.89 \times 10^8$ J·m^{-3}, a characteristic length l_0 = 1 μm, and a characteristic time step $\Delta t_0 = 10$ s. The detailed parameters and their normalized values are listed in **Table 5-1**.

Table 5-1 Phase-field simulation parameters and their normalized values.

Parameter	**Real value**			**Normalized value**		
	Symbol	LiMg value	LiMgLa value	expression	LiMg value	LiMgLa value
Diffusion coeff. in bulk lithium	D_{Li}	7.5×10^{-11} cm^2/s	1.2×10^{-9} cm^2/s	$D_{Li}/(l_0^2/t_0)$	0.075	1.2
Diffusion coeff. in void	D_v	0	0	$D_v/(l_0^2/t_0)$	0	0
Diffusion coeff. at surface	D_s	7.5×10^{-8} cm^2/s	7.5×10^{-6} cm^2/s	$D_s/(l_0^2/t_0)$	75	1200
Gradient energy coefficient	κ	1×10^{-6} J/m	5×10^{-6} J/m	$\kappa/(E_0 l_0^2)$	0.0528	0.264
Barrier height	W	4.95×10^4 J/m^3	4.95×10^4 J/m^3	W/E_0	0.0264	0.0264
Exchange current density	i_0	737.15 A/m^2	737.15 A/m^2	$i_0 t_0/(c_0 F l_0)$	1	1

To describe the diffuse interface in the phase-field model, a continuous phase-field variable ξ is introduced, which is a physical correspondence to the dimensionless concentration of Li atoms $\tilde{c} = \xi = c/c_0$. Here, c and c_0 are the real-time and initial lithium concentrations, respectively. ξ =1 represents the electrode, while ξ =0 represents the void, and 0<ξ<1 represents the interface between these two phases. From the Ginzburg-Landau theory, a local chemical potential must be derived as a function of concentration. With F representing the free energy function, the chemical potential can be represented as a variational derivative as

$$\mu = \frac{\delta \mathrm{F}}{\delta c} \tag{3.}$$

Since the concentration, c, is a conserved field, the mass conservation equation should be satisfied:

$$\frac{\partial c}{\partial t} = -\nabla . \vec{J} \tag{4.}$$

The flux, $\vec{J}$, can be defined as

$$\vec{J} = -\mathrm{M}\nabla . \mu \tag{5.}$$

where M is the diffusion mobility. The equation of motion for the concentration field can be obtained by combining equations (3) and (4):

$$\frac{\partial c}{\partial t} = \nabla \left(M \nabla \frac{\partial F}{\partial c} \right) \tag{6.}$$

This is the Cahn-Hilliard equation, which represents the governing equation for concentration. The Ginzburg-Landau free energy functional, F, is defined as:

$$F = \int_V \left[f(\xi) + \frac{1}{2}\kappa (\nabla \xi)^2 + \rho\phi \right] dV \tag{7.}$$

where f is the chemical free energy density, κ is the coefficient of gradient energy, ρ is the electrical charge density and ϕ is the electric potential. Then, the time evolution of ξ in the phase-field model can be derived and given by:

$$\frac{\partial \xi}{\partial t} = M\nabla^2 \left(\frac{\partial f}{\partial \xi} - \kappa(\nabla\xi)^2\right) \tag{8.}$$

An arbitrary double well function $f(\xi) = W\xi^2(1-\xi^2)$ is used to describe the two equilibrium states for the electrode ($\xi = 1$) and the void ($\xi = 0$). W represents the barrier height. $h(\xi) = \xi^3(6\xi^2 - 15\xi + 10)$ is an interpolating function representing the fraction of material participating in the electrochemical reactions. The diffusion coefficient at the interface depends on the phase parameter $D^{eff} = D_{Li}h(\xi) + 4D_s h(\xi)\big(1 - h(\xi)\big) + D_v(1 - h(\xi))$, where D_{Li}, D_s, and D_v are the lithium diffusion coefficients for the bulk, surface, and void, respectively.

To simulate the anodic dissolution process with a constant current density, the following rule is adapted to distribute the local current density (i) at the anode and SSE interface.

$$i = I_{app}\frac{\int_{S_0} \xi ds}{\int_{S} \xi ds} \tag{9.}$$

where I_{app} is the applied current density and S_0 and S are the initial and real-time contact areas at the electrode/electrolyte interface, respectively.

The reaction overpotential, η, is calculated by the Butler–Volmer equation:

$$i = -i_0 \left\{ \xi exp\left[\frac{(1-\alpha)F}{RT}\eta\right] - exp\left[\frac{-\alpha F}{RT}\eta\right] \right\} \tag{10.}$$

where i_0 is the exchange current density and α is the charge-transfer coefficient.

5.3 Suppression of Voids and Lithium Dendrite

5.2.1 Definition of Void Suppression Capability (VSC)

To analyze the void evolution mechanism, the VSC of an anode is defined as the product of the applied current (*i*) and full depletion capacity (Q_{max}). The VSC should be a constant for an ideal Li|SSE interface according to the mass-transfer transportation, which is determined by the effective diffusivity (D_{eff}) and the initial interfacial concentration (c_0) of the lithium anode.

Assuming a classical chemical diffusion process driven by the lithium concentration gradient in the anode and the initial interface resistance can be neglected, the depletion times (τ) can be determined by the applied current densities (*i*) according to Sand's equation[95]:

$$\tau^{-\frac{1}{2}} = \frac{2}{\sqrt{\pi \cdot D_{eff}} \cdot c_0 \cdot F} \cdot i \tag{11.}$$

where D_{eff} , c_0 , and F are the effective diffusion coefficient, initial lithium concentration for the anode, and Faraday constant, respectively. We have the full depletion capacity Q_{max},

$$Q_{max} = i \cdot \tau \tag{12.}$$

Defining the void suppression capability: $VSC = i \cdot Q_{max}$, and combining equations (4) and (5),

$$VSC = i^2 \cdot \tau = \frac{\pi \cdot D_{eff} \cdot c_0^2 \cdot F^2}{4} \tag{13.}$$

Since the effective diffusion coefficient and initial lithium concentration for the anode are the intrinsic properties of the anode, the VSC should be a constant for certain lithium metal or alloy anodes. The relative void suppression capability (RVSC) is obtained by defining the VSC of Li metal as 1.

5.2.2 Relationship between the VSC and CCD

For ASSLMB, when the product of the stripped capacity and applied current approaches the VSC, the lithium at the interface will be depleted, inducing void formation.

The critical current density (CCD) is measured as the current density when the cell is short during lithium plating and stripping. According to our principles, a short circuit occurs when the delivered capacity approaches the full depletion capacity using the CCD as the applied current density and a fixed time of t_{CCD}. Thus,

$$VSC = i \cdot Q_{max} > CCD^2 \cdot t_{CCD} \tag{14.}$$

Then, the relationship between the VSC and CCD can be derived as

$$CCD < \sqrt{VSC/t_{CCD}} \tag{15.}$$

The predicted maximum CCD at various t_{CCD} according to the VSC are listed in **Table 5-2**.

Table 5-2 The predicted maximum CCD for Li metal, LiMg, and LiMgLa anodes at a fixed plating/stripping time of 0.5 h based on the published diffusion coefficients.

Anode	**D_{eff} ($cm^2 \cdot s^{-1}$)**	**VSC($s \cdot A^2 \cdot m^{-4}$)**	**Predicted CCD ($mA \cdot cm^{-2}$)**
Li Metal	$(0.8\sim9)\times10^{-11}$	$(0.34\sim3.84)\times10^{5}$	0.44~1.46
LiMg	$(1.3\text{-}7)\times10^{-11}$	$(0.55\sim1.42)\times10^{5}$	0.56~1.29
LiMgLa	3.6×10^{-10}	1.50×10^{6}	2.89
Li Metal	$(0.8\sim9)\times10^{-11}$	$(0.34\sim3.84)\times10^{5}$	0.44~1.46

Current efforts to enhance the interface contact should be useful since it improves c_0. For a critical c_0 (ideal interface), the CCD can be predicted as a function of the capacity, which is presented as the orange line in **Figure 5-2** (data points listed in **Table 5-3**).

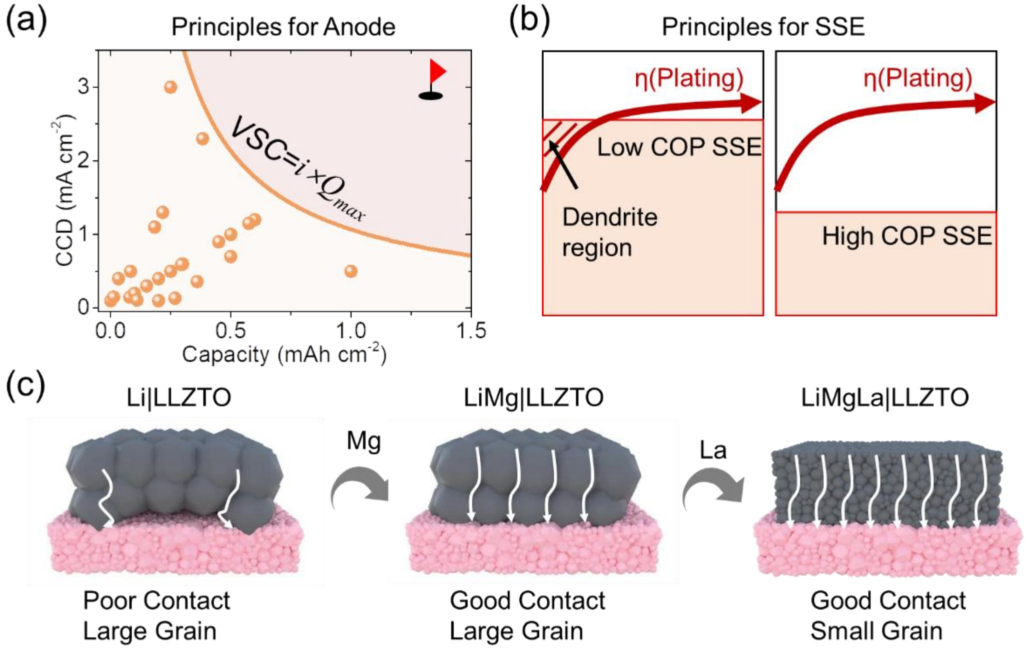

Figure 5-2 Design principles and strategies for high-performance ASSLMBs. (a) The predicted upper limit of CCD (orange line) and reported CCDs (orange scatters) as a function of capacity. The red target on the top right represents a target of high rate and high energy density ASSLMB. (b) Schematic of dendrite formation mechanisms in the SSE with different COPs. The red arrow represents the voltage profile during plating. When the absolute value of voltage is higher than the absolute value of COP, dendrite growth starts. (c) Schematic of the design of high-performance ASSLMB by enhancing the contact and refining the grain size.

The reported CCDs (scatters in **Figure 5-2** a and **Table 5-3**) by SSE modification and interface engineering are chasing the ideal CCD of lithium by c_0 enhancement. The relationship indicates that a high CCD can be achieved by shortening the Li plating/stripping time, which is consistent with the reported results[25]. However, improving the CCD by sacrificing the capacity deviates from the original intention of utilizing the high energy density of ASSLMBs. To simultaneously reach the goal of fast charging and high energy density (star in **Figure 5-2** a), the VSC should be raised by simultaneously improving c_0 at the interface and D_{eff} of the anode.

Table 5-3 Reported critical current densities (CCDs) and corresponding area specific capacity (ASC) for planar garnet-type solid-state electrolytes. The improvement strategies and experimental conditions are included. The 25 ℃ is defined as room temperature.

Composition	Methods	ASC ($mAh\cdot cm^{-2}$)	CCD ($mA\cdot cm^{2}$)	T (℃)	P (MPa)	Ref.
$Li_{6.5}La_3Zr_{1.5}Ta_{0.5}O_{12}$	Microstructure	0.08 0.20 0.30	0.15 0.40 0.60	25	1.4	J. Power Sources 2017, 363, 145–152.
$Li_{6.5}La_3Zr_{1.5}Ta_{0.5}O_{12}$	Roughness	0.1 0.2	0.2 0.4	25	1.4	J. Electrochem. Soc. 2017, 164, A666-A671.
$Li_{6.55}La_3Zr_{1.55}Ta_{0.45}O_{12}$	Relative density	0.36 0.11	0.36 0.11	25	/	Batteries Supercaps 2019, 2, 524–529.
$Li_{6.6}La_3Zr_{1.6}Ta_{0.4}O_{12}$	Acid Etching	1.0 0.2	0.5 0.1	20	0.15	ACS Appl. Energy Mater. 2019, 2, 6720–6731.
$Li_{6.5}La_3Zr_{1.5}Ta_{0.5}O_{12}$	SPS sintering	0.3	0.6	25	1.4	J. Power Sources, 2017, 363, 145-152
$Li_7La_3Zr_2O_{12}$	HIP	0.295	0.591	25	/	Solid State Ionics, 2018, 319, 285-290
$Li_{6.25}Ga_{0.25}La_3Zr_2O_{12}$	Heat treatment	0.45	0.9	60	/	ACS applied materials & interfaces 2018, 11, 1, 898-905.
$Li_7La_3Zr_2O_{12}$	Grain refinement	0.134	0.268	25	/	ACS applied materials & interfaces 2015, 7.3, 2073-2081
$Li_{6.5}La_3Zr_{1.5}Ta_{0.5}O_{12}$	Au/Nb coating	0.083	0.5	25	0.1	Rare Metals 2018, 37, 473-479.
$Li_7La_{2.75}Ca_{0.25}Zr_{1.75}Nb_{0.25}O_{12}$	Mg coating	0.008	0.1	25	/	Angewandte Chemie International Edition 2017, 56, 47, 14942-14947.
$Li_{6.5}La_3Zr_{1.5}Ta_{0.5}O_{12}$	Li_3N coating	0.0125	0.15	25	/	Nano Lett. 2018, 18, 11, 7414–7418
$Li_{6.5}La_3Zr_{1.5}Ta_{0.5}O_{12}$	Cu_3N coating	0.6	1.2	25	/	Energy & Environmental Science 2020, 13, 1, 127-134.
$Li_{6\cdot4}La_3Zr_{1\cdot4}Ta_{0\cdot6}O_{12}$	SnO_2 coating	0.575	1.15	30	/	J. of Power Sources 2019, 420, 15-21.
$Li_{5.9}Al_{0.2}La_3Zr_{1.75}W_{0.25}O_{12}$	Graphite interface	0.15	0.3	25	/	ACS Energy Lett. 3, 2018, 1212-1218

		0.25	0.5	80	/	
$Li_{6.5}La_3Zr_{1.5}Ta_{0.5}O_{12}$	Li-C composite	0.5	1	60	/	Adv. Mater. 2019, 31, 1807243
$Li_{6.28}La_3Zr_2Al_{0.24}O_{12}$	PVDF-PEO	0.033	0.4	25	/	J. of Mater. Chem. A 2018, 6, 42, 21018-21028.
$Li_{6.5}La_3Zr_{1.45}Ta_{0.55}O_{12}$ with Li_3N Filler	ultrafast sintering with Filler	0.383	2.3	25		Acs Energy Lett. 2021, 6, 3753–3760.
$Li_{6.5}La_3Zr_{1.45}Ta_{0.55}O_{12}$	Control group	0.217	1.3		/	
$Li_{6.28}Al_{0.24}La_3Zr_2O_{12}$	Li–Zn alloy anode	0.183	1.1	25	/	Acs Appl Energy Mater. 2020, 3, 9010–9017
$Li_{6.5}La_3Zr_{1.5}Ta_{0.5}O_{12}$	Li_3PO_4	0.4	0.8	25	/	J Mater Chem A. 2019, 7, 14565–14574
$Li_{6.5}La_3Zr_{1.5}Ta_{0.5}O_{12}$	LiMgLa alloy	1.1	2.2	25	/	This Work
$Li_{6.5}La_3Zr_{1.5}Ta_{0.5}O_{12}$	LiMg alloy	0.5 0.25	0.7 3.0	25	/	This Work

The voids at Li|SSE reduce the effective contact area at the interface and partially block lithium paths into the SSE, making the mass-transfer controlled overpotential (η) increase rapidly with the galvanistic lithium stripping time. For the subsequent lithium plating process, the initial overpotential may be larger than the critical overpotential (COP) of an SSE with a low COP (less stable against lithium) due to the formed voids, driving lithium dendrite formation and propagation (shadow area in **Figure 5-2** b left). Increasing the COP can effectively suppress dendrite propagation (**Figure 5-2** b right). It should be noted that even for an ideal dendrite-free electrolyte with a high COP, the high interface overpotential due to the formed void will finally block the charge/discharge process. Hence, the “short-circuit” is only one of the external manifestations of the cell failure, while more attention should be given to the reduction of polarization through increasing the VSC.

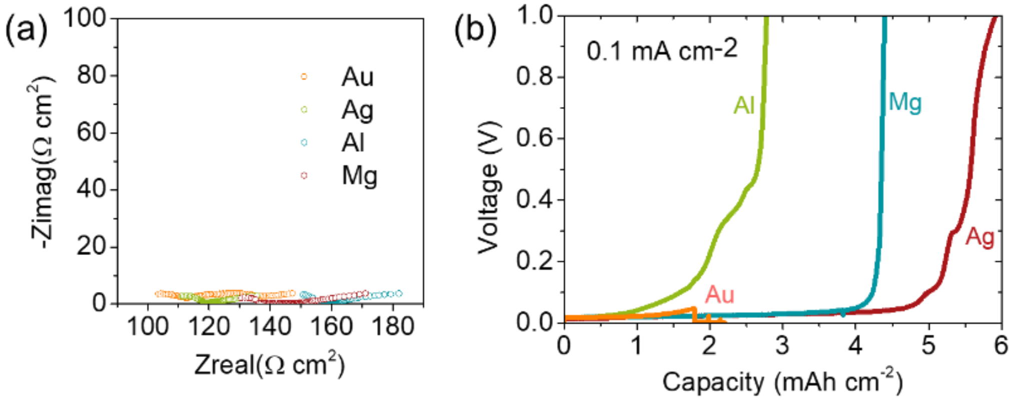

Figure 5-3 (a) Nyquist plots before cycling and (b) voltage profiles at 0.1 mA·cm^{-2} for symmetric cells with Ag-, Mg-, Al-, and Au-doped Li as anodes.

The high lithium concentration at the interface requires intimate contact between the SSE and Li anodes. Adding a small amount of lithiophilic metals, such as Al, Au, Ag and Mg, can effectively enhance the wettability and contact between lithium and SSE (**Figure 5-3**). Since Mg also has a long range of solid-solution phases, MgO can be easily formed at the LLZTO surface to protect the surface from further reduction. Therefore, Mg was selected as an additive in lithium anodes. However, as with other lithiophilic metals, Mg cannot effectively enhance the lithium diffusivity; thus, voids still form dynamically (**Figure 5-2** c middle and **Figure 5-3**). Since the grain boundary has a higher diffusivity than that in the bulk, reducing the grain size should enhance the lithium diffusivity. One way to refine the grain is to add inoculant into molten lithium followed by a rapid solidification. It was reported that Mg-La can form intermetallic compounds, which can serve as the effective nucleus[26] for lithium crystallization (**Figure 5-2** c right). Similar to the solidification process, Mg-La can also maintain the nuclear role during the electrochemical Li plating/stripping process, inheriting the refined grain size. With a decent interface contact and fast lithium diffusion inside the lithium anode, the LiMgLa anodes should achieve a high VSC and enable both high rate and high energy density cells.

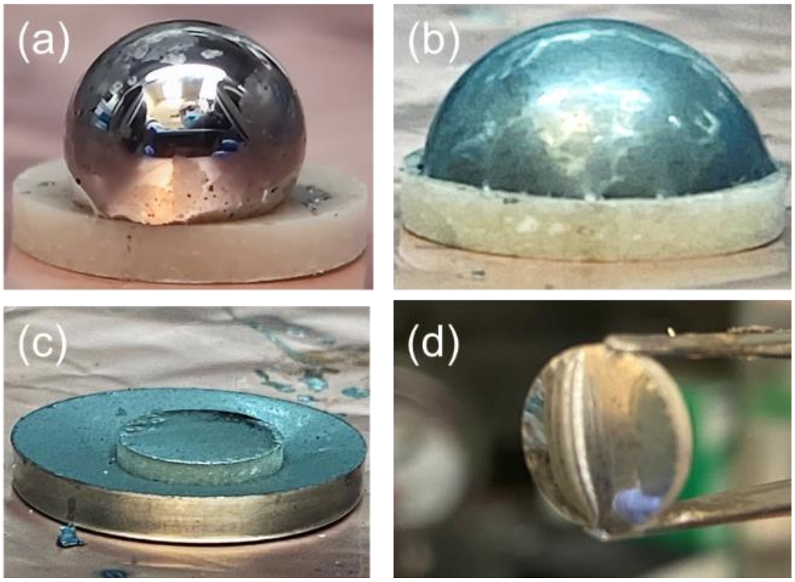

Figure 5-4 Digital pictures of the wettability of (a) molten Li and (b) molten LiMgLa against LLZTO pellets and the assembled LiMgLa|LLZTO|LiMgLa symmetric cells at (c) 350 °C and (d) room temperature.

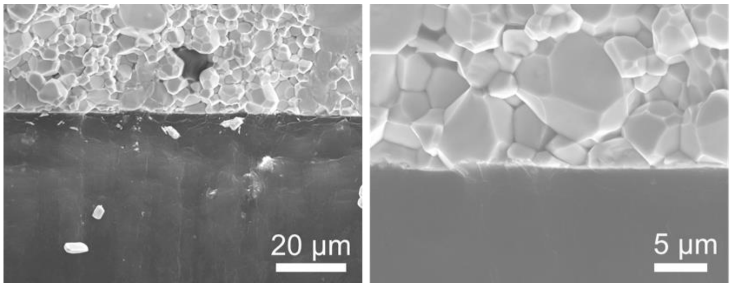

Figure 5-5 Scanning electronic microscope (SEM) images for the cross-section of the LiMgLa|LLZTO interface before cycling at different scales, showing decent contact.

5.4 Void Suppression Capability of the LiMgLa Anodes

Three doped Li anodes, including LiMg ($Li_{97.5}Mg_{2.5}$), LiLa (Li-1%wt La) and LiMgLa ($Li_{97.5}$(Mg-1%wt La$)_{2.5}$), were prepared by adding Mg and/or La into molten Li at 350°C followed by rapid solidification in a glovebox. The interface resistances of these alloy anodes with LLZTO were evaluated with electrochemical impedance spectroscopy (EIS). After subtracting the bulk transport resistance of ~155 $\Omega\cdot cm^2$ in the LLZTO (**Figure 3-8**) from the symmetric cell resistance, the interface resistances of the LiMg, LiLa, and LiMgLa anodes were calculated as 20-35 $\Omega\cdot cm^2$ (**Figure 5-7**). The small initial interface resistances indicate excellent wetting (**Figure 5-4)**, intimate contact, and high c_0 for all of the interfaces (**Figure 5-5** and **Figure 5-6**).

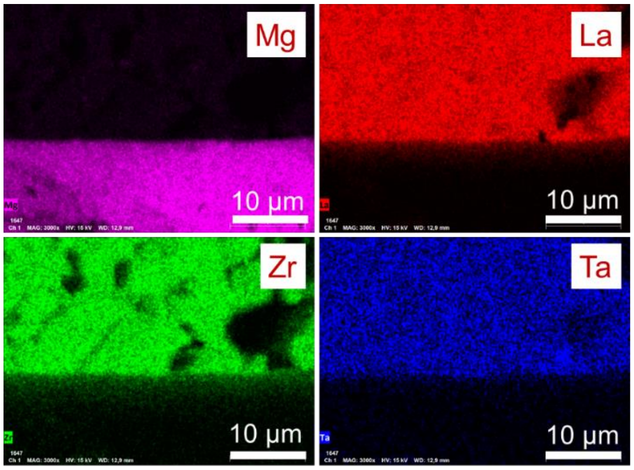

Figure 5-6 Energy dispersive X-ray (EDX) mapping analysis for Mg, La, Zr, and Ta on the cross-section of the LiMgLa|LLZTO interface. The EDX mapping images show distinct domains for the LiMgLa and LLZTO pellets with Mg elements in the electrode and La, Zr, and Ta elements in the LLZTO pellet. The mapping for La confirms that only a small amount of La is doped.

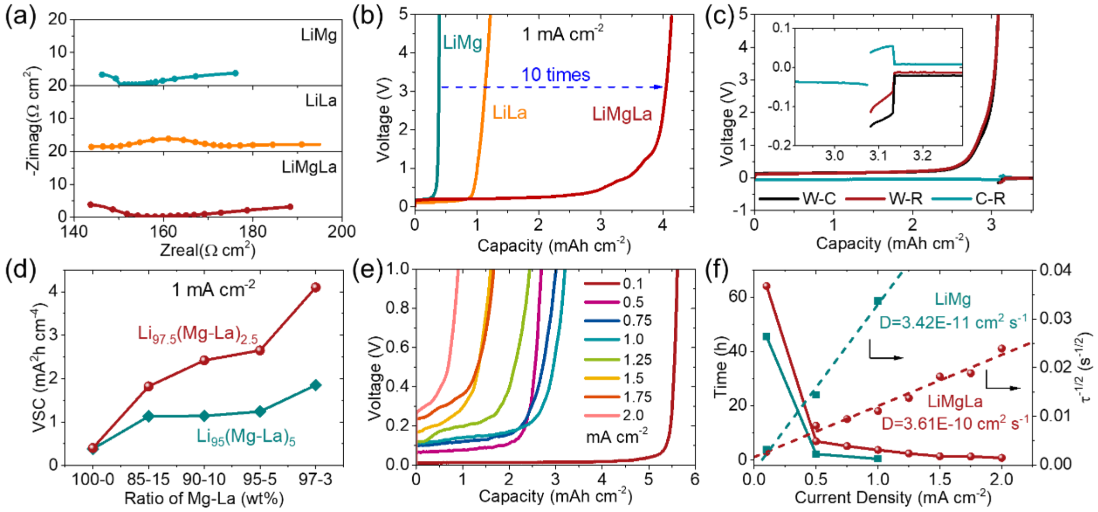

Figure 5-7 VSC of LiMgLa anodes at room temperature. (a) Electrochemical impedance spectra of symmetric cells with LiMgLa, LiLa, and LiMg anodes from 1 MHz to 0.1 Hz using symmetric cells without an external pressure at room temperature. (b) Delivered maximum capacity of LiMgLa LiLa and LiMg anodes during stripping at a current density of 1.0 mA·cm^{-2} with a voltage cut-off of 5.0 V. (c) Voltage profiles for the working-counter (W-C) electrodes, working-reference (W-R) electrodes, and counter-reference (C-R) electrodes measured using a three-electrode cell. The inset figure shows the potential profiles of the subsequent plating process after fully depleted Li stripping. (d) VSC of LiMgLa anodes with different compositions during stripping at a current density of 1.0 mA·cm^{-2}. (e) Potential profiles of LiMgLa anodes during stripping at different current densities. (f) The current density dependency on the Li depletion times and fitted (dotted lines) diffusion coefficients for LiMg and LiMgLa anodes using Sand's equation.

The Li stripping voltage profiles of symmetric cells using LiMg, LiLa and LiMgLa electrodes show flat plateaus with a rapid increase to 5.0 V at the end of the Li stripping at 1.0 mA·cm^{-2} (**Figure 5-7** b). The rapid increase in overpotential is attributed to the detachment of anodes to LLZTO due to void growth. The full stripping capacity of the LiMgLa anode is over 10 times larger than that of the Li anode at a high current of 1.0 mA·cm^{-2}, suggesting a great enhancement of VSC.

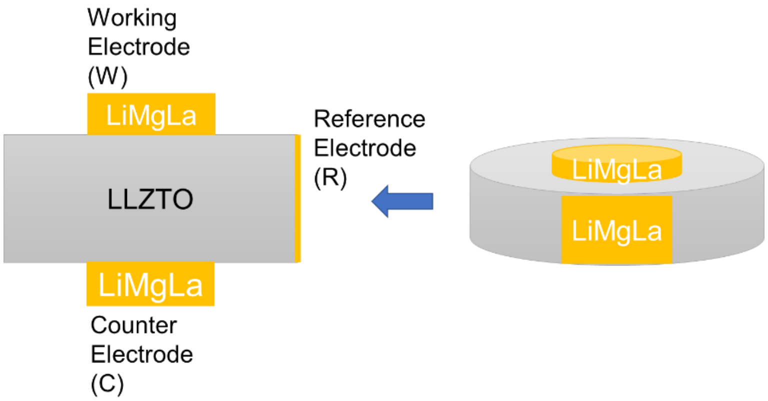

Figure 5-8 Cell schematic for three-electrode cells with LiMgLa electrodes.

Three-electrodes measurement (**Figure 5-8**) demonstrates that under the circumstance of reaching full stripping capacity, even a small amount of plated lithium (0.05 mAh·cm^{-2}) would shorten the circuit (**Figure 5-7** c), indicating the strong correlation between void formation and Li dendrite growth. The potential of the plating side (W-R) gradually decreases while the potential of the stripping side (C-R) gradually increases, suggesting that the dendrite growth from the depleted interface is much faster. The fast short circuit on the depleted interface can also be found at a large current density in the LiMgLa|LLZTO|LiMgLa symmetric cells (**Figure 5-9**).

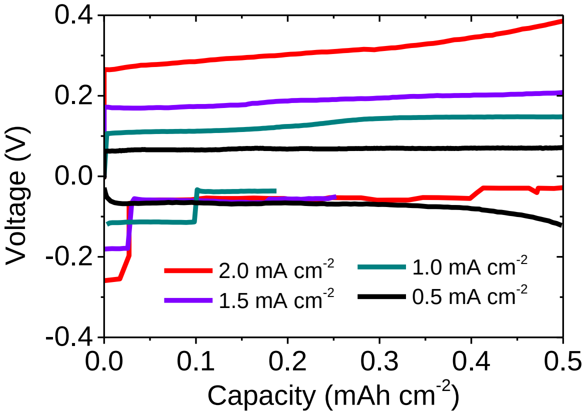

Figure 5-9 The enlarged potential profiles of LiMgLa electrodes at the early stage of stripping and their subsequent plating process at different current densities with a voltage cutoff of 5.0 V. Short circuits are found for the cell for 1.0, 1.5, and 2.0 mA·cm^{-2} within a small capacity of 0.1 mAh·cm^{-2}.

As shown in **Figure 5-7** d and **Figure 5-10**, the VSC of Li anodes increases with Mg/La weight ratios at a fixed total amount of Li-Mg. At a fixed Mg/La weight ratio, all VSCs of the $Li_{97.5}$(Mg-La)$_{2.5}$ anodes are higher than those of Li_{95}(Mg-La)$_5$. The voltage profiles of LiMgLa anodes at different current densities with a cut-off voltage of 5.0 V are displayed in **Figure 5-7** e.

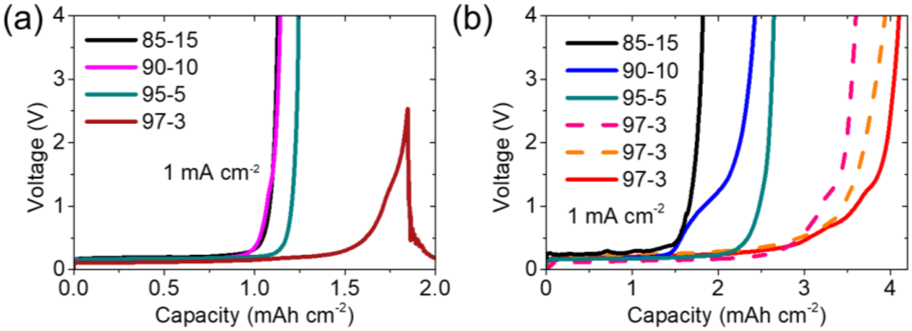

Figure 5-10 Voltage profiles of different composite (a) Li_{95}(MgLa)$_5$ and (b) $Li_{97.5}$(MgLa)$_{2.5}$ electrodes with different Mg-La weight ratios. The dashed lines demonstrate the reproducible performance for LiMgLa anodes.

Table 5-4 The effective diffusion coefficients (D_{eff}), the initial lithium concentration (c_0), and the calculated void suppression capability (VSC) and relative void suppression capability (RVSC, void suppression capability of Li metal set as 1) for Li metal, LiMg, and LiMgLa anodes. The initial surface concentration of LiMg and LiMgLa was set as 0.975 times that of Li metal.

Anode	D_{eff} ($cm^2 \cdot s^{-1}$)	c_0 ($mol \cdot m^{-3}$)	VSC ($s \cdot A^2 \cdot m^{-4}$)	RVSC
Li Metal	5.6×10^{-11}	7.64×10^{4}	2.39×10^{5}	1
LiMg	3.4×10^{-11}	7.45×10^{4}	1.42×10^{5}	0.59
LiMgLa	3.6×10^{-10}	7.45×10^{4}	1.50×10^{6}	6.28

Obviously, the full depletion capacity for the LiMgLa anode is much larger than that of the LiMg (**Figure 5-11**) anodes at a fixed current density. The full depletion times (τ) at different current densities of the LiMg and LiMgLa anodes are shown in **Error! Reference source not found.** f. By fitting plots of $\tau^{-1/2}$ versus current densities (i) using Sand's equation, the fitted D_{eff} of Li for the LiMgLa anode is 3.43×10^{-10} $cm^2 \cdot s^{-1}$, which is one order of magnitude higher than that of the LiMg anode (3.25×10^{-11} $cm^2 \cdot s^{-1}$), confirming the enhancement of Li self-diffusivity and VSC in the LiMgLa anodes. Assuming ideal contact between the anode and SSE, the theoretical VSC of LiMgLa (1.50×10^6 $A^2 \cdot h \cdot m^{-4}$) is 6.28 times higher than that of the Li anode (2.39×10^5 $A^2 \cdot h \cdot m^{-4}$), while the VSC of LiMg (1.42×10^5 $A^2 \cdot h \cdot m^{-4}$) is lower than that of Li (**Table 5-4**).

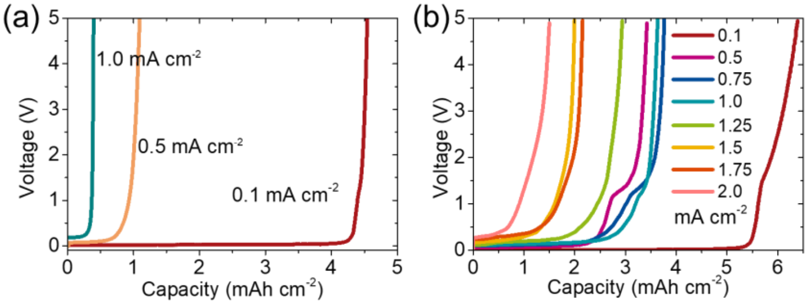

Figure 5-11 Voltage profiles of LiMg|LLZTO|LiMg and LiMgLa|LLZTO|LiMgLa symmetry cells at various current densities with a voltage cutoff of 5 V.

5.5 Mechanism for the high VSC of LiMgLa anodes

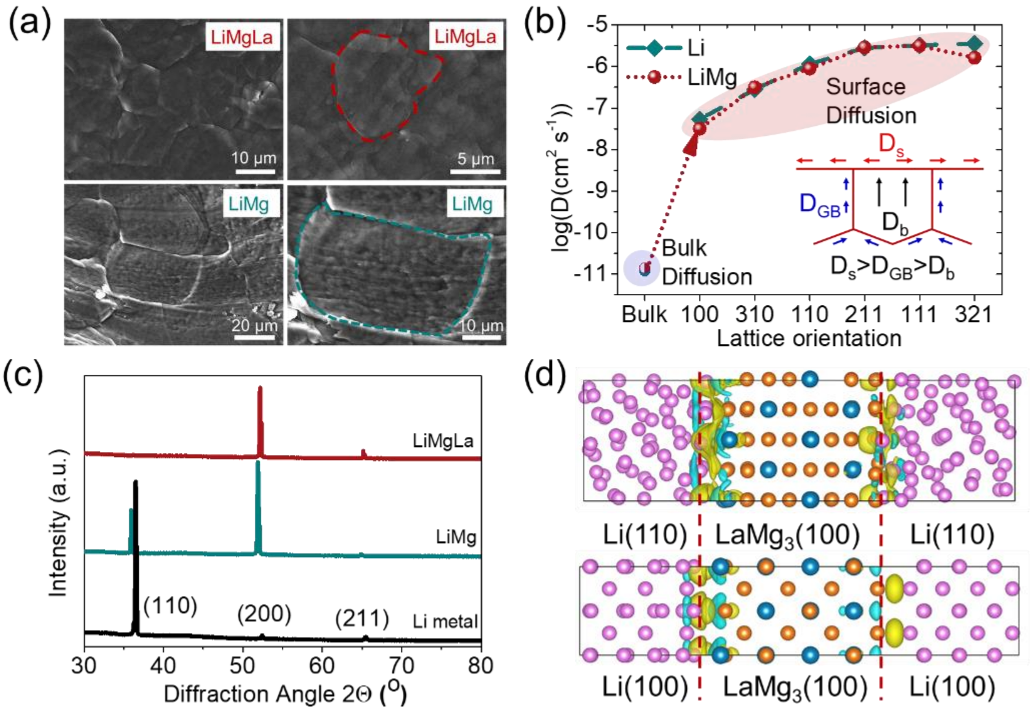

Figure 5-12 Characterization of the LiMgLa anode. (a) SEM showing the grain distributions and sizes of the LiMgLa and LiMg alloys. (b) Molecular dynamics-calculated diffusion coefficients of bulk and differently oriented surfaces for Li metal and LiMg alloy at room temperature. The inset scheme illustrates different diffusion mechanisms. (c) Representative X-ray diffraction data for the Li metal, LiMg, and LiMgLa anodes. (d) Atomic structures and charge distributions of Li(110)|$LaMg_3$(100) and Li(100)|$LaMg_3$(100) interfaces. (Li in pink, Mg in orange,

La in blue and the electron clouds in yellow for charge accumulation and cyan for charge depletion).

The high VSC of LiMgLa anodes is attributed to the refined microstructure with a fast lithium diffusion pathway since Mg-La is an excellent inoculant for metals. Scanning electron microscopy (SEM) was used to characterize the microstructure of the LiMg and LiMgLa anodes. **Figure 5-12** a shows the grain sizes of LiMg and LiMgLa. The grain sizes for the LiMgLa are in the range of 5-10 µm, while those for the LiMg alloy are approximately 40 µm. The smaller grain sizes indicate a larger specific surface and grain boundary area.

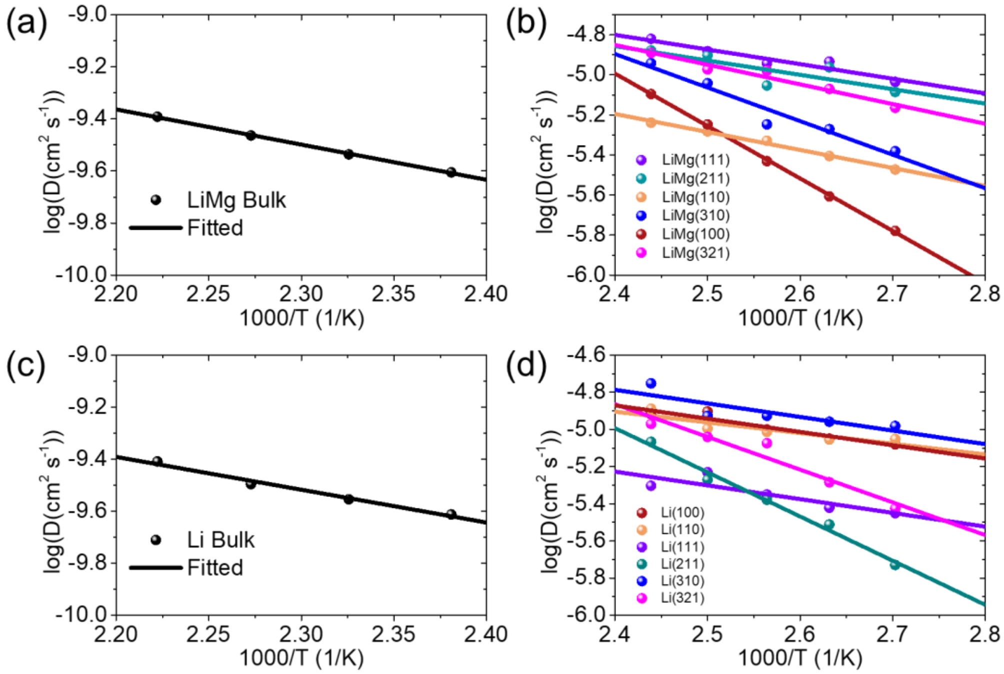

Figure 5-13 Molecular dynamics (MD) calculated diffusion coefficients for (a) LiMg bulk, (b) LiMg surfaces with different orientations, (c) Li bulk, and (d) Li surfaces with different orientations.

The lithium diffusion coefficients of the bulk and surfaces with different orientations for Li and LiMg are calculated via molecular dynamics (**Figure 5-12** b and **Figure 5-13**). LiMg and Li show close diffusion coefficients for both bulk and surface cases because of the low ratio of Mg and the same lattice type. The bulk LiMg shows a similar diffusion coefficient of 1.4×10^{-11} $cm^2 \cdot s^{-1}$ to that of bulk Li (1.1×10^{-11} $cm^2 \cdot s^{-1}$). The calculated diffusion coefficients of LiMg are consistent with the measured D_{eff} (3.42×10^{-11} $cm^2 \cdot s^{-1}$) obtained by fitting the experimental data in **Figure 5-12** f. However, the surface diffusion coefficients of Li and LiMg are over 3 magnitudes higher than those in the bulk (**Figure 5-12** b). LiMgLa anodes have a higher specific surface and grain boundary area than Li and LiMg, enabling faster Li diffusion because of the higher defect concentration at surfaces and grain boundaries.

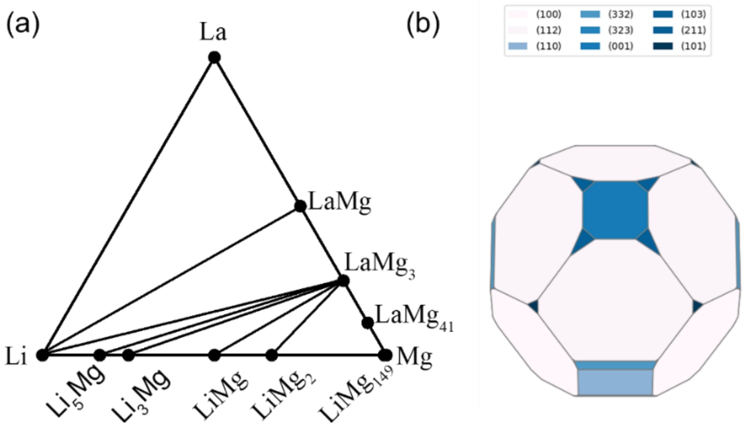

Figure 5-14 (a) Phase diagram from the Materials Project and (b) Wulff shape constructed by calculating the surface energies of different slabs. The picture is generated by using Pymatgen. The Wulff shape indicates that the La_3Mg particle is domain by the (100) surface.

The mechanism by which the Mg-La inoculant refines the Li microstructure was analysed. According to the ternary phase diagram (**Figure 5-14 a**), the added La in

Mg can form $LaMg_3$ compounds, while no intermetallic compound is formed for Li and La. The formed $LaMg_3$ with a higher melting point would act as a crystal nucleus when cooling down the molten LiMgLa alloy. Due to its small size, $LaMg_3$ cannot be indexed in X-ray diffraction (XRD) of the LiMgLa anode (**Figure 5-12** c) due to its weak crystallinity along the (110) orientation. The Wulff shape (**Figure 5-14** b) for $LaMg_3$ has been constructed by calculating the surface energies of different orientations to provide a panorama of the $LaMg_3$ nucleus. The atomic interfaces for $LaMg_3$(100) with Li(110) and Li(100) have been optimized by first-principles calculations based on density functional theory (**Figure 5-12** d). The atomic structures suggest that the $LaMg_3$(100) surface assists in forming amorphous Li along the (110) orientation and well-crystallized Li along the (100) orientation, corresponding to the XRD patterns. The distribution of charge density differences indicates that the interfacial interaction is electrostatic in nature. The characterizations reveal that codoped Mg-La in Li forms $LaMg_3$ intermetallic compounds, serving as excellent nuclei for the crystallization of Li solid solutions. The nucleus refines the grain size and changes the orientation and crystallization of the Li when annealing. The smaller grain size and amorphous Li with a higher defect concentration enhance the diffusion of LiMgLa anodes.

5.6 Void Evolution at the Interface with a High VSC Anode

Figure 5-15 a-b show the SEM cross-sections of the LiMgLa|LLZTO interfaces after Li stripping at currents of 1.0 and 2.0 mA·cm^{-2}, respectively. Voids are clearly observed in both currents, but the void depth of the LiMgLa|LLZTO interface after depletion at 1.0 mA·cm^{-2} is significantly larger than that at 2.0 mA·cm^{-2}, indicating that the smaller current density enables deeper Li stripping since VSC is a constant for the LiMgLa anode. Dendrite can be found inside the LLZTO pellets over the void after the plating process (**Figure 5-15** c).

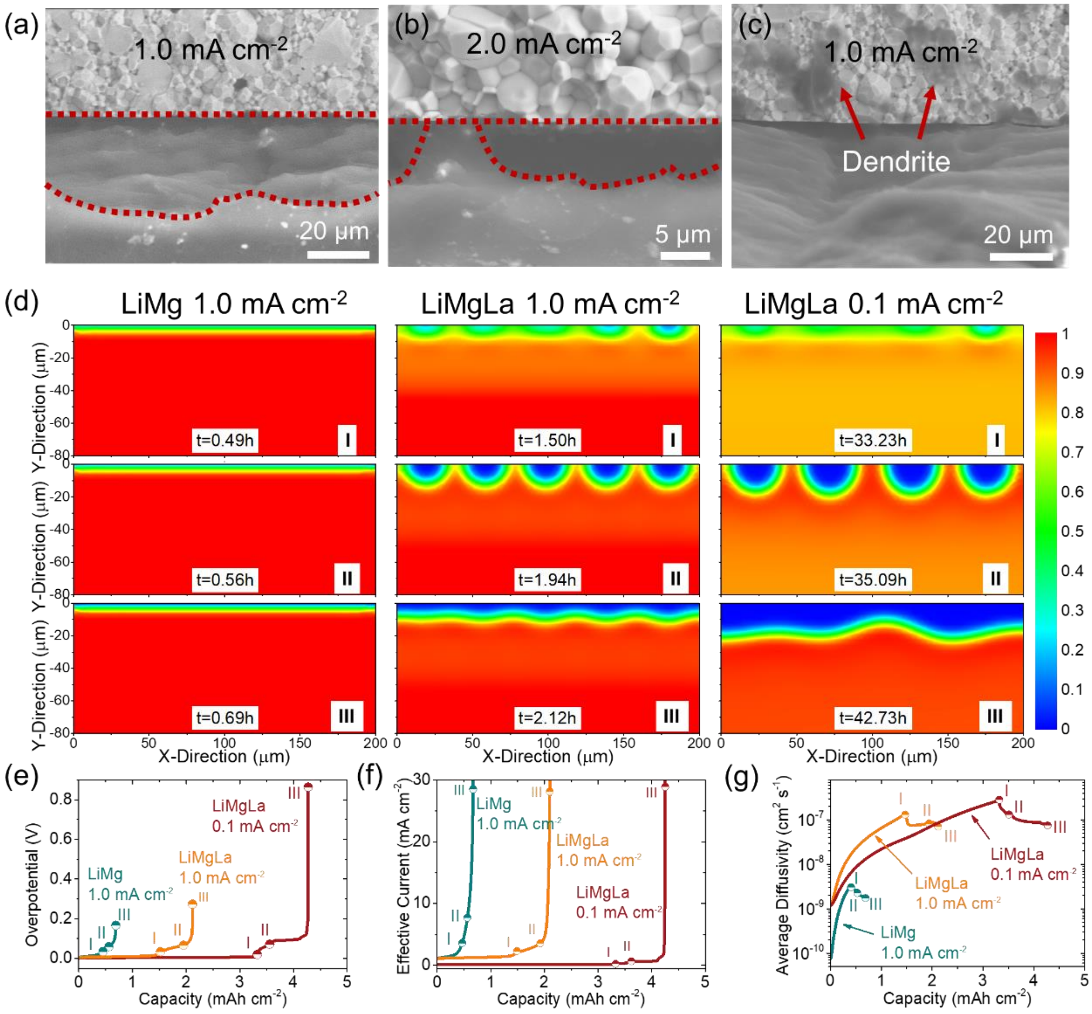

Figure 5-15 Interface evolution of the LiMg and LiMgLa anodes during stripping at different current densities. SEM cross-sections of the LiMgLa|LLZTO interface after full depletion at current densities of (a) 1.0 and (b) 2.0 mA·cm^{-2} and (c) subsequently plated and shorted interface at 1.0 mA·cm^{-2}. The voids are demarcated by the red dashed lines. (d) Snapshots of toid phase at various evolution times and the corresponding (e) Butler-Volmer reaction overpotential, (f) effective current densities showing the current constriction, and (g) average diffusion coefficients for the LiMg anode at 1.0 mA·cm^{-2}, LiMgLa anode at 1.0 mA·cm^{-2}, and LiMgLa anode at 0.1 mA·cm^{-2}. The order parameters (ξ) are listed as ξ=1 stands for lithium and ξ=0 represents the void phase.

The dynamic void formation process at the Li|LLZTO interface during the Li stripping process was simulated using a mesoscale phase-field method (**Figure 5-1** and **Table 5-1**). Snapshots of lithium (ξ=1, red) and void phases (ξ=0, blue) for LiMg and LiMgLa at various times and currents are captured to illustrate the evolution of the anodes (**Figure 5-15** d).

For Stage I, the lithium concentration near the Li|LLZTO interface gradually decreases, resulting in a density-gradient solid-solution reaction without void formation. The delivered capacities for LiMg at 1.0 mA·cm^{-2} are 0.49 mAh·cm^{-2}, LiMgLa at 1.0 ·cm^{-2} are 1.50 mAh·cm^{-2}, and LiMgLa at 0.1 mA·cm^{-2} are 3.32 mAh·cm^{-2}. The corresponding depletion depths are approximately 5, 40, and 80 µm, respectively. Upon further Li tripping, LiMgLa goes to Stage II with the phase transformation process by the formation of vacancies at the interfaces. The void at the LiMgLa|LLZTO interface is formed at 1.94 h with a current of 1.0 mA·cm^{-2} and at 35.09 h with a current of 0.1 mA·cm^{-2}. The voids demonstrate a circular shape. The number of voids at 1.0 mA·cm^{-2} is larger, but the depth of the voids is smaller than those at 0.1 mA·cm^{-2}. Stage III presents detached interfaces with full lithium stripping. For LiMg anodes at 1.0 mA·cm^{-2}, Li was completely depleted at only 0.69 mAh·cm^{-2} without the formation of a void. For the LiMgLa anodes, the anodes detach from the SSEs when the voids merge into one piece. The full depletion capacities of the LiMgLa anodes are 2.12 mAh·cm^{-2} at a current of 1.0 mA cm^{-2} and 4.27 mAh·cm^{-2} at a current of 0.1 mA·cm^{-2}, corresponding to void depths over 10 and 20 µm, respectively. The simulated results are consistent with the SEM cross-sections shown in **Figure 5-15** a-b, suggesting that the simulations capture the key phenomenon of the anodic dissolution process. Interestingly, the anode evolution behavior is counterintuitive, as the void is not forming and evolving along the whole stripping process but only at the late stage of Li stripping (**Supplementary Video**).

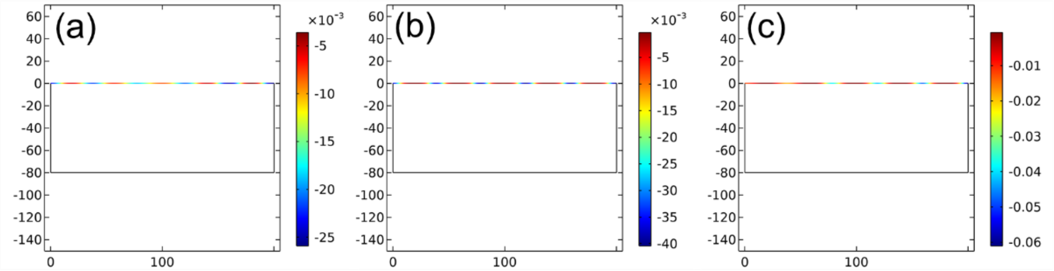

Figure 5-16 Local current density distribution for the LiMgLa|LLZTO interfaces after stripping at 1.0 mA·cm^{-2} for (a) 1.50 h, 1.94 h, and 2.12 h. The inhomogeneous distribution of the current densities during anodic dissolution indicates a current constriction resulting from the morphological evolution of anodes. As the stripping time increases, the current constriction is aggravated.

The simulated overpotential profiles for the Butler-Volmer reaction overpotential in **Figure 5-15** e exhibit the same trends as the experimental voltage profiles (**Figure 5-7** b and e and **Figure 5-11**). The overpotential is flat in Stage I, gradually increases between Stage I and Stage II, and rises rapidly between Stage II and Stage III. These results further confirmed that the abrupt increase in the voltages (**Figure 5-7** b) during Li stripping comes from the mass-transfer overpotential. The profiles of effective current densities (**Figure 5-15** f) and the spatial distribution of the current (**Figure 5-16**) at the interface indicate that the severe contact loss during dissolution, especially after the void formed, induces a high constriction of the current. The constricted current induced a high local overpotential across the SSE, acting as the driving force for SSE reduction and dendrite formation.

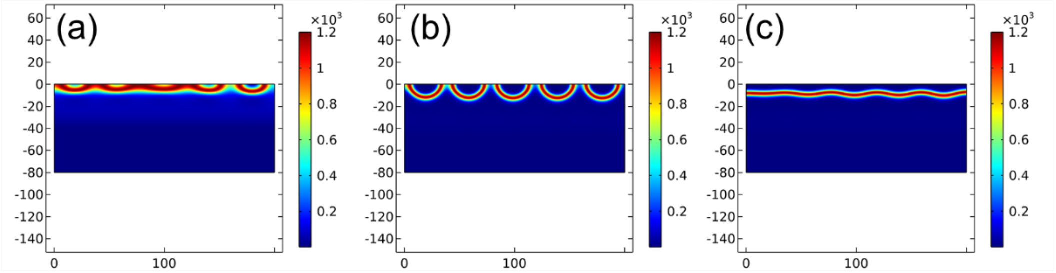

Figure 5-17 Spatial distribution of the normalized diffusion coefficient for the LiMgLa|LLZTO interfaces after stripping at 1.0 mA·cm^{-2} for (a) 1.5, 1.94, and 2.12 h. The distribution of the diffusion coefficient shows a decrease in the diffusion path for Li during anodic dissolution.

The evolution of the average (**Figure 5-15** g) and spatial distribution (**Figure 5-17**) of the diffusion coefficients in the LiMgLa anode demonstrated that the average Li diffusivities of the anodes increased and reached their maximum at Stage I while slightly decreasing during the subsequent stripping process. The reason for the fast phase transformation to form voids is that the high diffusion coefficient at Stage I enables a fast accumulation of vacancies at the interface. Since the delivered capacity

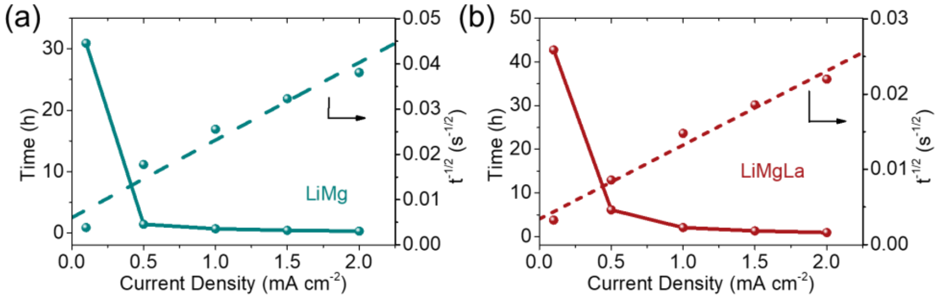

Figure 5-18 The phase-field modeled current density and depletion time dependence, and Sand’s equation fitted (dotted lines) lithium diffusion coefficients for LiMg and LiMgLa anodes.

from Stage I to Stage III is small and void formation leads to unrecoverable morphological instability, lithium utilization within Stage I (~70% of full depletion capacity) is highly recommended for stable cycling, which was confirmed by recent work[13].

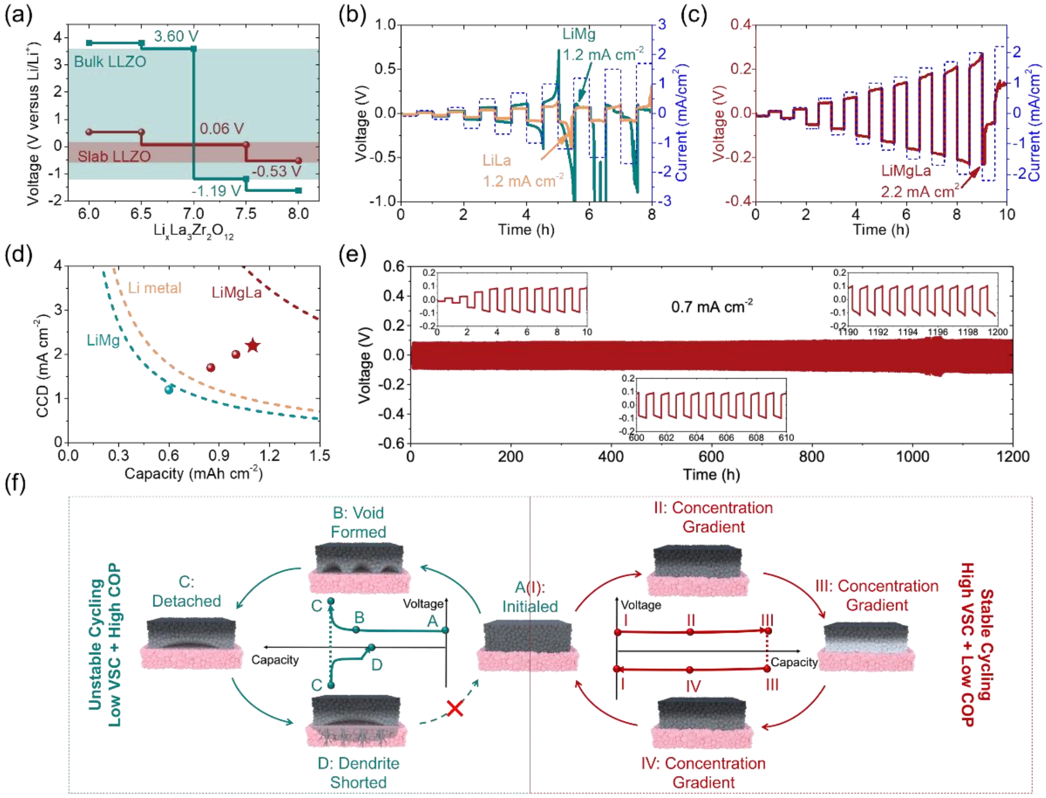

Figure 5-19 Electrochemical characterization of LiMgLa anodes in a solid-state symmetric cell at room temperature. (a) The calculated electrochemical stability window versus Li/Li$^+$ for bulk (cyan region) and slab (red region) $Li_xLa_3Zr_2O_{12}$. CCD measurements for symmetric cells with (b) LiMg, LiLa and (c) LiMgLa as anodes. (d) Comparison of CCD versus capacity for LiMg and LiMgLa anodes. The red dots indicate high reproducibility, as detailed in **Fig. S22**. (e) Cycling performance of LiMgLa|LLZTO|LiMgLa symmetric cells with a current density of 0.7 mA·cm^{-2} for a capacity of 0.35 mAh·cm^{-2}. (f) Interfacial evolution of unstable cycling with a low VSC anode and high COP SSE and stable cycling with a high VSC anode and low COP SSE.

Moreover, the simulated VSC (maximium capacity dependence on the rates) for LiMg and LiMgLa confirms the linear relationship between the current densities and $\tau^{-1/2}$ (**Figure 5-18**). Increasing the diffusion coefficient is an effective strategy to enable fast-charging cells with high capacity by enlarging the duration to reach stage I. Another feasible way is to enhance the utilization of Li by suppressing the phase transformation utilizing elevated pressure.

5.7 Electrochemical Performance with a High VSC Anode

To evaluate the dendrite suppression ability for the LiMg, LiLa, and LiMgLa anodes, the CCDs are obtained by the plating/stripping profiles using a stepwise current density for a fixed 0.5 hour. For both the LiMg and LiLa anodes (**Figure 5-19** b), a steep increase in voltage occurs at a current of 1.2 $mA\cdot cm^{-2}$, while a short circuit then takes place with an abrupt voltage drop. The large polarizations at high current densities are believed to be related to the formation of voids. In sharp contrast, the LiMgLa anode enables a high CCD of 2.2 $mA\cdot cm^{-2}$ with small voltage polarization even before the short circuit (**Figure 5-19** c). The voltages of the plateaus roughly obey Ohm’s law at low current densities, indicating no “soft” short during the process.

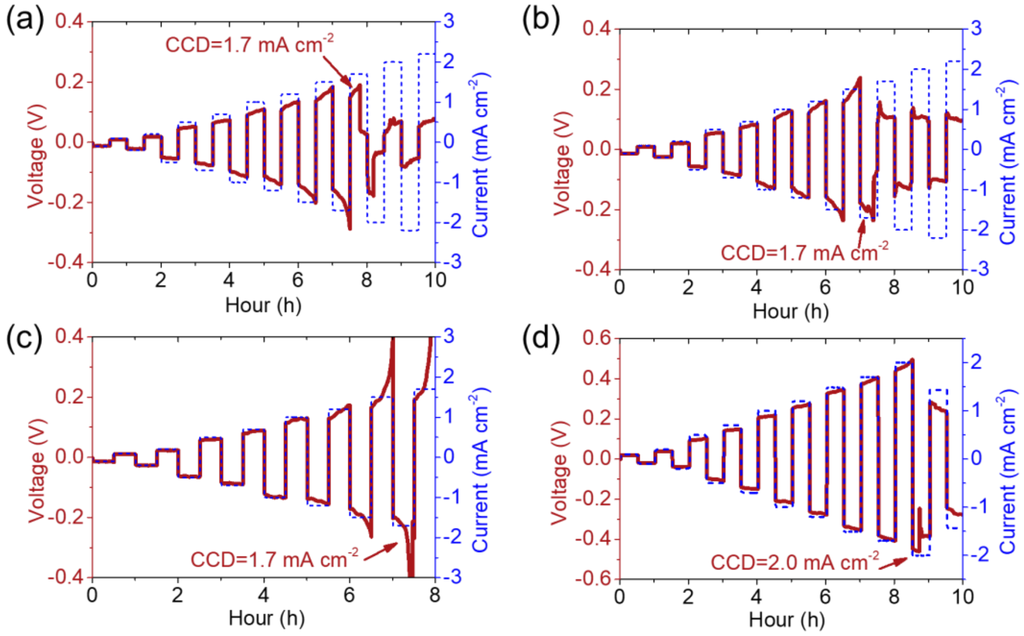

Figure 5-20 CCD measurements for symmetric cells with LiMgLa as anodes showing the high reproducibility.

The LiMgLa anodes have a high CCD of 2.2 mA cm^{-2} due to their high VSC, which simultaneously increases the CCD and deliverable capacity (**Figure 5-19** d and **Figure 5-20**). The LiMgLa anode enables stable cycling at 0.7 mA·cm^{-2} for over 1,200 hours and a high accumulated capacity of >420 mAh·cm^{-2} (**Figure 5-19** e).

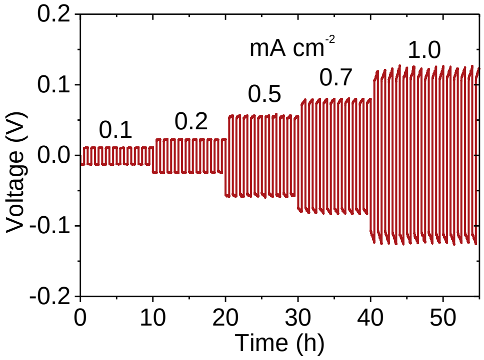

Figure 5-21 Rate performance of symmetric cell with LiMgLa anode at a step-increase current densities of 0.1, 0.2, 0.5, 0.7, and 1.0 mA·cm^{-2} for 10 cycles at each current density.

Moreover, the rate performance of the symmetric cell with the LiMgLa anode is tested at step-increase currents of 0.1, 0.2, 0.5, 0.7, and 1.0 mA·cm^{-2} for 10 cycles at each current density, showing a promising high-rate capability (**Figure 5-21**). The symmetric cell with the LiMgLa anode shows stable and smooth cycling plateaus even at a large current density of 1.0 mA·cm^{-2} at room temperature (**Figure 5-23**).

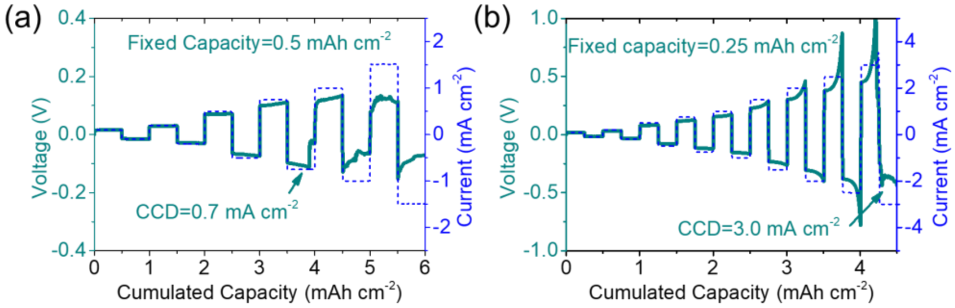

Figure 5-22 Critical current density measurements for $Li_{97.5}Mg_{2.5}$|LLZTO|$Li_{97.5}Mg_{2.5}$ symmetric cells at a fixed capacity of (a) 0.5 mAh·cm^{-2} and (b) 0.25 mAh·cm^{-2}. The measured CCD values are 0.7 mA·cm^{-2} and 3.0 mA·cm^{-2}, indicating that the CCD can be largely improved by reducing the cycling capacity.

The CCD for LiMg anodes can be significantly improved from 0.7 to 3.0 mA·cm^{-2} when reducing the cycling capacity from 0.50 to 0.25 mAh·cm^{-2} (**Figure 5-22**), further confirming the importance of VSC.

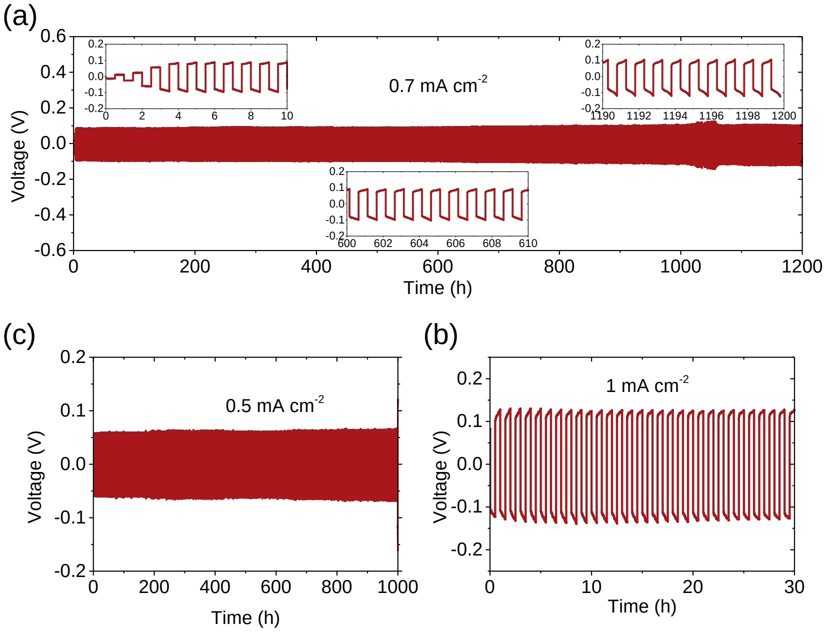

Figure 5-23 Galvanostatic cycling of the LiMgLa|LLZTO|LiMgLa symmetric cell at 0.7 0.5 and 1.0 mA·cm^{-2} at room temperature. The symmetric cell with LiMgLa electrodes enables stable and smooth cycling at a large current density.

The LiMgLa|LLZTO|LiNi$_{0.8}$Mn$_{0.1}$Co$_{0.1}$O$_2$ (NMC811) proof-of-concept cells demonstrate excellent cyclability and rate performance (**Figure 5-24**). The overall characterization of the EIS, CCD, rate performance, and cycling stability at a high current density suggests that the LiMgLa anodes have superior dendrite suppression ability with the LLZTO SSE, resulting from significant improvement of VSC.

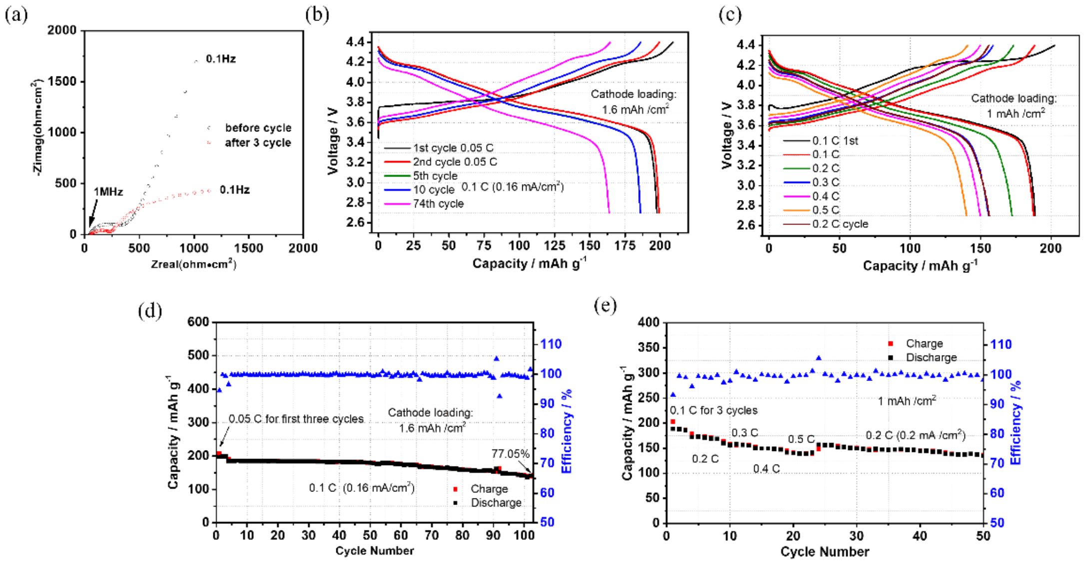

Figure 5-24 Electrochemical performance of the LiMgLa|LLZTO|NMC811 cell. (a) Nyquist spectra of the solid-state cell before and after 3 cycles with a constant current of 0.1 C. The electrochemical charge/discharge curves of the solid cell at (b) 0.1 C and (c) different rates from 0.1 to 0.5 C. (d) Cycling performance of the cell at a current density of 0.1 C. (e) Rate performance of the cell.

Comprehensive characterization, simulation and experiments demonstrated that Li dendrite growth occurs when the Li anode overpotential is higher than COP. The COP mainly depends on the lithiophobicity and mechanical and chemical stability of the SSE, while the Li anode overpotential mainly depends on the VSC, i.e., Li diffusivity and Li concentration. For a Li anode with a low VSC and a low COP, voids will be formed when the delivered capacity exceeds 70% of the maximum capacity (**Figure 5-19** f, left). The voids even detached Li from the SSE surface, leading to a rapid increase in the Li plating overpotential to be larger than COP, which accelerated dendrite formation inside the SSE. The unstable anode and SSE fail the cells rapidly. However, when using an anode with high VSC and an electrolyte with high COP, the Li anode undergoes recoverable concentration depletion with low polarization without void formation, while the high COP of the SSE enables the Li metal cell to achieve a long cycle life even at a high rate with high capacity (**Figure 5-19** f, right). This study provides guidelines for SSE modification, interface engineering and Li anode doping to simultaneously achieve high capacity and long cycle life.

5.8 Conclusion

Void formation at the Li/SSE interface is controlled by the Li diffusivity and Li concentration at the Li/SSE interface. The products of full depletion capacity and stripping current can be used to evaluate the void suppression capability (VSC). The Li anode with a high VSC will not form voids even at a high capacity and current, which reduces the overpotential. To enhance the VSC of Li anodes, Mg and La were codoped into a Li metal anode to achieve a high Li diffusivity by refining the Li grain size. The induced Mg-La enhances the lithium diffusivity by 10 times compared to the LiMg alloy. The LiMgLa anode delivers a high critical capacity of 4.1 mAh·cm^{-2} at 1.0 mA·cm^{-2}, which is 10 times higher than that of the LiMg anode. The high critical rate capacity enables a high CCD of 2.0 mA·cm^{-2} with a capacity of 1.0 mA·cm^{-2} and a high cumulative capacity over 420 mAh·cm^{-2}. The evolution of the anode during anodic dissolution is revealed by the phase-field model, in which the anode proceeds in three stages: solid-solution, phase transformation, and detachment. The higher diffusion coefficient of LiMgLa extends the solid solution and suppresses void formation. The LiMgLa anode provides a chemical strategy to simultaneously improve the fast-charge and high-capacity requirements to match the requirement for ASSLMBs.

Chapter 6 Triple-Phase Design for Highly Reversible Sulfur Cathode in All-Solid-State Lithium-Sulfur Battery

6.1 Introduction

Sulfur cathode is promising to be used in Li-metal batteries for practical application due to its high capacity and low cost. However, the sluggish reaction kinetics of S/Li_2S and polysulfide shuttle in lithium-metal battery (LMB) using organic liquid electrolyte (LE) decrease the utilization of sulfur active materials. Using catalysts can promote the reversible reaction of polysulfide in LMB, thus extending the cycling life of sulfur cathode. To ensure a high polysulfide reversible reaction in LMB, the polysulfide adsorption ability and catalytic activity of the catalyst has to be balanced. The strong adsorption of the polysulfide will lead to the catalyst passivation, while, a poor adsorption can not effectively ameliorate the polysulfide shuttle[96]. However, the formation and dissolution of polysulfide in LE still can not be fully suppressed, which affects the long cycle life of sulfur cathode in LMB. Replacing organic liquid electrolyte to solid-state electrolyte (SSE) can prevent the formation of polysulfide and eliminate the polysulfide shuttle effect. However, the slow reaction kinetics of S/Li_2S in all-solid-state lithium battery (SSLB) is more severe than that in LMB. In LMB, the S/Li_2S is surrounded by LE, the Li^+ transfer between LE and S/Li_2S is not the determining factor influencing the reaction kinetics of S/Li_2S. While, in ASSLB, the limited interfacial contact at electronic additive/SSE/sulfur triple-phase boundaries restricts the utilization of sulfur active material. Improving the Li^+ transfer through coating SSE on sulfur, or enhancing the e^- conduction using electronic conductive carbon as sulfur host can enhance S/Li_2S redox reaction due to the improved triple-phase contacts in these modified sulfur composite cathode. However, the preparation procedures for these modified sulfur cathodes are time-consuming. Besides, the low active sulfur content in the S@C composite will decrease the cell-level energy density because the large amount of electronic conductive carbon host can not provide capacity to the battery. Therefore, sulfur host that can provide extra capacity was introduced into the sulfur composite[22,23,97]. Among these active sulfur hosts, FeS_2 with high electronic/ionic conductivity has been demonstrated to mediate the sulfur redox reaction in SSLB[22]. During lithiation/delithiation process at cut-off voltage of 1.0~3.0V, the following reactions occur in FeS_2, and reaction (5) is the rate determining procedure for the electrochemical reversibility of FeS_2.

$FeS_2 + 2Li^+ + 2e^- \rightarrow Li_2FeS_2$ (1)

$Li_2FeS_2 + 2Li^+ + 2e^- \rightarrow 2Li_2S + Fe$ (2)

$2Li_2S + Fe \leftrightarrow Li_2FeS_2 + 2Li^+ + 2e^-$ (3)

$Li_2FeS_2 \leftrightarrow Li_{2-x}FeS_2 + xLi^+ + xe^-$ (4)

$Li_{2-x}FeS_2 \leftrightarrow FeS_y + (2-y)\ S + (2-x)\ Li^+ + (2-x)\ e^-$ (5)

Introducing transition metal into FeS_2 can improve the reaction kinetics of reaction (5).[98] However, the volume expansion of FeS_2 after fully lithiation remains unsolved, which will lead to the structure collapse of FeS_2@S composite during long cycles, thus resulting in rapid capacity decay of FeS_2@S composite when the capacity is fully utilized[2]. Therefore, to stabilize the structure of FeS_2@S composite in SSLB, the cell cut-off voltage was restricted at 1.5~2.8V[23], where reaction (1) with small volume change and high reversibility proceeds in FeS_2. However, the delivered capacity of FeS_2@S composite was reduced when restricting the cut-off voltage to 1.5~2.8V. How to maintain a good cycling stability with a high capacity utilization of FeS_2@S composite at high cathode loading remains challenging.

Increasing the Li^+/e^- transfer inside the bulk material or at the phase boundary of different components can enhance the reaction kinetics of the composite cathode in ASSLB. Therefore, to fully utilize the capacity of FeS_2@S composite, a bridge with fast Li^+ diffusivity should be *in-situ* formed at FeS_2-S-Li_6PS_5Cl triple phase boundary during the initial few delithiation/lithiation process to ensure high Li^+ exchange in FeS_2@S-Li_6PS_5Cl-C composite cathode during the following cycles. We have demonstrated that introduction of LiI into Li_2S can significantly improve the reversibility of S/Li_2S redox reaction due to the reduced Li-S bond and improved ionic conductivity of Li_2S@LiI composite[99]. Besides, Wagemaker's group[100] also demonstrated that the LiI coating on Li_2S can improve the Li^+ diffusivity over Li_6PS_5Cl/Li_2S interface, where LiI acts as a Li^+ transfer bridge between Li_6PS_5Cl and Li_2S. Therefore, to improve the reaction kinetics of FeS_2@S, transition metal iodide should be chosen as dopant, because transition metal iodide can *in-situ* transfer to LiI and transition metal when FeS_2@S was fully lithiated, where transition metal can improve the reaction kinetics of FeS_2, and LiI acts as a bridge at FeS_2-S-Li_6PS_5Cl

phase boundary in FeS_2@S-Li_6PS_5Cl composite cathode to improve the redox kinetics of S/Li_2S, thus enhancing the electrochemical performance. To demonstrate this assumption, CuI was chosen as dopant in this work. After the first few cycles, FeS_2@S@CuI composite *in-situ* transfers to FeS_2@S@Cu@LiI, the *in-situ* built fast e^-/Li^+ transfer in FeS_2@S composite enables FeS_2@S composite to cycle even without addition of Li_6PS_5Cl electrolyte and electronic conductive carbon into the cathode. The impedance spectra show that at the third fully lithiated state (discharge to 1.0V), the interfacial resistance in FeS_2@S@CuI composite was decreased, because of the enhanced Li^+ exchange at FeS_2-S-Li_6PS_5Cl triple-phase boundary. While for FeS_2@S composite without CuI doping, the impedance increases continuously during discharge/charge processes due to the volume expansion of FeS_2@S when fully lithiation, which leads to the contact loss at FeS_2-S-Li_6PS_5Cl triple phase boundary and structure collapse of the composite cathode. Besides, the XRD pattern shows that CuI can promote the amorphization of S in FeS_2@S composite, which can further decrease the reaction barriers of S/Li_2S redox reaction. Benefited from these merits, the FeS_2@S@CuI composite delivers a high reversible capacity of 4.0 mAh cm^{-2} with a high initial Coulombic Efficiency of 94.6% at current density of 0.5 mA cm^{-2} under room temperature. After five cycles, the capacity utilization of FeS_2@S@CuI composite reaches to 96.5%. Even at low temperature, the FeS_2@S@CuI composite cathodes deliver specific capacity of 499.9 mAh g^{-1} (44.4% of capacity utilization) at -20^oC, and 374.4 mAh g^{-1} (33.3% of capacity utilization) at -30^oC. Furthermore, the FeS_2@S@CuI composite cathode with high areal capacity of 4.0 mAh cm^{-2} also shows good cycling stability with capacity retention of 88.8% after 145 cycles. Such a high capacity utilization and good cycling stability at high cathode loading has never been reported in ASSLB.

6.2 Experimental

6.2.1 Synthesis of FeS2@S@CuI and FeS2@S composite

FeS_2@S@CuI was prepared by ball-milling procedures. Typically, FeS_2 and CuI with mole ratio of 9: 1 was ball-milled at 500 rpm for 12h. Then, the obtained FeS_2@CuI and S with weight ratio of 1: 1 was further ball-milled at 500 rpm for 12.0 hours to obtain the final FeS_2@S@CuI composite. FeS_2@S was prepared by the same ball-milling procedures without adding CuI.

The theoretical capacity of S is 1673 mAh g^{-1}, and FeS_2 is 894 mAh g^{-1}. Therefore, the theoretical capacity of FeS_2@S composite is (1673+894)/2=1283.5 mAh g^{-1}. The weight ratio of FeS_2 in the FeS_2@S@CuI composite was 42.5%, and the weight ratio of S in the FeS_2@S@CuI composite was 50%. Therefore, the theoretical capacity of FeS_2@S@CuI composite is 1673×0.5+894×0.425=1216.45 mAh g^{-1} based on the weight of FeS_2@S, and 1216.45×0.925=1125.2 mAh g^{-1} based on the weight of FeS_2@S@CuI.

6.2.2 Electrochemical Measurements

Before assembling all-solid-state battery, FeS_2@S@CuI and C with weight ratio of 5: 1 was ball-milled, then the obtained FeS_2@S@CuI-C was hand mixed with Li_6PS_5Cl

with weight ratio of 6: 4 to form FeS_2@S@CuI-C-Li_6PS_5Cl composite cathode. All-solid-state battery was assembled as following. Firstly, 100 mg of Li_6PS_5Cl electrolyte was pressed at 2 ton to form a pellet with diameter of 10 mm. Then, the composite cathode material was spread on one side of Li_6PS_5Cl electrolyte and pressed at 4 ton. After that, LiIn anode was attached on the other side of Li_6PS_5Cl electrolyte.

The electrochemical performances of the fabricated all-solid-state lithium battery were evaluated on an Arbin BT2000 workstation (Arbin Instruments, TX, USA). To investigate impact of CuI doping on the redox kinetics of FeS_2@S, cyclic voltammetry (CV) was measured at a scan rate of 0.2 mV s^{-1}. Electrochemical impedance spectroscopy (EIS) analyses were conducted on Gamry instrument at frequencies from 1 MHz to 0.1 Hz with the amplitude of 15 mV under argon.

6.3 High e-/Li+ Exchange across the FeS2@S@CuI

FeS_2@S@CuI composite was prepared by ball-milling procedures, where the mole ratio of FeS_2 and CuI was 9: 1, and the weight ratio of FeS_2@CuI: S was 50: 50. As shown in **Figure 6-1** a, after ball-milling, the diffraction peaks for sulfur disappeared in FeS_2@S@CuI composite. While the sulfur diffraction peaks still maintain in FeS_2@S composite without CuI, implying the introduction of CuI additive can promote the amorphization of S in FeS_2@S composite, which will decrease the reaction barriers of S/Li_2S redox reaction.

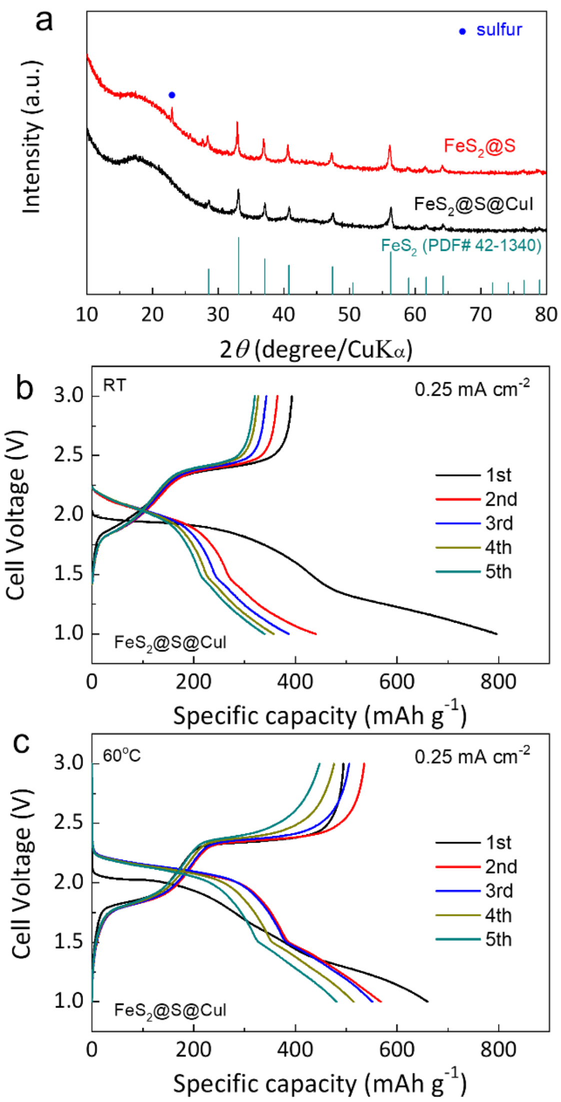

Figure 6-1 (a) XRD patterns of FeS_2@S and FeS_2@S@CuI composite. Galvanostatic discharge/charge profile of FeS_2@S@CuI composite at (b) room temperature and (c) temperature of 60°C without addition of Li_6PS_5Cl electrolyte and conductive carbon in the cathode layer.

To demonstrate the *in-situ* formed fast e^-/Li^+ transfer in FeS_2@S composite was achieved after CuI doping, all-solid-state battery using FeS_2@S@CuI cathode (without electrolyte and conductive carbon, cathode loading: 1.3 mg cm^{-2}) were assembled. As shown in **Figure 6-1**, FeS_2@S@CuI cathode delivers initial reversible capacity of 393.4 mAh g^{-1} at room temperature (**Figure 6-1** b, 35% of capacity utilization), and 535.4 mAh g^{-1} at temperature of 60°C at the second cycle (**Figure 6-1** c, 47.6% of capacity utilization) even without adding additional Li_6PS_5Cl electrolyte and electronic conductive carbon into the cathode, implying the high e^-/Li^+ exchange in the *in-situ* formed FeS_2@S@Cu@LiI composite after the first few lithiation/delithiation processes.

6.4 Enhanced Kinetic in the FeS2@S@CuI Composite Cathode

To further improve the capacity utilization of FeS_2@S@CuI, Li_6PS_5Cl solid electrolyte and electronic conductive carbon additive was further introduced forming FeS_2@S@CuI-Li_6PS_5Cl-C composite cathode. Then, the electrochemical performance of FeS_2@S@CuI-Li_6PS_5Cl-C composite cathode with areal capacity of 4 mAh cm^{-2} was evaluated using LiIn alloy anode. As shown in **Figure 6-2** b, for FeS_2@S@CuI composite cathode, the first discharge plateau that corresponds to the lithiation of S to Li_2S increased to higher potential after the initial cycle, and then the overpotential for S/Li_2S redox reaction maintains almost constant in the following cycles. In sharp contrast, the FeS_2@S composite cathode without CuI additive shows continuously increased S/Li_2S redox overpotential (**Figure 6-2** a), proving the introduction of CuI can significantly improve the reaction kinetics of S/Li_2S after the initial lithiation of CuI to Cu@LiI composite.

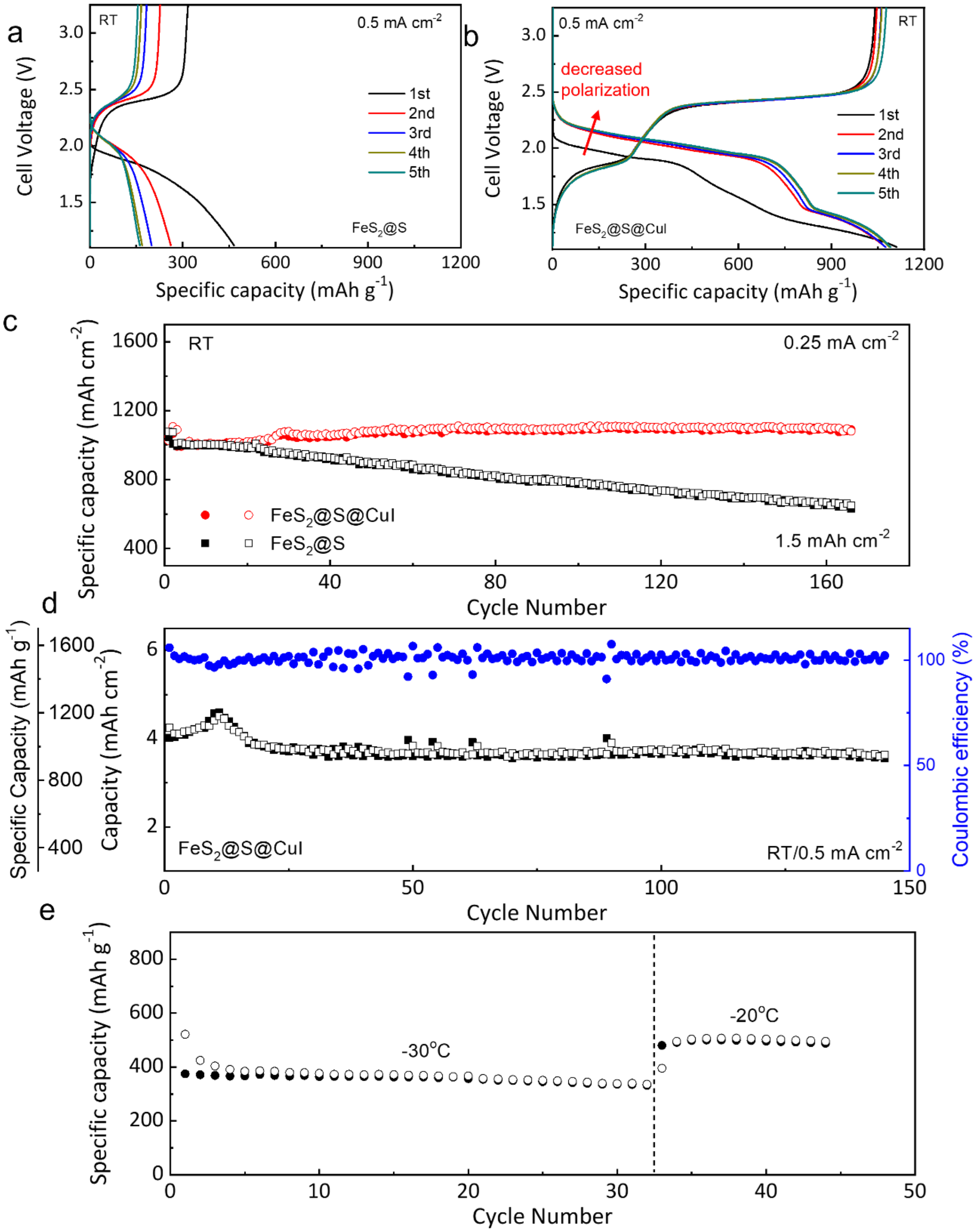

Figure 6-2 Galvanostatic discharge/charge profile of (a) FeS_2@S and (b) FeS_2@S@CuI composite cathode at room temperature. (c) Cyclic performance of FeS_2@S composite cathode with and without CuI additive under areal capacity of 1.5 mAh cm^{-2}. (d) Cyclic performance of FeS_2@S@CuI composite cathode with areal capacity of 4.0 mAh cm^{-2} at room temperature. (e) Cyclic performance of FeS_2@S@CuI composite cathode at low temperature of -30°C and -20°C.

The improved S/Li_2S redox kinetics leads to the FeS_2@S@CuI composite cathode delivers a high reversible capacity of 4.0 mAh cm^{-2} with a high initial Coulombic efficiency of 94.6% at current density of 0.5 mA cm^{-2} under room temperature (**Figure 6-2** b). Besides, after five cycles, the FeS_2@S@CuI composite cathode shows a high reversible capacity of 1086.1 mAh g^{-1}, corresponding to capacity utilization of 96.5% (**Figure 6-2**b). In sharp contrast, the reversible capacity of FeS_2@S composite cathode decays to 162.2 mAh g^{-1}, corresponding to capacity utilization of 12.6% at the fifth cycle. Such a modified FeS_2@S@CuI composite cathode with areal capacity of 1.5 mAh cm^{-2} can stable for >167 cycles at current density of 0.25 mA cm^{-2} under room temperature (**Figure 6-2** c). While, the FeS_2@S composite cathode shows rapid capacity decay at the same cathode loading (Figure 2c). When further increasing the areal capacity to 4 mAh cm^{-2}, the FeS_2@S@CuI composite cathode still shows excellent cyclic performance with capacity retention of 88.8% after 145 cycles (**Figure 6-2** d). Even at low temperature, the FeS_2@S@CuI composite cathode can deliver specific capacity of 499.9 mAh g^{-1} at -20^{o}C, and 374.4 mAh g^{-1} at -30^{o}C (**Figure 6-2** e). Such a high capacity utilization (44.4% of capacity utilization at -20^{o}C, and 33.3% of capacity utilization at -30^{o}C) at low temperature has never been reported in SSLBs.

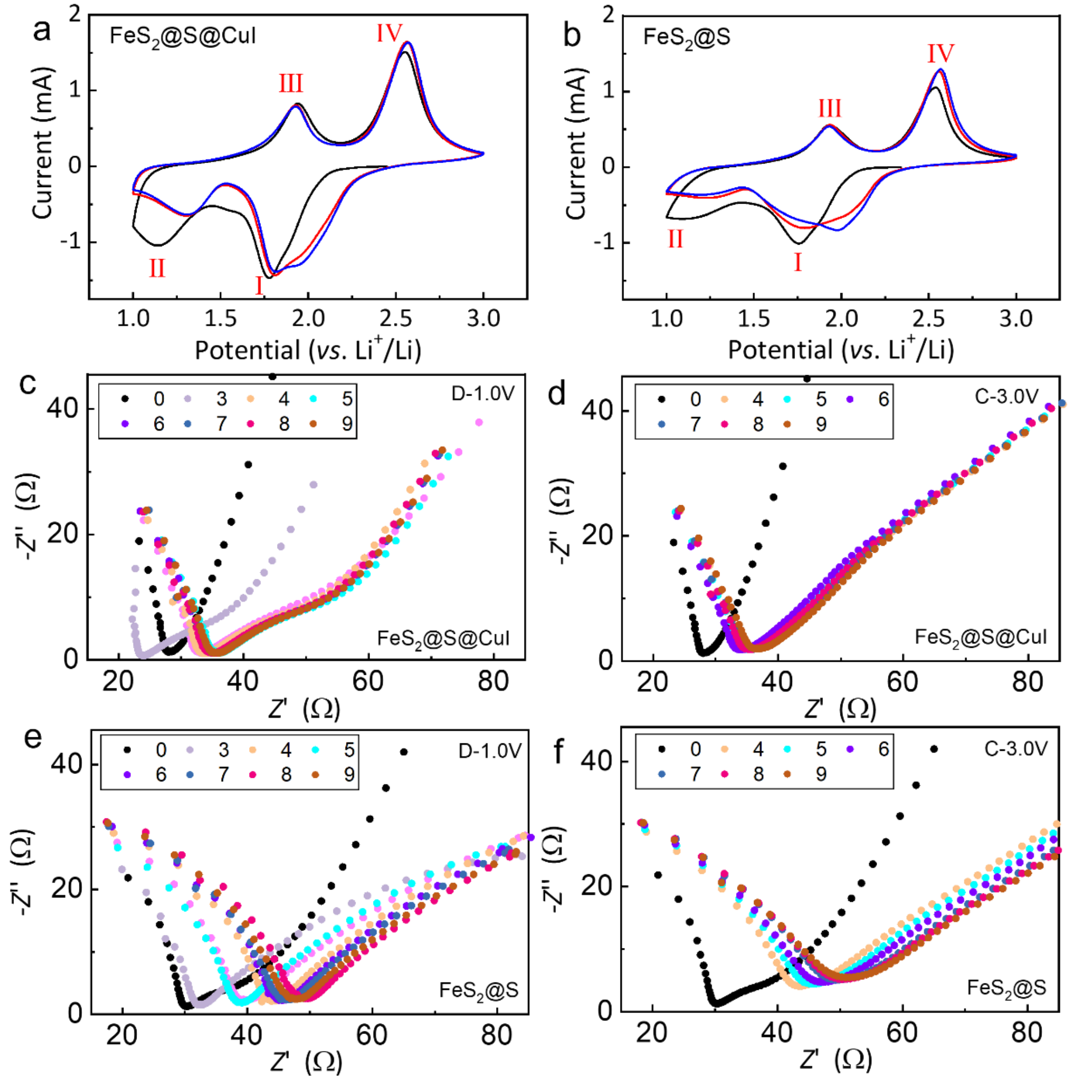

Figure 6-3 CV curves of (a) FeS_2@S@CuI and (b) FeS_2@S composite cathode. EIS spectra of FeS_2@S@CuI composite cathode at (c) fully discharged state and (d) fully charged state. EIS spectra of FeS_2@S composite cathode at (e) fully discharged state and (f) fully charged state.

CV and operando EIS were collected to explore the catalytic effect of CuI on the redox kinetics of FeS_2@S. As shown in **Figure 6-3** a, during the first anodic scan of FeS_2@S@CuI composite, the reduction peak I belongs to the lithiation of S to Li_2S, and the reduction peak II belongs to the lithiation of FeS_2 to Li_2S and Fe. Compared with the reduction peaks in FeS_2@S@CuI composite cathode, the reduction peaks I in FeS_2@S moves to more negative value, and the reduction peak II were almost vanished (**Figure 6-3** b), implying the formation of Li_2S (reduction peaks I) affects the further lithiation of FeS_2 without CuI additive. In the first cathodic scan, the oxidation peak III belongs to the reaction (3) $2Li_2S + Fe \rightarrow Li_2FeS_2 + 2Li^+ + 2e^-$ and oxidation peak IV attributes to reaction (4) $Li_2FeS_2 \rightarrow Li_{2-x}FeS_2 + xLi^+ + xe^-$ and (5) $Li_{2-x}FeS_2 \rightarrow FeS_y + (2-y)\ S + (2-x)\ Li^+ + (2-x)\ e^-$, and the oxidation of Li_2S back to S. Then, from the second cycle onward, the FeS_2@S@CuI composite cathode shows excellent redox reversibility compared with FeS_2@S composite cathode. The improved reaction kinetics in FeS_2@S@CuI composite cathode after the first few cycles can also be proved by the reduced impedance of FeS_2@S@CuI composite cathode at the third fully discharged state (D-1.0V, **Figure 6-3** c). Then, from the fourth cycle onward, the interfacial resistance at fully discharged state (D-1.0V, Figure 3c), and the impedance at fully charged state (C-3.0V, **Figure 6-3** d) remains almost constant, proving the highly reversible redox reaction proceeds in FeS_2@S with CuI additive, which is beneficial for maintaining the structure integrity of FeS_2@S@CuI composite cathode during cycles. In sharp contrast, for FeS_2@S without CuI additive, the impedance continuously increases during discharge/charge process (**Figure 6-3** e-f), proving the irreversible redox reaction and structure collapse of the FeS_2@S composite cathode after lithiation/delithiation processes.

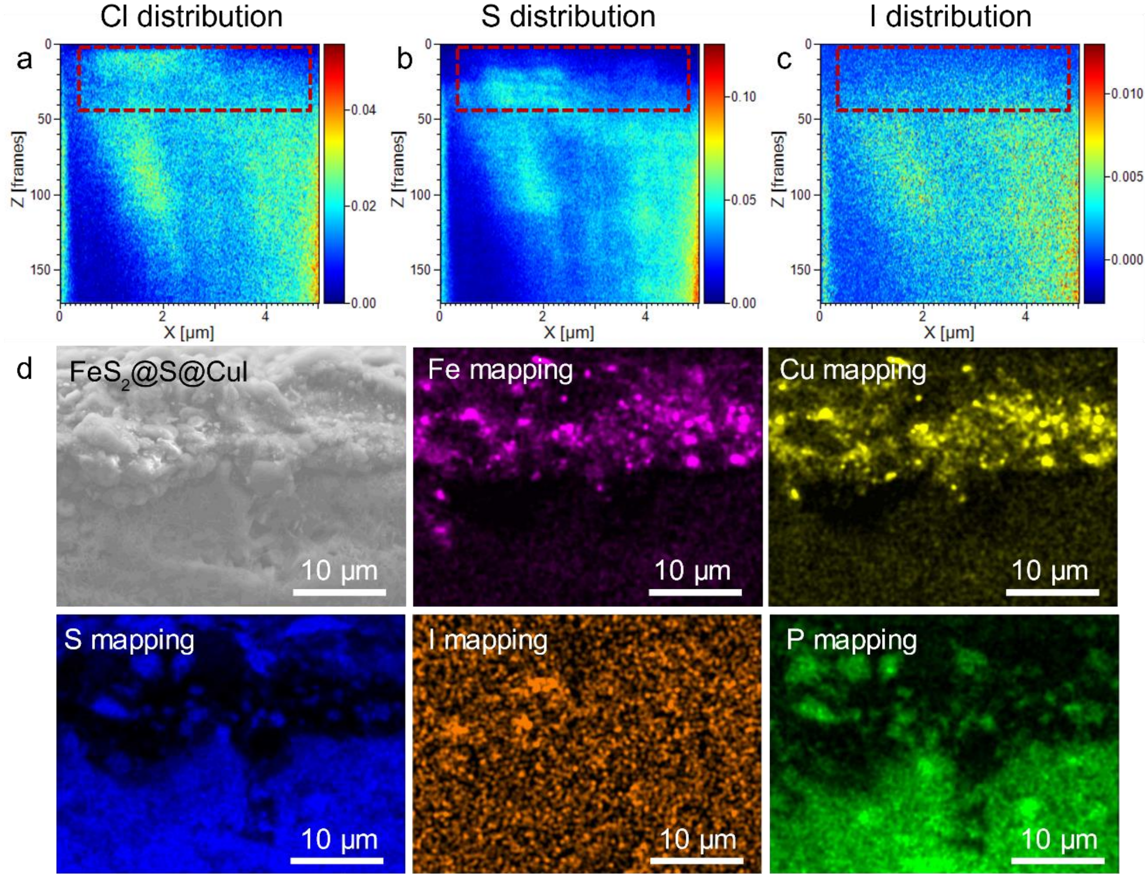

Figure 6-4 Element distribution for (a) Cl, (b) S and (c) I in FeS$_2$@S@CuI composite cathode after 20 cycles. (d) Cross-section SEM and EDS images of FeS$_2$@S@CuI composite cathode after 100 cycles.

ToF-SIMS and EDS were collected to explore the mechanism of the catalytic effect of CuI. For the elemental distribution images in **Figure 6-4** a-c, the area that Cl-rich and S-poor is the Li$_6$PS$_5$Cl electrolyte rich area (marked by the red rectangle), while the area that Cl-poor and S-rich represents the FeS$_2$@S rich area. As shown in **Figure 6-4** a-c, I signal also has high intensity in Li$_6$PS$_5$Cl electrolyte rich area (marked by the red rectangle), proving the I migration from the FeS$_2$@S rich area to Li$_6$PS$_5$Cl electrolyte rich area after discharge/charge processes. The I migration can decrease the interfacial resistance of the composite cathode, because LiI can increase the Li^+ transfer between Li_6PS_5Cl and Li_2S, which is in accordance with the EIS results in **Figure 6-3** c. Benefited from the catalytic effect of CuI, the FeS_2@S@CuI composite cathode retains excellent structure integrity (**Figure 6-4** d) without crack formation inside the composite cathode layer and at Li_6PS_5Cl/FeS_2@S@CuI interface.

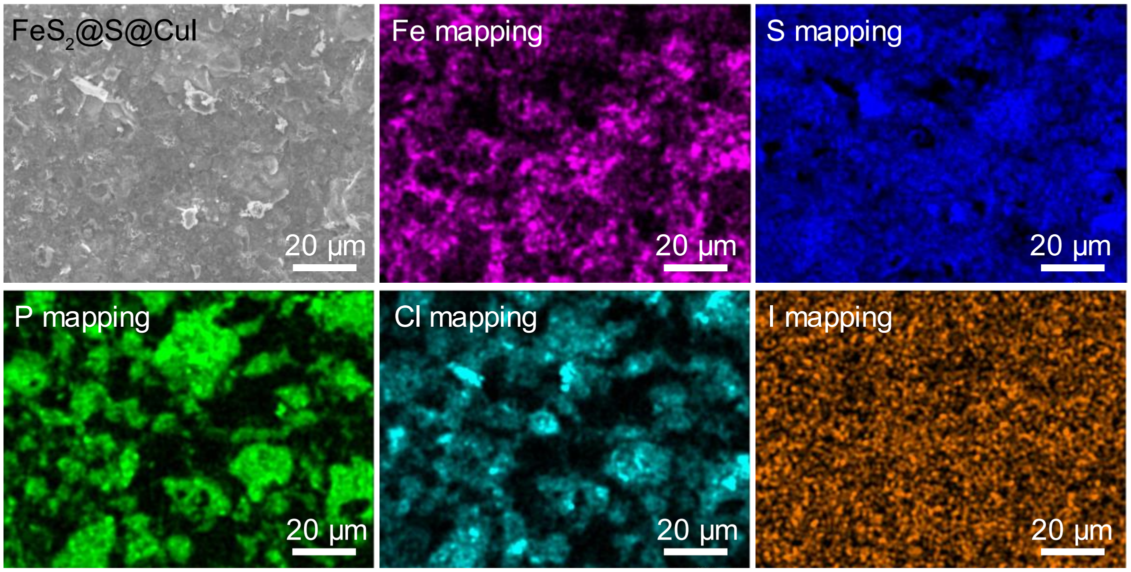

Figure 6-5 SEM and EDS images for the surface of FeS_2@S@CuI composite cathode after 100 cycles.

Besides, all the components in the composite cathode were homogeneously distributed after 100 cycles (**Figure 6-5**). While cracks are obviously observed in FeS_2@S composite cathode without CuI additive (**Figure 6-6**) after 100 cycles, which lead to significantly impedance increase (**Figure 6-7**) compared with that of FeS_2@S@CuI composite cathode.

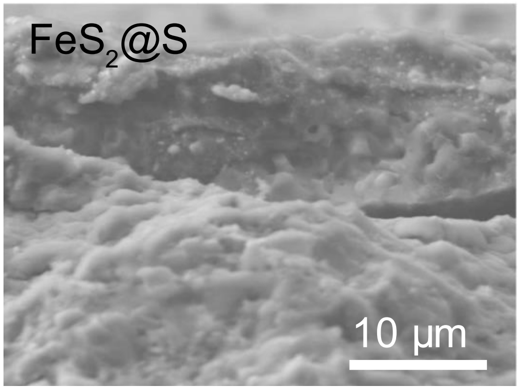

Figure 6-6 SEM images for the surface of FeS_2@S composite cathode after 100 cycles.

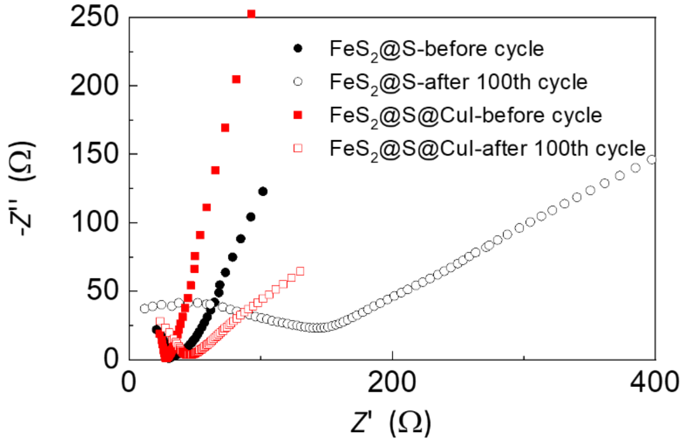

Figure 6-7 Impedance spectra of FeS_2@S@CuI andFeS_2@S composite cathode before and after 100 cycles.

6.6 Conclusion

In summary, we use FeS_2@S@CuI composite as a model material to demonstrate that the *in-situ* formed fast Li^+/*e^-* transfer in sulfur cathode is efficient to improve the S/Li_2S redox kinetics. After the initial few cycles, FeS_2@S@CuI *in-situ* transfers to FeS_2@S@Cu@LiI composite. Electronic/ionic conductive FeS_2 acts as sulfur host, Cu acts as electronic conductive additive, LiI acts as Li^+ transfer bridge at FeS_2-S-

Li_6PS_5Cl triple-phase boundaries due to the migration of I from the FeS_2@S to Li_6PS_5Cl. Such a composite sulfur cathode with enhanced S/Li_2S redox kinetics enables the battery with areal capacity of 4 mAh cm^{-2} to achieve a high initial Coulombic efficiency of 94.6% at current density of 0.5 mA cm^{-2} under room temperature. Besides, the constructed all-solid-state batteries show excellent cycling stability and high capacity utilization at both high areal capacity of 4 mAh cm^{-2} and low temperature of -30^oC. This work offers a new strategy for designing high-performance all-solid-state battery with sulfur cathode.

Chapter 7 Summary and Future Work

7.1 Lithium Anode | SSE Interfaces

On the anode side interface, addressed both the challenges of Li dendrite and high interface resistance by doping strontium(Sr) into lithium anodes. Different from all previous metal/metal oxide coating on garnet or Li alloy anodes that form lithiophilic interlayer, Li-Sr/SrO-doped-Li2O are enriched on the interface forming a lithiophilic/lithiophobic bifunctional layer. The interlayer reduces the interfacial resistance and also suppresses lithium dendrite. The stability of the lithiophobic SrO doped Li_2O against Li prevents reducing the garnet and suppresses Li dendrite, which distinguishes it from all reported alloy electron-conducting interlayers. The optimized Li-Sr | garnet | Li-Sr symmetric cell achieves a critical current density of 1.3 mA/cm^2 and can be cycled for 1,000 cycles under 0.5 mA/cm^2 at room temperature. The bifunctional lithiophilic/lithiophobic interlayer provides a new strategy for high-performance garnet solid-state lithium batteries

Enlightened by the effectiveness of the Sr work, I tried to further more stable material on the interface. I screened the Gibbs energy for the reaction between Li and the metal oxides ($nLi + MO_m \leftrightarrow M + nLiO_{m/n}$) and identified the $LiYO_2$ as a highly thermodynamical stable candidate for the interface between the electrolyte and lithium. In addition, $LiYO_2$ has a record high interface energy against lithium of 81.65 meV/Å, which would provide high dynamic stability against dendrite penetration. Guided by our design principle, we successfully established the Li | LLZTO interface with $LiYO_2$ as the interlayer, which endows the symmetric cells a high critical current density of 1.15 mA cm^{-2}, a critical capacity of 4.2 mAh cm^{-2} at 0.1 mA cm-2 and a long cycle life of 600 cycles under 0.5 mA cm^{-2}/0.25 mAh cm^{-2}. This work sheds new insight on the rational design of the interface for SSLBs with high performance.

Inspired by the failure analysis (Chapter 3.5) in the Sr work, I realized the impact the anode bulk properties on interface stability. Void formation was carefully analyzed, which should controlled by the product of the lithium full stripping capacity and the applied current, which is defined as the void suppression capability (VSC). The VSC can be enhanced by increasing the self-diffusivity and initial concentration of the lithium atoms. By refining the grain by introducing a Mg-1wt%La inoculant into molten lithium (LiMgLa), the lithium self-diffusivity and VSC are enhanced by 10.56 and 6.28 times, respectively, resulting in an increase in the critical current density/capacity from 1.2 mA·cm^{-2}/0.6 mAh·cm^{-2} for the Li anode to 2.2 mA·cm^{-2}/1.1 mAh·cm^{-2} for the LiMgLa anode. The LiMgLa anodes enable stable Li plating/stripping for over 1,200 h at 0.7 mA·cm^{-2} at room temperature. The phase-field model dynamically shows that the interfacial overpotential will be higher than the critical overpotential of the electrolyte when the Li stripping is larger than 70% of the full depletion capacity, leading to dendrite growth and cell failure. The new understanding of the interface evolution and strategy of refining Li grain size paves the way for the design of both high power and high energy density SSLBs.

7.2 Cathode | SSE Interfaces

Low initial Coulombic efficiency (CE) and capacity utilization at high cathode loading are the main challenges that impede the cyclic performance and the energy density of sulfur cathode due to the poor S/Li_2S redox kinetics. Herein, we address both challenges using FeS_2@S@CuI composite, where Li^+/e^- conductive FeS_2 acts as an active sulfur host to ameliorate the volume change of sulfur, catalytic CuI additive will *in-situ* transfer to Cu-LiI, and the *in-situ* formed LiI acts as a Li^+ transfer bridge at FeS_2-S-Li_6PS_5Cl phase boundaries to promote Li^+ transfer, thus increasing the S/Li_2S redox kinetics. Benefited from these merits, the FeS_2@S@CuI composite with areal capacity of 4.0 mAh cm^{-2} shows a high initial CE of 94.6% at current density of 0.5 mA cm^{-2} under room temperature. Besides, a long cyclic performance with capacity retention of 88.8% after 145 cycles was also at high areal capacity of 4.0 mAh cm^{-2} under room temperature. Furthermore, a high capacity utilization of 96.5% at room temperature, 44.4% at -20^{o}C and 33.3% at -30^{o}C is also achieved for the FeS_2@S@CuI composite cathode, which has never been reported in all-solid-state battery. This work provides a strategy for designing high-performance solid-state sulfur cathodes.

7.3 Future Work

For the past decades, the hotspot of all-solid-state batteries research has been switched from finding high ionic conductivity SSE to pursuing low interface resistance. In this dissertation, it has been demonstrated that new understanding such as interface energy, VSC are critical and should be paid more attention to. Future works could focus on:

1. Controllable construction of the high interface energy interface. The *in-situ* formed method by molten lithium is not suitable for other SSE systems such as sulfide and polymer, and it does not have a good manufacturability for mass production.

2. Mechanical properties enhancement of the bulk anode and bulk SSE towards void suppression. Methods to achieve a more deformable anode without sacrificing the energy density, and to have more deformable SSEs without adding organic binders would be highly beneficial to construct a robust interface, and thus to realize the practical future SSLM without high external pressure add-on.

3. The failure mechanism of the Li+/e- conductive network inside a solid-state battery cathode should be further explored for us the design a interface that could realize high cathode active material ratio.

Bibliography

(1) Schainker, R. B. Executive Overview: Energy Storage Options for a Sustainable Energy Future. *Ieee Power Eng Soc Gen Meet 2004* 2004, 1–6. https://doi.org/10.1109/pes.2004.1373298.

(2) Whittingham, S. M. Ultimate Limits to Intercalation Reactions for Lithium Batteries. *Chemical Reviews* 2014, *114* (23), 11414–11443. https://doi.org/10.1021/cr5003003.

(3) Thackeray, M. M.; Wolverton, C.; Isaacs, E. D. Electrical Energy Storage for Transportation—Approaching the Limits of, and Going beyond, Lithium-Ion Batteries. *Energ Environ Sci* 2012, *5* (7), 7854–7863. https://doi.org/10.1039/c2ee21892e.

(4) Kim, Y.; Waluyo, I.; Hunt, A.; Yildiz, B. Avoiding CO2 Improves Thermal Stability at the Interface of Li7La3Zr2O12 Electrolyte with Layered Oxide Cathodes. *Adv Energy Mater* 2022, *12* (13), 2102741. https://doi.org/10.1002/aenm.202102741.

(5) Wang, C.; Fu, K.; Kammampata, S.; McOwen, D. W.; Samson, A.; Zhang, L.; Hitz, G. T.; Nolan, A. M.; Wachsman, E. D.; Mo, Y.; Thangadurai, V.; Hu, L. Garnet-Type Solid-State Electrolytes: Materials, Interfaces, and Batteries. *Chem Rev* 2020, *120* (10), 4257–4300. https://doi.org/10.1021/acs.chemrev.9b00427.

(6) Yu, C.; Zhao, F.; Luo, J.; Zhang, L.; Sun, X. Recent Development of Lithium Argyrodite Solid-State Electrolytes for Solid-State Batteries: Synthesis, Structure, Stability and Dynamics. *Nano Energy* 2021, *83*, 105858. https://doi.org/10.1016/j.nanoen.2021.105858.

(7) Thangadurai, V.; Kaack, H.; Weppner, W. J. Novel Fast Lithium Ion Conduction in Garnet-Type Li5La3M2O12 (M = Nb, Ta). *J Am Ceram Soc* 2003, *86* (3), 437–440. https://doi.org/10.1111/j.1151-2916.2003.tb03318.x.

(8) Murugan, R.; Thangadurai, V.; Weppner, W. Fast Lithium Ion Conduction in Garnet-Type Li7La3Zr2O12. *Angewandte Chemie International Edition* 2007, *46* (41), 7778–7781. https://doi.org/10.1002/anie.200701144.

(9) Li, Y.; Han, J.-; Wang, C.-; Xie, H.; Goodenough, J. B. Optimizing Li + Conductivity in a Garnet Framework. *J Mater Chem* 2012, *22* (30), 15357–15361. https://doi.org/10.1039/c2jm31413d.

(10) Han, F.; Zhu, Y.; He, X.; Mo, Y.; Wang, C. Electrochemical Stability of Li10GeP2S12 and Li7La3Zr2O12 Solid Electrolytes. *Advanced Energy Materials* 2016, *6* (8), 1501590. https://doi.org/10.1002/aenm.201501590.

(11) Miara, L. J.; Richards, W.; Wang, Y. E.; Ceder, G. First-Principles Studies on Cation Dopants and Electrolyte|Cathode Interphases for Lithium Garnets. *Chem Mater 27* (11), 4040–4047. https://doi.org/10.1021/acs.chemmater.5b01023.

(12) Buschmann, H.; Dölle, J.; Berendts, S.; Kuhn, A.; Bottke, P.; Wilkening, M.; Heitjans, P.; Senyshyn, A.; Ehrenberg, H.; Lotnyk, A.; Duppel, V.; Kienle, L.; Janek, J. Structure and Dynamics of the Fast Lithium Ion Conductor "Li 7 La 3 Zr 2 O 12 ." *Phys Chem Chem Phys* 2011, *13* (43), 19378–19392. https://doi.org/10.1039/c1cp22108f.

(13) Wu, J.-F.; Pang, W. K.; Peterson, V. K.; Wei, L.; Guo, X. Garnet-Type Fast Li-Ion Conductors with High Ionic Conductivities for All-Solid-State Batteries. *Acs Appl Mater Inter* 2017, *9* (14), 12461–12468. https://doi.org/10.1021/acsami.7b00614.

(14) Bernges, T.; Culver, S. P.; Minafra, N.; Koerver, R.; Zeier, W. G. Competing Structural Influences in the Li Superionic Conducting Argyrodites Li6PS5–x Se x Br ($0 \leq x \leq 1$) upon Se Substitution. *Inorg Chem* 2018, *57* (21), 13920–13928. https://doi.org/10.1021/acs.inorgchem.8b02443.

(15) Yubuchi, S.; Teragawa, S.; Aso, K.; Tadanaga, K.; Hayashi, A.; Tatsumisago, M. Preparation of High Lithium-Ion Conducting Li6PS5Cl Solid Electrolyte from Ethanol Solution for All-Solid-State Lithium Batteries. *J Power Sources* 2015, *293*, 941–945. https://doi.org/10.1016/j.jpowsour.2015.05.093.

(16) Yubuchi, S.; Tsukasaki, H.; Sakuda, A.; Mori, S.; Hayashi, A.; Tatsumisago, M. Quantitative Analysis of Crystallinity in an Argyrodite Sulfide-Based Solid Electrolyte Synthesized via Solution Processing. *Rsc Adv* 2019, *9* (25), 14465–14471. https://doi.org/10.1039/c9ra00949c.

(17) Yubuchi, S.; Uematsu, M.; Hotehama, C.; Sakuda, A.; Hayashi, A.; Tatsumisago, M. An Argyrodite Sulfide-Based Superionic Conductor Synthesized by a Liquid-Phase Technique with Tetrahydrofuran and Ethanol. *J Mater Chem A* 2018, *7* (2), 558–566. https://doi.org/10.1039/c8ta09477b.

(18) Rao, R. P.; Sharma, N.; Peterson, V. K.; Adams, S. Formation and Conductivity Studies of Lithium Argyrodite Solid Electrolytes Using In-Situ Neutron Diffraction. *Solid State Ionics* 2013, *230*, 72–76. https://doi.org/10.1016/j.ssi.2012.09.014.

(19) Shen, Z.; Zhang, W.; Zhu, G.; Huang, Y.; Feng, Q.; Lu, Y. Design Principles of the Anode–Electrolyte Interface for All Solid-State Lithium Metal Batteries. *Small Methods* 2019, *4* (1), 1900592. https://doi.org/10.1002/smtd.201900592.

(20) Zhang, S. S. Liquid Electrolyte Lithium/Sulfur Battery: Fundamental Chemistry, Problems, and Solutions. *J Power Sources* 2013, *231*, 153–162. https://doi.org/10.1016/j.jpowsour.2012.12.102.

(21) Qu, Y.; Zhang, Z.; Jiang, S.; Wang, X.; Lai, Y.; Liu, Y.; Li, J. Confining Selenium in Nitrogen-Containing Hierarchical Porous Carbon for High-Rate Rechargeable Lithium–Selenium Batteries. *J Mater Chem A* 2014, *2* (31), 12255–12261. https://doi.org/10.1039/c4ta02563f.

(22) Ulissi, U.; Ito, S.; Hosseini, S. M.; Varzi, A.; Aihara, Y.; Passerini, S. High Capacity All-Solid-State Lithium Batteries Enabled by Pyrite-Sulfur Composites. *Adv Energy Mater* 2018, *8* (26), 1801462. https://doi.org/10.1002/aenm.201801462.

(23) Mwizerwa, J. P.; Zhang, Q.; Han, F.; Wan, H.; Cai, L.; Wang, C.; Yao, X. Sulfur-Embedded FeS2 as a High-Performance Cathode for Room Temperature All-Solid-State Lithium–Sulfur Batteries. *Acs Appl Mater Inter* 2020, *12* (16), 18519–18525. https://doi.org/10.1021/acsami.0c01607.

(24) Hohenberg, P.; Kohn, W. Inhomogeneous Electron Gas. *Phys Rev* 1964, *136* (3B), B864–B871. https://doi.org/10.1103/physrev.136.b864.

(25) Kohn, W.; Sham, L. Self-Consistent Equations Including Exchange and Correlation Effects. *Phys Rev* 1965, *140* (4A), A1133–A1138. https://doi.org/10.1103/physrev.140.a1133.

(26) Kresse, G.; Hafner, J. Ab Initio Molecular Dynamics for Liquid Metals. *Phys Rev B* 1993, *47* (1), 558–561. https://doi.org/10.1103/physrevb.47.558.

(27) Blöchl, P. Projector Augmented-Wave Method. *Phys Rev B* 1994, *50* (24), 17953–17979. https://doi.org/10.1103/physrevb.50.17953.

(28) Kresse, G. Efficient Iterative Schemes for Ab Initio Total-Energy Calculations Using a Plane-Wave Basis Set. *Phys Rev B* 1996, *54* (16), 11169–11186. https://doi.org/10.1103/physrevb.54.11169.

(29) Perdew, J. P.; Burke, K.; Ernzerhof, M. Generalized Gradient Approximation Made Simple. *Phys Rev Lett* 1996, *77* (18), 3865–3868. https://doi.org/10.1103/physrevlett.77.3865.

(30) Grimme, S.; Antony, J.; Ehrlich, S.; Krieg, H. A Consistent and Accurate Ab Initio Parametrization of Density Functional Dispersion Correction (DFT-D) for the 94 Elements H-Pu. *J Chem Phys* 2010, *132* (15), 154104. https://doi.org/10.1063/1.3382344.

(31) Monkhorst, H. J.; Pack, J. D. Special Points for Brillouin-Zone Integrations. *Phys Rev B* 1976, *13* (12), 5188–5192. https://doi.org/10.1103/physrevb.13.5188.

(32) Fan, X.; Ji, X.; Han, F.; Yue, J.; Chen, J.; Chen, L.; Deng, T.; Jiang, J.; Wang, C. Fluorinated Solid Electrolyte Interphase Enables Highly Reversible Solid-State Li Metal Battery. *Sci Adv* 2018, *4* (12), eaau9245. https://doi.org/10.1126/sciadv.aau9245.

(33) Momma, K.; Izumi, F. VESTA 3 for Three-Dimensional Visualization of Crystal, Volumetric and Morphology Data. *J Appl Crystallogr* 2011, *44* (6), 1272–1276. https://doi.org/10.1107/s0021889811038970.

(34) Diouf, B.; Pode, R. Potential of Lithium-Ion Batteries in Renewable Energy. *Renew Energ* 2015, *76*, 375–380. https://doi.org/10.1016/j.renene.2014.11.058.

(35) Feng, X.; Ouyang, M.; Liu, X.; Lu, L.; Xia, Y.; He, X. Thermal Runaway Mechanism of Lithium Ion Battery for Electric Vehicles: A Review. *Energy Storage Mater* 2018, *10*, 246–267. https://doi.org/10.1016/j.ensm.2017.05.013.

(36) Aurbach, D.; Zinigrad, E.; Cohen, Y.; Teller, H. A Short Review of Failure Mechanisms of Lithium Metal and Lithiated Graphite Anodes in Liquid Electrolyte Solutions. *Solid State Ionics* 2002, *148* (3–4), 405–416. https://doi.org/10.1016/s0167-2738(02)00080-2.

(37) Tsai, C.-L.; Roddatis, V.; Chandran, V. C.; Ma, Q.; Uhlenbruck, S.; Bram, M.; Heitjans, P.; Guillon, O. Li7La3Zr2O12 Interface Modification for Li Dendrite Prevention. *Acs Appl Mater Inter* 2016, *8* (16), 10617–10626. https://doi.org/10.1021/acsami.6b00831.

(38) Fu, K.; Gong, Y.; Fu, Z.; Xie, H.; Yao, Y.; Liu, B.; Carter, M.; Wachsman, E.; Hu, L. Transient Behavior of the Metal Interface in Lithium Metal–Garnet Batteries. *Angewandte Chemie Int Ed* 2017, *56* (47), 14942–14947. https://doi.org/10.1002/anie.201708637.

(39) Krauskopf, T.; Mogwitz, B.; Rosenbach, C.; Zeier, W. G.; Janek, J. Diffusion Limitation of Lithium Metal and Li–Mg Alloy Anodes on LLZO Type Solid Electrolytes as a Function of Temperature and Pressure. *Adv Energy Mater* 2019, *9* (44), 1902568. https://doi.org/10.1002/aenm.201902568.

(40) Feng, W.; Dong, X.; Li, P.; Wang, Y.; Xia, Y. Interfacial Modification of Li/Garnet Electrolyte by a Lithiophilic and Breathing Interlayer. *J Power Sources* 2019, *419*, 91–98. https://doi.org/10.1016/j.jpowsour.2019.02.066.

(41) Luo, W.; Gong, Y.; Zhu, Y.; Li, Y.; Yao, Y.; Zhang, Y.; Fu, K.; Pastel, G.; Lin, C.; Mo, Y.; Wachsman, E. D.; Hu, L. Reducing Interfacial Resistance between

Garnet-Structured Solid-State Electrolyte and Li-Metal Anode by a Germanium Layer. *Adv Mater* 2017, *29* (22), 1606042. https://doi.org/10.1002/adma.201606042.

(42) Fu, K.; Gong, Y.; Liu, B.; Zhu, Y.; Xu, S.; Yao, Y.; Luo, W.; Wang, C.; Lacey, S. D.; Dai, J.; Chen, Y.; Mo, Y.; Wachsman, E.; Hu, L. Toward Garnet Electrolyte–Based Li Metal Batteries: An Ultrathin, Highly Effective, Artificial Solid-State Electrolyte/Metallic Li Interface. *Science Advances* 2017, *3* (4), e1601659. https://doi.org/10.1126/sciadv.1601659.

(43) Luo, W.; Gong, Y.; Zhu, Y.; Fu, K.; Dai, J.; Lacey, S. D.; Wang, C.; Liu, B.; Han, X.; Mo, Y.; Wachsman, E. D.; Hu, L. Transition from Superlithiophobicity to Superlithiophilicity of Garnet Solid-State Electrolyte. *J Am Chem Soc* 2016, *138* (37), 12258–12262. https://doi.org/10.1021/jacs.6b06777.

(44) Han, X.; Gong, Y.; Fu, K.; He, X.; Hitz, G. T.; Dai, J.; Pearse, A.; Liu, B.; Wang, H.; Rubloff, G.; Mo, Y.; Thangadurai, V.; Wachsman, E. D.; Hu, L. Negating Interfacial Impedance in Garnet-Based Solid-State Li Metal Batteries. *Nat Mater* 2016, *16* (5), 572–579. https://doi.org/10.1038/nmat4821.

(45) Wang, C.; Gong, Y.; Liu, B.; Fu, K.; Yao, Y.; Hitz, E.; Li, Y.; Dai, J.; Xu, S.; Luo, W.; Wachsman, E. D.; Hu, L. Conformal, Nanoscale ZnO Surface Modification of Garnet-Based Solid-State Electrolyte for Lithium Metal Anodes. *Nano Lett* 2016, *17* (1), 565–571. https://doi.org/10.1021/acs.nanolett.6b04695.

(46) Cai, M.; Lu, Y.; Yao, L.; Jin, J.; Wen, Z. Robust Conversion-Type Li/Garnet Interphases from Metal Salt Solutions. *Chem Eng J* 2021, 129158. https://doi.org/10.1016/j.cej.2021.129158.

(47) Deng, T.; Ji, X.; Zhao, Y.; Cao, L.; Li, S.; Hwang, S.; Luo, C.; Wang, P.; Jia, H.; Fan, X.; Lu, X.; Su, D.; Sun, X.; Wang, C.; Zhang, J.-G. Tuning the Anode-Electrolyte Interface Chemistry for Garnet-Based Solid-State Li Metal Batteries. *Adv Mater Deerfield Beach Fla* 2020, *32* (23), e2000030. https://doi.org/10.1002/adma.202000030.

(48) Zhang, S. S.; Xu, K.; Jow, T. R. The Low Temperature Performance of Li-Ion Batteries. *J Power Sources* 2003, *115* (1), 137–140. https://doi.org/10.1016/s0378-7753(02)00618-3.

(49) Krauskopf, T.; Hartmann, H.; Zeier, W. G.; Janek, J. Toward a Fundamental Understanding of the Lithium Metal Anode in Solid-State Batteries—An Electrochemo-Mechanical Study on the Garnet-Type Solid Electrolyte Li 6.25 Al 0.25 La 3 Zr 2 O 12. *Acs Appl Mater Inter* 2019, *11* (15), 14463–14477. https://doi.org/10.1021/acsami.9b02537.

(50) Kasemchainan, J.; Zekoll, S.; Jolly, D.; Ning, Z.; Hartley, G. O.; Marrow, J.; Bruce, P. G. Critical Stripping Current Leads to Dendrite Formation on Plating in Lithium Anode Solid Electrolyte Cells. *Nature materials* 2019. https://doi.org/10.1038/s41563-019-0438-9.

(51) Kinzer, B.; Davis, A. L.; Krauskopf, T.; Hartmann, H.; LePage, W. S.; Kazyak, E.; Janek, J.; Dasgupta, N. P.; Sakamoto, J. Operando Analysis of the Molten Li|LLZO Interface: Understanding How the Physical Properties of Li Affect the Critical Current Density. *Matter* 2021. https://doi.org/10.1016/j.matt.2021.04.016.

(52) Huang, W.; Zhao, N.; Bi, Z.; Shi, C.; Guo, X.; Fan, L.; Nan, C. Can We Find Solution to Eliminate Li Penetration through Solid Garnet Electrolytes? *Mater Today Nano* 2020, *10*, 100075. https://doi.org/10.1016/j.mtnano.2020.100075.

(53) Wang, C.; Xie, H.; Zhang, L.; Gong, Y.; Pastel, G.; Dai, J.; Liu, B.; Wachsman, E. D.; Hu, L. Universal Soldering of Lithium and Sodium Alloys on Various Substrates for Batteries. *Adv Energy Mater* 2018, *8* (6), 1701963. https://doi.org/10.1002/aenm.201701963.

(54) Koshikawa, H.; Matsuda, S.; Kamiya, K.; Miyayama, M.; Kubo, Y.; Uosaki, K.; Hashimoto, K.; Nakanishi, S. Electrochemical Impedance Analysis of the Li/Au-Li7La3Zr2O12 Interface during Li Dissolution/Deposition Cycles: Effect of Pre-Coating Li7La3Zr2O12 with Au. *J Electroanal Chem* 2019, *835*, 143–149. https://doi.org/10.1016/j.jelechem.2019.01.025.

(55) Chen, J.; Li, Q.; Pollard, T. P.; Fan, X.; Borodin, O.; Wang, C. Electrolyte Design for Li Metal-Free Li Batteries. *Mater Today* 2020, *39*, 118–126. https://doi.org/10.1016/j.mattod.2020.04.004.

(56) Lorger, S.; Usiskin, R.; Maier, J. Transport and Charge Carrier Chemistry in Lithium Oxide. *J Electrochem Soc* 2019, *166* (10), A2215–A2220. https://doi.org/10.1149/2.1121910jes.

(57) Thangadurai, V.; Weppner, W. Li6ALa2Ta2O12 (A = Sr, Ba): Novel Garnet-Like Oxides for Fast Lithium Ion Conduction. *Adv Funct Mater* 2005, *15* (1), 107–112. https://doi.org/10.1002/adfm.200400044.

(58) Thangadurai, V.; Ceramic, W. W. of the. Li6ALa2Nb2O12 (A=Ca, Sr, Ba): A New Class of Fast Lithium Ion Conductors with Garnet-Like Structure. 2005.

(59) Cheng, K.; Xu, H.; Zhang, L.; Du, Y.; Zhou, J.; Tang, S.; Chen, M. Numerical Simulation of the SrZrO3 Formation in Solid Oxide Fuel Cells. *J Electron Mater* 2019, *48* (9), 5510–5515. https://doi.org/10.1007/s11664-019-07236-0.

(60) Risold, D.; Hallstedt, B.; Gauckler, L. J. The Strontium-Oxygen System. *Calphad* 1996, *20* (3), 353–361. https://doi.org/10.1016/s0364-5916(96)00037-5.

(61) Doveren, V. H.; Verhoeven, J. A. T. H. XPS Spectra of Ca, Sr, Ba and Their Oxides. *J Electron Spectrosc* 1980, *21* (3), 265–273. https://doi.org/10.1016/0368-2048(80)85055-9.

(62) Li, H.; Balaya, P.; Maier, J. Li-Storage via Heterogeneous Reaction in Selected Binary Metal Fluorides and Oxides. *J Electrochem Soc* 2004, *151* (11), A1878. https://doi.org/10.1149/1.1801451.

(63) Roine, A. HSC - SOFTWARE VER. 3.0 FOR THERMODYNAMIC CALCULATIONS. *Proceedings of the International Symposium on Computer Software in Chemical and Extractive Metallurgy* 1989, 15–29. https://doi.org/10.1016/b978-0-08-036087-4.50007-0.

(64) Huang, X.; Lu, Y.; Guo, H.; Song, Z.; Xiu, T.; Badding, M. E.; Wen, Z. None-Mother-Powder Method to Prepare Dense Li-Garnet Solid Electrolytes with High Critical Current Density. *ACS Applied Energy Materials* 2018. https://doi.org/10.1021/acsaem.8b00976.

(65) Park, R.; Eschler, C. M.; Fincher, C. D.; Badel, A. F.; Guan, P.; Pharr, M.; Sheldon, B. W.; Carter, C. W.; Viswanathan, V.; Chiang, Y.-M. Semi-Solid Alkali Metal Electrodes Enabling High Critical Current Densities in Solid Electrolyte Batteries. *Nat Energy* 2021, *6* (3), 314–322. https://doi.org/10.1038/s41560-021-00786-w.

(66) Xie, X.; Xing, J.; Hu, D.; Gu, H.; Chen, C.; Guo, X. Lithium Expulsion from the Solid-State Electrolyte Li 6.4 La 3 Zr 1.4 Ta 0.6 O 12 by Controlled Electron Injection in a SEM. *ACS Applied Materials & Interfaces* 2018, *10* (6), 5978–5983. https://doi.org/10.1021/acsami.7b17276.

(67) Lepley, N. D.; Holzwarth, N. A. W. Modeling Interfaces between Solids: Application to Li Battery Materials. *Phys Rev B* 2015, *92* (21), 214201. https://doi.org/10.1103/physrevb.92.214201.

(68) Xu, R.; Han, F.; Ji, X.; Fan, X.; Tu, J.; Wang, C. Interface Engineering of Sulfide Electrolytes for All-Solid-State Lithium Batteries. *Nano Energy* 2018. https://doi.org/10.1016/j.nanoen.2018.09.061.

(69) Zhang, X.; Cheng, X.; Chen, X.; Yan, C.; Zhang, Q. Fluoroethylene Carbonate Additives to Render Uniform Li Deposits in Lithium Metal Batteries. *Adv. Funct. Mater.* 2017, *27* (10), 1605989. https://doi.org/10.1002/adfm.201605989.

(70) Zhu, Z.; Tang, Y.; Lv, Z.; Wei, J.; Chemie …, Z. Y. Fluoroethylene Carbonate Enabling a Robust LiF-rich Solid Electrolyte Interphase to Enhance the Stability of the MoS2 Anode for Lithium-Ion Storage. 2018.

(71) Janek, J.; Zeier, W. G. A Solid Future for Battery Development. *Nat Energy* 2016, *1* (9), 16141. https://doi.org/10.1038/nenergy.2016.141.

(72) Manthiram, A.; Yu, X.; Wang, S. Lithium Battery Chemistries Enabled by Solid-State Electrolytes. *Nat Rev Mater* 2017, *2* (4), 16103. https://doi.org/10.1038/natrevmats.2016.103.

(73) Pfenninger, R.; Struzik, M.; Garbayo, I.; Stilp, E.; Rupp, J. L. M. A Low Ride on Processing Temperature for Fast Lithium Conduction in Garnet Solid-State Battery Films. *Nat Energy* 2019, *4* (6), 475–483. https://doi.org/10.1038/s41560-019-0384-4.

(74) Pasta, M.; Armstrong, D.; Brown, Z. L.; Bu, J.; Castell, M. R.; Chen, P.; Cocks, A.; Corr, S. A.; Cussen, E. J.; Darnbrough, E.; Deshpande, V.; Doerrer, C.; Dyer, M. S.; El-Shinawi, H.; Fleck, N.; Grant, P.; Gregory, G. L.; Grovenor, C.; Hardwick, L. J.; Irvine, J. T. S.; Lee, H. J.; Li, G.; Liberti, E.; McClelland, I.; Monroe, C.; Nellist, P. D.; Shearing, P. R.; Shoko, E.; Song, W.; Jolly, D. S.; Thomas, C. I.; Turrell, S. J.; Vestli, M.; Williams, C. K.; Zhou, Y.; Bruce, P. G. 2020 Roadmap on Solid-State Batteries. *J Phys Energy* 2020, *2* (3), 032008. https://doi.org/10.1088/2515-7655/ab95f4.

(75) Krauskopf, T.; Richter, F. H.; Zeier, W. G.; Janek, J. Physicochemical Concepts of the Lithium Metal Anode in Solid-State Batteries. *Chem Rev* 2020, *120* (15), 7745–7794. https://doi.org/10.1021/acs.chemrev.0c00431.

(76) Famprikis, T.; Canepa, P.; Dawson, J. A.; Islam, S. M.; Masquelier, C. Fundamentals of Inorganic Solid-State Electrolytes for Batteries. *Nature Materials* 2019, 1–14. https://doi.org/10.1038/s41563-019-0431-3.

(77) Han, F.; Westover, A. S.; Yue, J.; Fan, X.; Wang, F.; Chi, M.; Leonard, D. N.; Dudney, N. J.; Wang, H.; Wang, C. High Electronic Conductivity as the Origin of Lithium Dendrite Formation within Solid Electrolytes. *Nature Energy* 2019, 1–10. https://doi.org/10.1038/s41560-018-0312-z.

(78) Liu, X.; Garcia-Mendez, R.; Lupini, A. R.; Cheng, Y.; Hood, Z. D.; Han, F.; Sharafi, A.; Idrobo, J. C.; Dudney, N. J.; Wang, C.; Ma, C.; Sakamoto, J.; Chi, M. Local Electronic Structure Variation Resulting in Li 'Filament' Formation within Solid Electrolytes. *Nat Mater* 2021, *20* (11), 1485–1490. https://doi.org/10.1038/s41563-021-01019-x.

(79) Huo, H.; Luo, J.; Thangadurai, V.; Guo, X.; Nan, C.-W.; Sun, X. Li 2 CO 3 : A Critical Issue for Developing Solid Garnet Batteries. *Acs Energy Lett* 2019, *5* (1), 252–262. https://doi.org/10.1021/acsenergylett.9b02401.

(80) Wang, T.; Duan, J.; Zhang, B.; Luo, W.; Ji, X.; Xu, H.; Huang, Y.; Huang, L.; Song, Z.; Wen, J.; Wang, C.; Huang, Y.; Goodenough, J. B. A Self-Regulated Gradient Interphase for Dendrite-Free Solid-State Li Batteries. *Energ Environ Sci* 2022. https://doi.org/10.1039/d1ee03604a.

(81) Chen, Y.; Wang, Z.; Li, X.; Yao, X.; Wang, C.; Li, Y.; Xue, W.; Yu, D.; Kim, S.; Yang, F.; Kushima, A.; Zhang, G.; Huang, H.; Wu, N.; Mai, Y.-W.; Goodenough, J. B.; Li, J.; Chen, Y.; Wang, Z.; Li, X.; Yao, X.; Wang, C.; Li, Y.; Xue, W.; Yu, D.; Kim, S.; Yang, F.; Kushima, A.; Zhang, G.; Huang, H.; Wu, N.; Mai, Y.-W.; Goodenough, J. B.; Li, J. Li Metal Deposition and Stripping in a Solid-State Battery via Coble Creep. *Nature* 2020. https://doi.org/10.1038/s41586-020-1972-y.

(82) Raj, V.; Venturi, V.; Kankanallu, V. R.; Kuiri, B.; Viswanathan, V.; Aetukuri, N. P. B. Direct Correlation between Void Formation and Lithium Dendrite Growth in Solid-State Electrolytes with Interlayers. *Nat Mater* 2022, 1–7. https://doi.org/10.1038/s41563-022-01264-8.

(83) Tikekar, M. D.; Choudhury, S.; Tu, Z.; Archer, L. A. Design Principles for Electrolytes and Interfaces for Stable Lithium-Metal Batteries. *Nature Energy* 2016, *1* (9), 16114. https://doi.org/10.1038/nenergy.2016.114.

(84) Ji, X.; Hou, S.; Wang, P.; He, X.; Piao, N.; Chen, J.; Fan, X.; Wang, C. Solid-State Electrolyte Design for Lithium Dendrite Suppression. *Adv Mater* 2020, *32* (46), 2002741. https://doi.org/10.1002/adma.202002741.

(85) Jana, A.; Woo, S. I.; Vikrant, K. S. N.; García, R. E. Electrochemomechanics of Lithium Dendrite Growth. *Energ Environ Sci* 2019, *12* (12), 3595–3607. https://doi.org/10.1039/c9ee01864f.

(86) Parekh, M. N.; Rahn, C. D.; Archer, L. A. Controlling Dendrite Growth in Lithium Metal Batteries through Forced Advection. *J Power Sources* 2020, *452*, 227760. https://doi.org/10.1016/j.jpowsour.2020.227760.

(87) Doux, J.; Nguyen, H.; Tan, D. H. S.; Banerjee, A.; Wang, X.; Wu, E. A.; Jo, C.; Yang, H.; Meng, Y. S. Stack Pressure Considerations for Room-Temperature All-Solid-State Lithium Metal Batteries. *Adv Energy Mater* 2020, *10* (1), 1903253. https://doi.org/10.1002/aenm.201903253.

(88) Wang, M. J.; Choudhury, R.; Sakamoto, J. Characterizing the Li-Solid-Electrolyte Interface Dynamics as a Function of Stack Pressure and Current Density. *Joule* 2019. https://doi.org/10.1016/j.joule.2019.06.017.

(89) Sakamoto, J. More Pressure Needed. *Nat Energy* 2019, *4* (10), 827–828. https://doi.org/10.1038/s41560-019-0478-z.

(90) Lewis, J. A.; Cortes, F.; Liu, Y.; Miers, J. C.; Verma, A.; Vishnugopi, B. S.; Tippens, J.; Prakash, D.; Marchese, T. S.; Han, S.; Lee, C.; Shetty, P. P.; Lee, H.-W.; Shevchenko, P.; Carlo, F.; Saldana, C.; Mukherjee, P. P.; McDowell, M. T. Linking Void and Interphase Evolution to Electrochemistry in Solid-State Batteries Using Operando X-Ray Tomography. *Nat Mater* 2021, *20* (4), 503–510. https://doi.org/10.1038/s41563-020-00903-2.

(91) Liu, J.; Yuan, H.; Liu, H.; Zhao, C.; Lu, Y.; Cheng, X.; Huang, J.; Zhang, Q. Unlocking the Failure Mechanism of Solid State Lithium Metal Batteries. *Adv Energy Mater* 2021, 2100748. https://doi.org/10.1002/aenm.202100748.

(92) Thompson, A. P.; Aktulga, H. M.; Berger, R.; Bolintineanu, D. S.; Brown, W. M.; Crozier, P. S.; Veld, P. J. in ’t; Kohlmeyer, A.; Moore, S. G.; Nguyen, T. D.; Shan, R.; Stevens, M. J.; Tranchida, J.; Trott, C.; Plimpton, S. J. LAMMPS - a Flexible Simulation Tool for Particle-Based Materials Modeling at the Atomic, Meso, and Continuum Scales. *Comput Phys Commun* 2022, *271*, 108171. https://doi.org/10.1016/j.cpc.2021.108171.

(93) Hong, Z.; Viswanathan, V. Phase-Field Simulations of Lithium Dendrite Growth with Open-Source Software. *Acs Energy Lett* 2018, *3* (7), 1737–1743. https://doi.org/10.1021/acsenergylett.8b01009.

(94) Chen, L.; Zhang, H. W.; Liang, L. Y.; Liu, Z.; Qi, Y.; Lu, P.; Chen, J.; Chen, L.-Q. Modulation of Dendritic Patterns during Electrodeposition: A Nonlinear Phase-Field Model. *J Power Sources* 2015, *300*, 376–385. https://doi.org/10.1016/j.jpowsour.2015.09.055.

(95) Rosso, M.; Chazalviel, J.-N.; Chassaing, E. Calculation of the Space Charge in Electrodeposition from a Binary Electrolyte. *J Electroanal Chem* 2006, *587* (2), 323–328. https://doi.org/10.1016/j.jelechem.2005.11.030.

(96) Shen, Z.; Jin, X.; Tian, J.; Li, M.; Yuan, Y.; Zhang, S.; Fang, S.; Fan, X.; Xu, W.; Lu, H.; Lu, J.; Zhang, H. Cation-Doped ZnS Catalysts for Polysulfide Conversion in Lithium–Sulfur Batteries. *Nat Catal* 2022, 1–9. https://doi.org/10.1038/s41929-022-00804-4.

(97) Xu, S.; Kwok, C. Y.; Zhou, L.; Zhang, Z.; Kochetkov, I.; Nazar, L. F. A High Capacity All Solid-State Li-Sulfur Battery Enabled by Conversion-Intercalation Hybrid Cathode Architecture. *Adv. Funct. Mater.* 2021, *31* (2), 2004239. https://doi.org/10.1002/adfm.202004239.

(98) Wan, H.; Liu, G.; Li, Y.; Weng, W.; Mwizerwa, J. P.; Tian, Z.; Chen, L.; Yao, X. Transitional Metal Catalytic Pyrite Cathode Enables Ultrastable Four-Electron-Based All-Solid-State Lithium Batteries. *Acs Nano* 2019, *13* (8), 9551–9560. https://doi.org/10.1021/acsnano.9b04538.

(99) Wan, H.; Zhang, B.; Liu, S.; Zhang, J.; Yao, X.; Wang, C. Understanding LiI-LiBr Catalyst Activity for Solid State Li2S/S Reactions in an All-Solid-State Lithium Battery. *Nano Lett* 2021, *21* (19), 8488–8494. https://doi.org/10.1021/acs.nanolett.1c03415.

(100) Liu, M.; Wang, C.; Zhao, C.; Maas, E. van der; Lin, K.; Arszelewska, V. A.; Li, B.; Ganapathy, S.; Wagemaker, M. Quantification of the Li-Ion Diffusion over an Interface Coating in All-Solid-State Batteries via NMR Measurements. *Nat Commun* 2021, *12* (1), 5943. https://doi.org/10.1038/s41467-021-26190-2.

Publication and Presentation

Publications:

(1) **<u>He, X</u>**.; Ji, X.; Zhang, B.; Rodrigo, N. D.; Hou, S.; Gaskell, K.; Deng, T.; Wan, H.; Liu, S.; Xu, J.; Nan, B.; Lucht, B. L.; Wang, C. Tuning Interface Lithiophobicity for Lithium Metal Solid-State Batteries. *ACS Energy Letter* **2021**. https://doi.org/10.1021/acsenergylett.1c02122.

(2) **<u>He, X</u>**.; Ji, X.; Wang, Z.; Wan, H.; Wang, C. High Interface Energy Enabled Highly Stable Garnet-based Lithium Metal Solid-State Batteries (Ready to Submit)

(3) Ji, X.†; **<u>He, X.†</u>**; Chen, C.†; Hou, S.; Xu, J.; Zhang, B.; Ruan, Y.; Zhang, J.; Deng, T.; Chen, J.; Wang, C. Void Suppressive Lithium Anodes for All-Solid-State Batteries. *Nature Material* (Under Review) (Co-First Author)

(4) Wan, H. †; **<u>He, X.†</u>**; Ren, Y.; Wang, C. Highly reversible sulfur cathode for all-solid-state lithium-sulfur battery (Ready to Submit) (Co-First Author)

(5) Chiekezi, O.†; **<u>He, X.†</u>**; Wang, H.; Reed, D.; Wang, C.; Lu, X. Highly Conductive PEO-Based Composite Polymer Electrolyte for Na Battery Applications. *Journal of The Electrochemical Society* (Submitted) (Co-First Author)

(6) Deng, T.†; Cao, L.†; **<u>He, X.†</u>**; Li, A.-M.; Li, D.; Xu, J.; Liu, S.; Bai, P.; Jin, T.; Ma, L.; Schroeder, M. A.; Fan, X.; Wang, C. In Situ Formation of Polymer-Inorganic Solid-Electrolyte Interphase for Stable Polymeric Solid-State Lithium-Metal Batteries. *Chem* **2021**. (Co-First Author) https://doi.org/10.1016/j.chempr.2021.06.019.

(7) Bai, P.; Ji, X.; Zhang, J; Zhang, W.; Hou, S.; Su, H.; Li, M.; Deng, T.; Cao, L.; Liu, S.; **<u>He, X.</u>**; Xu, Y.; Wang, C. Formation of LiF-rich Cathode-Electrolyte Interphase by Electrolyte Reduction. *Angewandte Chemie Int Ed* **2022**. https://doi.org/10.1002/anie.202202731.

(8) Nan, B.; Chen, L.; Rodrigo, N. D.; Borodin, O.; Piao, N.; Xia, J.; Pollard, T.; Hou, S.; Zhang, J.; Ji, X.; Xu, J.; Zhang, X.; Ma, L.; **<u>He, X.</u>**; Liu, S.; Wan, H.; Hu, E.; Zhang, W.; Xu, K.; Yang, X.-Q.; Lucht, B.; Wang, C. Enhancing Li+ Transport in NMC811||Graphite Lithium-Ion Batteries at Low Temperatures by Using Low-Polarity-Solvent Electrolytes. *Angewandte Chemie Int Ed* **2022**. https://doi.org/10.1002/anie.202205967.

(9) Wan, H.; Zhang, J.; Xia, J.; Ji, X.; **<u>He, X.</u>**; Liu, S.; Wang, C. F and N Rich Solid Electrolyte for Stable All-Solid-State Battery. *Adv Funct Mater* **2021**, 2110876. https://doi.org/10.1002/adfm.202110876.

(10) Cao, X.; Zou, L.; Matthews, B. E.; Zhang, L.; **<u>He, X.</u>**; Ren, X.; Engelhard, M. H.; Burton, S. D.; El-Khoury, P. Z.; Lim, H.-S.; Niu, C.; Lee, H.; Wang, C.; Arey, B. W.; Wang, C.; Xiao, J.; Liu, J.; Xu, W.; Zhang, J.-G. Optimization of

Fluorinated Orthoformate Based Electrolytes for Practical High-Voltage Lithium Metal Batteries. *Energy Storage Mater* **2021**, 34, 76–84. https://doi.org/10.1016/j.ensm.2020.08.035.

(11) Wan, H.; Liu, S.; Deng, T.; Xu, J.; Zhang, J.; **He, X**.; Ji, X.; Yao, X.; Wang, C. Bifunctional Interphase-Enabled Li10GeP2S12 Electrolytes for Lithium–Sulfur Battery. *Acs Energy Lett* **2021**, *6* (3), 862–868. https://doi.org/10.1021/acsenergylett.0c02617.

(12) Ji, X.; Hou, S.; Wang, P.; **He, X.**; Piao, N.; Chen, J.; Fan, X.; Wang, C. Solid‐State Electrolyte Design for Lithium Dendrite Suppression. *Adv Mater* **2020**, *32* (46), 2002741. https://doi.org/10.1002/adma.202002741.

(13) Luo, C.†; Ji, X.†; Chen, J.; Gaskell, K. J.; **He, X.**; Liang, Y.; Jiang, J.; Wang, C. Solid‐State Electrolyte Anchored with a Carboxylated Azo Compound for All‐Solid‐State Lithium Batteries. *Angewandte Chemie Int Ed* **2018**, 57 (28), 8567–8571. https://doi.org/10.1002/anie.201804068.

Presentations:

(1) **He, X.**; Wang, C. Interface Design for All-Solid-State Lithium Metal Batteries. *ACS Fall **2022** - American Chemical Society, Chicago, IL.* Student Presentation Award Competition. Oral, August 27 (Third Prize Winner)

(2) **He, X.**; Ji, X.; Wang, C. Interface Lithiophobicity Regulation for Lithium Metal Solid-State Batteries. *ACS Fall **2022** - American Chemical Society, Chicago, IL.* [ENFL] Division of Energy and Fuels. Oral - In-person, August 23. 3720265.

(3) **He, X.**; Ji, X.; Wang, C. Interface Lithiophobicity Regulation for Lithium Metal Solid-State Batteries. *Electrochem Soc Meet Abstr* **2022**, MA2022-01 (1), 87–87. https://doi.org/10.1149/ma2022-01187mtgabs.

(4) Lu, X.; **He, X.**; Wang, H.; Reed, D.; Sprenkle, V. Highly Conductive PEO-Based Polymer Electrolyte for Na Battery Applications. *Electrochem Soc Meet Abstr* **2019**. https://doi.org/10.1149/ma2019-01/2/134.